Modeling of Microstructures and Stiffness of Injection Molded Long Glass Fiber Reinforced Thermoplastics

By

Hongyu Chen

Dissertation submitted to the faculty of the Virginia Polytechnic Institute and State University in partial fulfillment of the requirements for the degree of

DOCTOR OF PHILOSOPHY

In

Chemical Engineering

Donald G. Baird, Chairman

Peter Wapperom

Stephen M. Martin

Rickey M. Davis

Sep.20, 2018

Blacksburg, VA

Keywords: Long glass fibers; elastic properties; fiber orientation; fiber length; injection molding

Modeling of Microstructures and Stiffness of Injection Molded Long Glass Fiber Reinforced Thermoplastics

Hongyu Chen

Abstract

An enhanced demand for lightweight materials in automotive applications has resulted in the growth of the use of injection molded discontinuous fiber-reinforced thermoplastics. During the intensive injection molding process, severe fiber breakage arises in the plasticating stage leading to a broad fiber length distribution. Fiber orientation distribution (FOD) is another highly anisotropic feature of the final injection molded parts induced by the mold filling process. The mechanical and other properties can be highly dependent on the fiber length distribution and fiber orientation distribution.

The residual fiber length in the final part is of great significance determining the mechanical performances of injection molded discontinuous fiber reinforced thermoplastic composites. One goal of this research is to develop a fiber length characterization method with reproducible sampling procedure in a timely manner is described. In this work is also proposed an automatic fiber length measurement algorithm supported by Matlab®. The accuracy of this automatic algorithm is evaluated by comparing the measured results using this in-house developed tool with the manual measurement and good agreement between the two methods is observed.

Accurate predictions of fiber orientation are also important for the improvement of mold design and processing parameters to optimize mechanical performances of fiber-reinforced thermoplastics. In various fiber orientation models, a strain reduction factor is

usually applied to match the slower fiber orientation evolution observed experimentally. In this research, a variable strain reduction factor is determined locally by the corresponding local flow-type and used in fiber orientation simulation. The application of the variable strain reduction factor in fiber orientation simulations for both non-lubricated squeeze flow and injection molded center-gated disk, allows the simulated fiber re-orient rate to be dependent on the local flow-type. This empirical variable strain reduction factor might help to improve the fiber orientation predictions especially in complex flow, because it can reflect the different rates at which fibers orient during different flow conditions.

Finally, the stiffness of injection-molded long-fiber thermoplastics is investigated by micro-mechanical methods: the Halpin-Tsai (HT) model and the Mori-Tanaka model based on Eshelby's equivalent inclusion (EMT). We proposed an empirical model to evaluate the effective fibers' aspect ratio in the computation for the fiber bundles under high fiber content in the as-formed fiber composites. After the correction, the analytical predictions had good agreement with the experimental stiffness values from tensile tests on the composites. Our analysis shows that it is essential to incorporate the effect of the presence of fiber bundles to accurately predict the composite properties.

Modeling of Microstructures and Stiffness of Injection Molded Long Glass Fiber Reinforced Thermoplastics

Hongyu Chen

General Audience Abstract

An enhanced demand for lightweight materials in automotive applications has resulted in the growth of the use of injection molded discontinuous fiber-reinforced thermoplastics. The injection molding process results in fiber length and fiber orientation distributions in the final parts. The mechanical and other properties can be highly dependent on the fiber length distribution and fiber orientation distribution.

This work focuses on the process-structure-property relationship of fiber-thermoplastic composites. A novel fiber length measurement procedure and an automatic fiber length measurement tool were developed to improve the accuracy of fiber length measurement. The existing fiber orientation models have been improved by integration of the flow-type dependent fiber orientation kinetics. To improve the stiffness predictions, an empirical model has been developed to include the effects of fiber clumping on the elastic properties of injection molded fiber composites.

Acknowledgements

I would first like to express my thanks to my advisor, Dr. Donald G. Baird, who has been a great advisor, for his guidance and support which was necessary for the completion of this research. I would also like to offer special thanks to Dr. Peter Wapperom for his continuous involvement and for his constructive criticism that contributed greatly in my development as an researcher. In addition, I would like to thank my committee members, Dr. Stephen Martin and Dr. Richey Davis for their help and suggestiongs throughout this research project.

I would like to acknowledge current and past members of the polymer processing laboratory at Virginia Tech: Mark Cieslinski, Kevin Meyer, Gregory Lambert, Criag Mansfield, and Juan Pretelt. It was a great pleasure working with this group of individuals who are very supportive and helpful.

I was also greatly appreciate the help of the chemical department staff: Tina Russell, Diane Cannaday, Nora Bentley, Jane Price, Melanie Darden, Michael Vaught, Kevin Holshouser and Riley Chan.

Finally, I would like to thank my friends, family for their irreplaceable support and encouragement without which this dissertation would not have been possible.

Original Contributions

1. Developed a new fiber length measurement method with reproducible sampling procedure in a timely manner. This method can generate a relatively uniform sampling region through the entire thickness of the fiber stack, which help to reduce sampling bias from irregular sampling geometry. In addition, this new method applies an well-controlled down-sampling step which decreases the collected number of fibers that need to be characterized.

2. Proposed an automatic fiber length detection and measurement algorithm supported by Matlab®. The accuracy of this automatic algorithm was evaluated by comparing the codes determined results with those from manual measurement and good agreement between the two methods was observed.

3. Proposed using a variable strain reduction factor according to local flow-type in the fiber orientation simulation. This variable strain reduction factor might help to improve the fiber orientation predictions in complex flow, because it allows the simulated fiber re-orienting rate to be dependent on local flow conditions.

4. Investigated the concentration effect on the stiffness of glass fiber reinforced polypropylene composites. The effect fiber bundles in the fiber composites need to be included to accurately predict the composite properties. We proposed an empirical model to correct the fibers' aspect ratio in the computation due to the presence of fiber

bundles. After the correction, the analytical predictions had been improved compared to the results of tensile tests on the composites.

Table of Contents

List of Figures

Chapter 1 Introduction

The lightweight composite materials generated by the injection molding process have attracted great attentions stemming from the improved strength and stiffness over pure thermoplastics. First, in §1.1 a brief overview about fiber reinforced composites is given. Next, in §1.3 we briefly introduce the injection molding process. Then, in §1.3 we discuss the important microstructural variables of the fiber composites induced by the injection molding process. Finally, in §1.4 the objectives of this research are presented.

1.1 Fiber Reinforced Composites

Composites typically are made of two or more discrete materials, which help to enhance the mechanical or other properties of the resulting part relative to the main component [1]. Among this broad field, polymer based composites constitute the largest category [2]. As reinforcing constituents in a polymer matrix, fibers attract tremendous interest in the engineering community, because the strength and stiffness of materials in fiber form. Glass is the most commonly used type of commercial fiber, but carbon is used as well [3]. Fiber reinforced polymer composites are also in a wide variety of forms, ranging from discontinuous short fibers to oriented continuous fibers. Thermosetting resins are the most widely used matrix for continuous fiber polymer composites, while thermoplastic matrices are often used in discontinuous fiber reinforced polymer composites.

Our main interest is discontinuous long fiber thermoplastic composites (LFTs), because of their mechanical properties and the remained melt processbility. According to mechanical performance, fibers with length less than 1 mm were considered as short, while fibers greater than 1 mm are named as long [4]. Typically, LFTs have better mechanical properties over short fiber composties and still can be injection molded which reduces the manufacturing cost compared to continuous fiber reinforced composites.

1.2 Injection molding process

Injection molding is a robust and fast intermittent cyclic process [5], probably most widely used for producing uniform plastic articles with a high degree of geometrical complexity. Engineering thermoplastics and the corresponding fiber reinforced composites are very suitable for use with injection molding [3]. A typical injection molding machine is illustrated in Figure 1-1. First, polymer pellets are fed into the hopper and then mixed and melted by a reciprocating screw inside the heated barrel. The screw also acts as a ram that pushes the molten polymer rapidly into the cold mold, where the polymer begins to solidify. After solidification, the mold is opened and the finished part is ejected and removed. One production cycle is finished and next cycle is ready to start. The whole operation is nearly automatic.

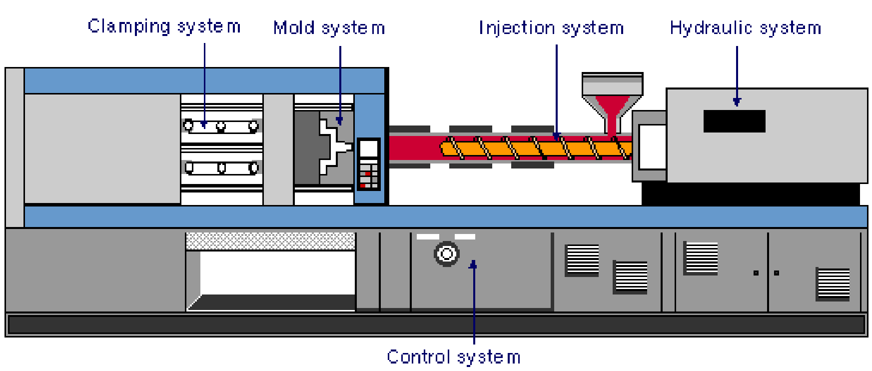

Figure 1-1: schematic representation of injection molding machine. Image obtained from Capetronics®.

1.3 Injection Molding Imparted Microstructural Variables

The complex combination of material and processing parameters during the injection molding of fiber reinforced composites will result in various microstructures in the final injection molded parts. Specifically, there are three important microstructures induced by the injection molding process: fiber length distribution (FLD), fiber orientation distribution (FOD) and fiber concentration [6]. Mechanical performances of the injection molded parts are highly dependent on these microstructures.

Injection molded articles produced by LFTs pellets (Figure 1-2) usually contain fibers of larger size exceeding significantly the aspect ratios found in conventional SFTs and thus offering improved mechanical properties than corresponding SFTs [7]. However, during injection molding, especially in the plasticating unit, severe fiber attrition would occur and lead to a distribution of fiber lengths in the final parts [3]. According to Baily and Kraft [8], significant attrition is already done mostly in the solid convey and melting section before the material entering the mold. So, understanding the mechanism of fiber breakage in the screw unit of injection molding machine will give insight to achieving longer fiber lengths.

A reliable experimental-evaluation of the fiber length of the injection molded parts, is the prerequisite to understand the fiber breakage mechanism. An ideal procedure for fiber length measurement is to do a full analysis of a sufficiently large sample which normally contains hundreds of thousands of fibers. However, the time-consuming analysis of such a large number of fibers might limit the application of this approach. A down-sampling step is commonly used to decrease the collected number of fibers that needs to be characterized from hundreds of thousands of fibers. The collection of the sub-sample is commonly done manually by collecting fibers at the location of interest using general tools like tweezers. However, the handling of the fibers with tweezers is quite arbitrary and results in the loss of very short fibers. So, it is of great importance to a new fiber length measurement method with reproducible sampling procedure in a timely manner.

Fiber orientation distribution also has significant influence on the mechanical properties of fiber thermoplastics composites [9, 10]. When fibers align in the direction of mechanical interest, greatest improvement on mechanical properties such as elastic modulus occurs [11]. The local alignment of fibers induced by the flow during injection molding is quite different, which makes mechanical properties vary accordingly. In order to optimize fiber orientation, it is important to understand the flow pattern and other features that will influence fiber orientation kinetics during mold filling.

Fiber concentration is another important factor that directly determines the mechanical performance of a composite [12]. Generally, various mechanical properties of glass fiber reinforced polypropylene increase with the fiber concentration up to 40 wt% [13]. In addition, fiber content is strongly related to fiber-fiber interactions in a suspension which is an important feature that influences both fiber attrition [7] and fiber orientation kinetics [14]. Generally, there are two criteria:

(i) An increase in fiber breakage with increasing fiber concentration;

(ii) A slower orientation evolution with increasing fiber concentration.

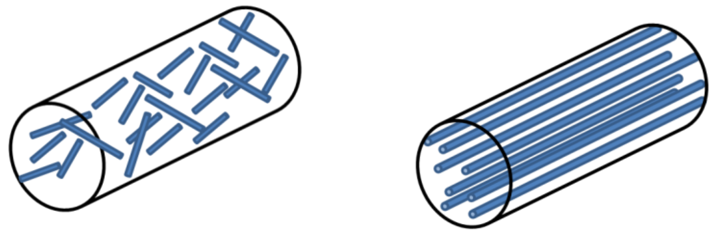

Figure 1-2: Short fiber and long fiber thermoplastic composite pellets used for injection molding.

1.4 Research Objectives

This research focus on the improvement in the characterization and prediction of microstructural variables related to the mechanical performance of the injection-molded fiber-composites. And the final objective is to perform stiffness predictions and gain better understanding toward the underlying influence of microstructural variables on the mechanical performances. As a result, three objectives have been proposed:

1. Improve the fiber length measurement technique by developing a new fiber length measurement method with reproducible sampling procedure in a timely manner. To reduce the manual work and speed up the whole fiber length measurement procedure, it is also of great importance to develop an automatic fiber detection and fiber length measurement tool supported by Matlab®.

2. Develop a method of using a variable strain-reduction factor in fiber orientation simulation. This variable factor would be determined by the local flow-type, since the flow pattern has a significant effect on the fiber orientation

kinetics. This method would allow the simulated fiber re-orient rate to be dependent on local flow conditions and might help to improve the fiber orientation prediction in complex flow.

3. Assess the ability of the existed analytical micro-mechanical models to predict the stiffness of the injection-molded long glass fibers reinforced thermoplastic composites with changes in concentration, fiber length and fiber orientation.

References

1. M.M. Schwartz, Composite materials handbook, McGraw-Hill, 1984.
2. T. Papthanasiou, D.C. Guell, Flow-induced alignment in composite materials, Elsevier, 1997.
3. J.H. Phelps, Processing-microstructure models for short-and long-fiber thermoplastic composites, ProQuest, 2009.
4. J. Crosby, Long-fiber molding materials, Elsevier Science Publishers BV, Thermoplastic Composite Materials, (1991) 139-165.
5. D.G. Baird, D.I. Collias, Polymer processing: principles and design, John Wiley & Sons, 2014.
6. G. Von Bradsky, R. Bailey, A. Cervenka, H. Zachmann, P. Allan, Characterization of finite length composites: Part IV-Structural studies on injection moulded composites (Technical Report), Pure and Applied Chemistry, 69 (1997) 2523-2540.
7. A. Hassan, R. Yahya, A.H. Yahaya, A.R.M. Tahir, P.R. Hornsby, Tensile, Impact and Fiber Length Properties of Injection-Molded Short and Long Glass Fiber-Reinforced Polyamide 6,6 Composites, Journal of Reinforced Plastics and Composites, 23 (2004) 969-986.
8. R. Bailey, H. Kraft, A Study of Fibre Attrition in the Processing of Long Fibre Reinforced Thermoplastics, International Polymer Processing, 2 (1987) 94-101.
9. S. Bapanapalli, B.N. Nguyen, Prediction of elastic properties for curved fiber polymer composites, Polymer Composites, 29 (2008) 544-550.
10. B.E. VerWeyst, C.L. Tucker III, P.H. Foss, J.F. O'Gara, Fiber orientation in 3-D injection molded features: prediction and experiment, International Polymer Processing, 14 (1999) 409-420.
11. B.N. Nguyen, S.K. Bapanapalli, J.D. Holbery, M.T. Smith, V. Kunc, B.J. Frame, J.H. Phelps, C.L. Tucker, Fiber Length and Orientation in Long-Fiber Injection-Molded

Thermoplastics — Part I: Modeling of Microstructure and Elastic Properties, Journal of Composite Materials, 42 (2008) 1003-1029.
12. J.L. Thomason, M.A. Vlug, Influence of fibre length and concentration on the properties of glass fibre-reinforced polypropylene: 1. Tensile and flexural modulus, Composites Part A: Applied Science and Manufacturing, 27 (1996) 477-484.
13. J.L. Thomason, The influence of fibre length and concentration on the properties of glass fibre reinforced polypropylene. 6. The properties of injection moulded long fibre PP at high fibre content, Composites Part A: Applied Science and Manufacturing, 36 (2005) 995-1003.
14. M.J. Cieslinski, P. Wapperom, D.G. Baird, Influence of fiber concentration on the startup of shear flow behavior of long fiber suspensions, Journal of Non-Newtonian Fluid Mechanics.

Chapter 2 Review of literatures

In this chapter a review of the literature concerning fiber breakage and fiber orientation for discontinuous fiber composites during processing especially during injection molding is presented. First, important microstructural variables of fiber composites are reviewed in section §2.1 which allow the reader to be familiar enough with the subject matter to understand the concepts presented throughout this review. Next, in §2.2 the theory and experimental investigation of fiber breakage during polymer processing are reviewed. Finally, in §2.3 the modeling of fiber orientation during flow is reviewed.

2.1 Microstructural Variables

Important microstructural variables for discontinuous fiber reinforced composites include: fiber concentration, fiber orientation and fiber length within the final parts[1]. The final composite properties are very much dependent on the microstructural variables [2]. In this section we will give an introduction to these three important variables.

2.1.1 Fiber Concentration

Fiber concentration directly influences mechanical properties of the final parts. Tensile, flexural and impact strengths have been reported to increase with fiber concentration till 40 wt% glass fiber content in polypropylene matrix [3-5].

Fiber concentration also has effects on the fiber motion (fiber-fiber interaction) in a flowing liquid (melted matrix polymer). Cieslinski et al. [6] observed that as long glass fiber concentration increased (10 wt% to 40 wt %), the stress growth overshoot measured in a sliding plate rheometer broadened which indicates slower orientation kinetics.

Based on the interactions a fiber has with its neighbors, Doi and Edwards [7]defined three concentration regimes for fiber suspensions, as shown in Eq. (2-1) to Eq. (2.3):

$$\phi_v < \frac{1}{a_r^2} \qquad \text{(dilute)} \tag{2-1}$$

$$\frac{1}{a_r^2} < \phi_v < \frac{1}{a_r} \qquad \text{(semi} - \text{concentrated)} \tag{2-2}$$

$$\frac{1}{a_r} < \phi_v, \qquad \text{(concentrated)} \tag{2-3}$$

where ϕ_v is the fiber volume fraction, and a_r is fiber the aspect ratio defined as $a_r = L/d$, where *L* is the fiber length and *d* the diameter of fiber. In the dilute region, the presence of a single fiber is completely unaffected by any other fibers. Specifically, fibers in a dilute suspension are free to move and rotate and cannot be affected by adjacent fibers. In this region, Jeffery's model can well describe the fiber motion. In the semi-concentrated region, the average spacing between the adjacent fibers is still greater than the fiber diameter, *d*, but less than *L*, and as a result, hydrodynamic interactions are frequent, but physical collision between fibers is still rare.

To meet the requirement of mechanical performance, the commercial fiber reinforced thermoplastic composites normally has a fiber content within the concentrated region which is also the major focus of our study. Non-hydrodynamic effects such as fiber-fiber interactions need to be considered this region. The orientation behaviors of fibers in dilute and non-dilute suspensions deviate significantly from each other [1].

2.1.2 Fiber Length

Fiber length is another important factor influencing the mechanical properties of discontinuous fiber thermoplastic composites [3, 8, 9]. Figure 2-1 shows the deformation of the matrix containing a fiber under tension. Due to the existed stress concentrations near the ends of the fiber, discontinuous fiber composites have worse mechanical properteis than continuous composites. Generally, the mechanical properties of the composites containing discontinuous fiber are proportional to fiber length and reach plateau at significant long length. According to the dependence of modulus on fiber length, short fibers are those with length smaller than 1mm, while long fibers have lengths greater than 1 mm.

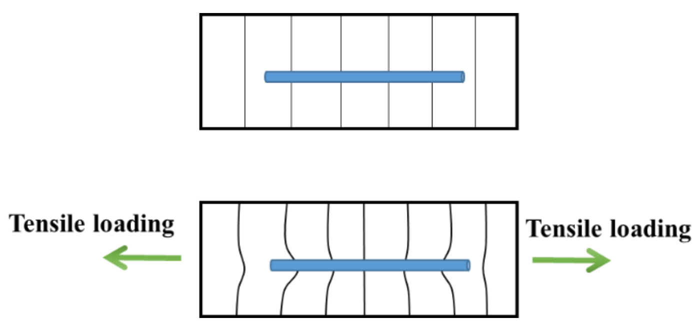

Figure 2-1: Schematic diagram showing the deformation of the polymer matrix containing a single fiber under tension.

Long fibers would experience deform and bend during complex flow. Switzer and Klingenberg [10, 11] proposed a dimensionless group to quantify the effective stiffness of a fiber as Eq. (2-4):

$$\mathrm{S}^{\mathrm{eff}} = \frac{E_y \pi}{64 \eta_m \dot{\gamma} a_r^4} \tag{2-4}$$

here E_y represents fiber's Young's modulus, η_m the matrix viscosity,and $\dot{\gamma}$ the shear rate. As $\mathrm{S}^{\mathrm{eff}}$ approaches 0, fibers behave completely like flexible threads, while for $\mathrm{S}^{\mathrm{eff}}$ approaching infinity, fibers turn out to be complete inflexible and preserve their rod shape in flow [12].

Typically, fiber composites show a normal distribution of fiber length with a long tail towards the longer fiber length. To concisely describe the overall length information for a fiber suspension, the number average and weight average fiber length summarize the fiber length distribution (FLD) information compactly by Eq. (2-5) and Eq. (2-6) respectively [13]:

$$L_n = \frac{\sum N_i \, l_i}{\sum N_i} \tag{2-5}$$

$$L_w = \frac{\sum N_i \, l_i^2}{\sum N_i \, l_i} \tag{2-6}$$

where, N_i is the number of fibers with length l_i. For L_n, all fiber lengths are weighted equally. While, for L_w implies, more weight are given to longer fibers.

To better reflect the steady shear viscosity, Huq and Azaiez [14] proposed a specific average fiber length, L_{HA}, for the fiber suspensions investigated, which is defined as:

$$L_{HA}^2 = \frac{\sum N_i \, L_i^3}{\sum N_i \, L_i} \tag{2-7}$$

This average gives more weight to longer fibers than the number or weight averages.

2.1.3 Fiber Orientation

A unit vector **p** is normally used to describe the alignment of a rigid fiber as shown in Figure 2-2, and its expression and components are shown in Eq. (2-8) to Eq. (2-11).

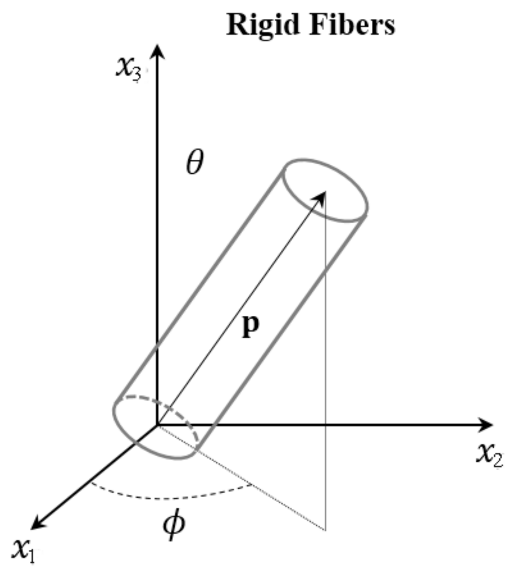

Figure 2-2: Schematic representation of a rigid particle orientation in 3-dimensional space by the vector, **p** which is characterized by the azimuthal and zenith angles ϕ and θ, respectively.

$$\mathbf{p} = \mathrm{p}_1\boldsymbol{\delta}_\mathbf{1} + \mathrm{p}_2\boldsymbol{\delta}_\mathbf{2} + \mathrm{p}_3\boldsymbol{\delta}_\mathbf{3} \qquad (2\text{-}8)$$

$$\mathrm{p}_1 = \sin\theta\cos\phi \qquad (2\text{-}9)$$

$$\mathrm{p}_2 = \sin\theta\sin\phi \qquad (2\text{-}10)$$

$$\mathrm{p}_3 = \cos\theta. \qquad (2\text{-}11)$$

For long fiber composites, a single vector **p** will no longer be able to represent the slightly bent fibers. Strautins and Latz [15] proposed a “bead-rod” model to describe the orientation evolution of slightly bended fibers. Flexible fiber is represented by two vectors, **p** and **q** connecting three beads. As a result, the alignment (orientation) of this slightly bended fiber is evaluated by the vector, $\underline{\mathrm{r}}$ (using $\underline{\mathrm{r}}$ to distinguish from the end to end tensor **r**) as shown in Figure 2-3. Detailed review of this model is given in §2.3.1.6.

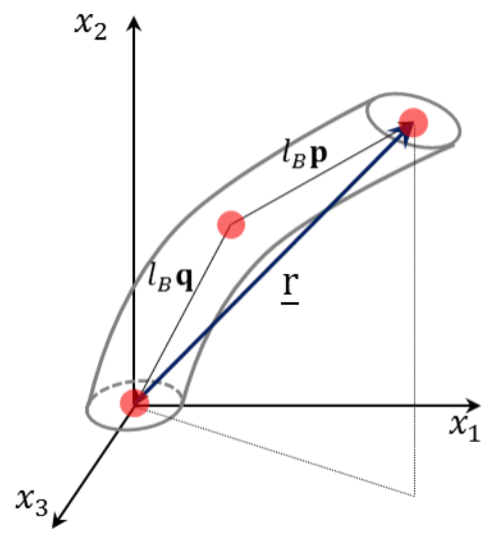

Figure 2-3: Schematic diagram of a semi-flexible fiber.

2.2 Fiber Breakage

The fibers in the composites have to be longer enough to sufficiently transfer the load from the polymer-matrix to the composites. And the threshold for this critical fiber length is given by [16]:

$$L_c = \frac{\sigma_f d}{2\tau_u}. \quad (2\text{-}12)$$

Here, σ_f is the fiber's tensile strength, d the fiber radius and τ_u the interfacial stress. During injection molding process, a great deal of damage to the fibers is quite normal, whid reduces average fiber length and the mechanical properties [17, 18]. It is, therefore, of great importance to understand the mechanisms for fiber breakage, so that systems can be designed to preserve fiber length as much as possible.

2.2.1 Mechanism

Fiber breakage during melt processing can arise from fiber-melt (polymer), fiber-fiber and fiber-machine interactions [19]. According to Phelps and Tucker [1], what is unclear is the effects of contact forces on fiber breakage. For example, fiber-fiber contact force may lead to fiber networks, which can even preserve the individual fibers from fiber breakage. So far, most of the fiber breakage modeling only considers the fiber-polymer interaction especially the stress exerted on the fiber surface by the polymer melt [20-22]. In Forgacs and Mason's [23] pioneer work, the tendency of rigid fibers to undergo rotation and buckling in simple shear flow was first analyzed. The center (mass) of the fiber was assumed to translate affinely with the bulk flow which is also the most likely location for buckling to occur [1, 24]. The total hydrodynamic force F acting on the central cross section of a single fiber along the axial in suspension is obtained from the integral:

$$F = -\int_{L/2}^{0} f(s)ds, \tag{2-13}$$

here, s is the local fiber coordinate along its axis , $L/2$ the half fiber length and $f(s)ds$ is the increment of force over the distance ds [23]. Based on Dinh and Armstrong's work [24], Phelps and Tucker [1] proposed that $f(s) = \zeta_p s \eta_m (\nabla\mathbf{v}\!:\mathbf{pp})$. Here ζ_p is a coefficient describing the drag on the fiber for relative motion parallel to its axis and treated as a fitting parameter, η_m the polymer matrix viscosity and $\nabla\mathbf{v}$ the velocity gradient tensor. Based on the slender-body theory for a dilute suspension, Burgers [25] proposed an expression for F:

$$F = -\int_{\frac{L}{2}}^{0} f(s)ds = \frac{M\pi\eta_m\dot{\gamma}L^2}{\ln 2a_r - 1.75}. \quad (2\text{-}14)$$

Here, $\dot{\gamma}$ is the shear rate and M the orientation factor for a single fiber defined as $M = \sin^2\theta \sin\phi \cos\phi$ where θ and ϕ are obtained from the orientation vector $\mathbf{p}$. The sign of F depends upon the fiber orientation relative to the flow field, which determines whether it is under compression or tension.

The buckling threshold, $F_{buckling}$, based on the Euler buckling model is described by:

$$F_{buckling} = \frac{\pi^2 E_y I}{KL^2}, \quad (2\text{-}15)$$

where, E_y is the Young's modulus, K column effective length factor and $I = \pi d^4/64$ (d is the fiber diameter) is the cross-sectional moment of inertia. By comparing the absolute value of negative F(compressive) in Eq. (2-14) with the value of $F_{buckling}$ in Eq. (2-15) a relation was developed for the critical value of $\eta_m\dot{\gamma}$ required to buckle a straight fiber in shear flow with several assumptions such as the particle is rigid and lying within the x-y plane, there is no Brownian motion and etc. This relation is defined as:

$$(\dot{\gamma}\eta_m) \cong \frac{E_y\,(\ln 2a_r - 1.75)}{2a_r^4}, \quad (2\text{-}16)$$

where a_r is the fiber aspect ratio and E_y the elastic modulus of fiber. The theory was tested experimentally by Forgacs and Mason [23] and the results generally indicated that theory of deformation was correct qualitatively.

Based on experimental data and the Euler Buckling theory, Bumm and White [26] developed a kinetic model to track the average glass fiber length evolution in the case that chopped fibers were fed into completely melted matrix materials in a twin screw extruder. Important parameters in this model were determined by the compressive force, F, exerted by the polymer-melt on the surfaces of the fibers and the buckling force, $F_{buckling}$, derived from Euler buckling theory. This model did not take account of the fiber-fiber, and fiber-machine interactions.

Durin et al. [27] proposed that flow-induced buckling is only due to flow-induced buckling. According to Durin et al. [27] a rotating rigid fiber in a shear flow might break into two child fibers under certain orientation state, when the fiber buckled (Figure 2-4). Indeed, when the sever tensile stress σ_s under deformation reaches the tensile strength value of the fiber σ_f, the break of fiber occurs. The sever tensile stress is a function of the fiber radius r_{radius}, its elastic modulus E_y and the local radius of curvature R:

$$\sigma_s(x) = \frac{E_y r_{radius}}{R(x)}, \tag{2-17}$$

where x is abscissa along the fiber principal axis. Durin et al. [27] validated in their work that, the fiber borke because of the buckling resulted huge deformation. Durin et al. [27] also mentioned that for flexible fiber, buckling threshold might be reached before breakage occurring, while, for weak fiber with defects, fiber breakage might occur without buckling. Based on these observation, Durin et al. [27] further suggested that the breakage probability for a single fiber should be proportional to the ratio between the compressive force in Eq. (2-14) (when it is negative) and the buckling force in Eq. (2-15). The force in Eq. (2-14) depended on the orientation **p** (or M). The breakage probability was computed by screening all the orientation sate and adding up all the probabilities of the occurrence of fiber breakage with the corresponding fiber orientaion. Based on the breakage rate obtained from the breakage probability, a new model predicting the fiber length distribution during processing was proposed. For detailed mathematical derivation, interested readers are referred to Durin et al. [27]. This model is derived from a slender-body theory for a dilute suspension. Another limitation is that it only includes the buckling mechanism, another important source, normal forces that act perpendicular to the fiber axis, is not considered.

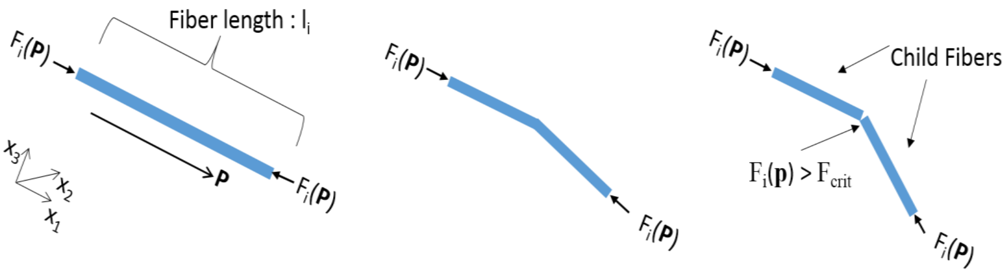

Figure 2-4: Buckling mechanism of fiber breakage in the Phelps-Tucker model.

Phelps and Tucker [22] used the steady state orientation distribution in simple shear flow to analyze the breakage of fibers with length l_i that the compression force at the center is larger than the critical buckling force. Finally, fiber orientation is decoupled from their breakage model and as a result breakage rate P_i for a fiber with length l_i is described by

$$P_i = \begin{cases} C_B\dot{\gamma}[1 - \exp(1 - B_i)] & \text{for } B_i > 1 \\ 0 & \text{for } B_i \leq 1 \end{cases}, \qquad (2\text{-}18)$$

where $\dot{\gamma}$ is magnitude of the deformation tensor, C_B a phenomenological parameter called the breakage coefficient which might help to include all the uncertain effects on fiber breakage, and B_i a dimensionless parameter defined as:

$$B_i = \frac{4\zeta_p \eta_m \dot{\gamma} l_i^4}{\pi^3 E_y d_f^4}. \tag{2-19}$$

Here ζ_p is a dimensionless drag coefficient, η_m the polymer matrix viscosity, E_y the elastic modulus of the fiber, and d_f the fiber diameter. Besides, a child generation rate R_{ji} was proposed to represent the rate of a fiber with length l_i to generate a child fiber with length l_j. In addition, R_{ji} is assumed to exhibit a Gaussian profile and be defined by:

$$R_{ji} = N_{PDF}\left(l_j, \frac{l_i}{2}, Sl_i\right), \tag{2-20}$$

where N_{PDF} is the normal probability density function, S the fitting parameter which controls the fiber length distribution shape. Child fiber generating rate R_{ji} is normalized for all possible child fibers with length l_j based on the breakage rate P_i

$$\sum_j R_{ji} = 2\, P_i. \tag{2-21}$$

Finally, a governing equation tracking the evolution of fiber length distribution information can be expressed as:

$$\frac{DN_i}{Dt} = -P_i N_i + \sum R_{ik}\, N_k \ (k \geq i), \tag{2-22}$$

here N_i and N_k are the number of fibers with the length of l_i and l_k respectively. Phelps and Tucker's [22] breakage model also neglected the pure bending mechanism for fiber breakage.

To reduce the computational time for the scenario only needs information of average fiber length evolution, an abbreviated model were developed and shown in Eq. (2-23):

$$\frac{DL_n}{Dt} = -\frac{1}{2} P_n L_n, \tag{2-23}$$

here L_n is the number average fiber length, and P_n denotes the function P_i (Eq. (2-18)) evaluated using the current value of L_n in place of l_i. This model only have two parameters: C_B and ζ of the original fiber breakage model.

The Phelps and Tucker's fiber breakage model has been implemented in Autodesk Moldflow [28]. Numerical examples showed that the implementation could predict a sandwich structure in terms of fiber length through the entire thickness of the sample. That was, longer fibers remained in the core region whereas fibers were uniformly broken down in the high shearing region. Meanwhile, quite some long fibers still remained in the skin region. This skin region reflected the fountain effect that the inner core fibers were turned onto the skin and quickly became frozen. Frederik [29] investigated the possible influence of the power law index of the polymer matrix on the fiber breakage by using Autodesk Moldflow software containing Phelps and Tucker's fiber breakage model. It was found that the lower the power law index, the lower the fiber breakage would be on average. This behavior is mainly caused by the difference in shear thinning behavior; the smaller the power law coefficient, the higher the shear thinning behavior and the smaller the region where high shear rates are present [30].

In a continuation of efforts, Forgacs and Mason [31] studied the deformation of suspended thread-like particles in simple shear flow. The conformation of the particles with increasing flexibility is shown in Figure 2-5 and the deformation was determined by both of the strength of flow and the intrinsic flexibility of the particle [32]. Salinas and Pittman [33] also studied fracture of fibers undergoing concentric cylinder shear flow and found that glass fibers will break with "snake" conformation.

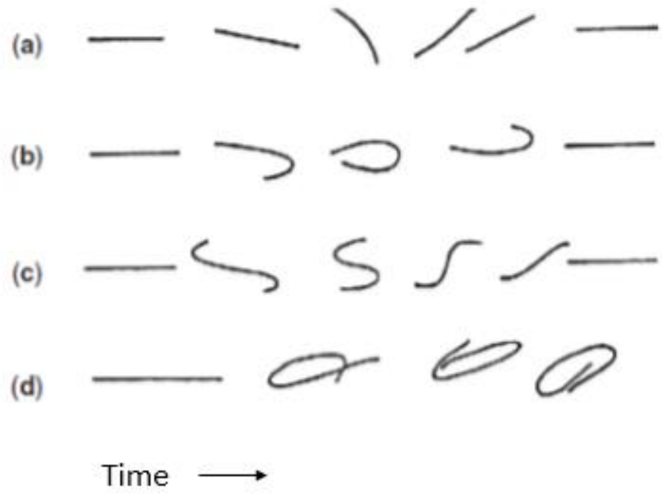

Figure 2-5: Fiber conformation in shear flow. The flexibility of particle increases from (a) to (d) [33].

The types of velocity field relative to the moving fiber axis has significant effect on the resulted viscous stress (hydrodynamic loading) on a single fiber. There are 4 possible situations as shown in Figure 2-6. Any efforts of predicting breaking criterion should clearly take into account the flexibility of the fibers and stresses of types (a) and (c) in Figure 2-6 [33]. However, the fiber breakage models based on buckling theory only account for the axial stresses in case (c) [27].

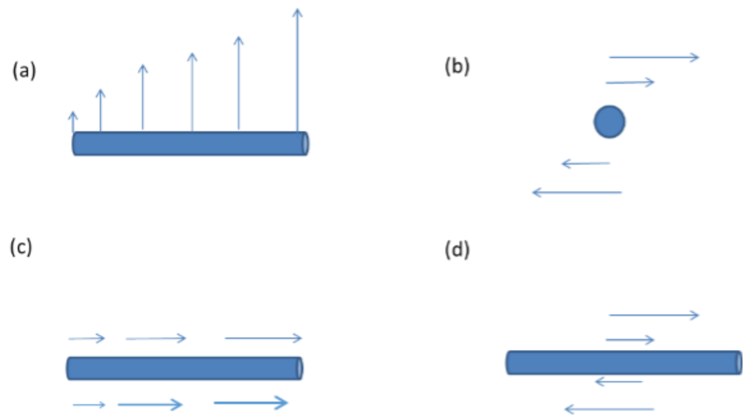

Figure 2-6: Schematic diagram of the the undisturbed flow field relative to the fiber, which can produce: (a) bending moments; (b) torsion about the fiber axis; (c) tensile (or compressive) axial stresses; and (d) rotational couple. Adapted from Salinas [33].

For glass fibers, there are three main types of breakage according to the types of applied force. The typical fractured cross-sections corresponding to the three types of breakage are shown in Figure 2-7 [34, 35]. Pu Ren et al. [36] investigated glass fiber breakage in the case where chopped fibers were fed in to melted polymer material in a two-stage single screw extruder. They checked the cross-sections of fiber fractures, and no twist break was found. The fibers with length of the order of 40 mm showed the characteristic of a tensile break cross-section. Cross-sections of the medium length fibers (5 mm to 40 mm) had both characteristics of tensile breaks and bend breaks. All the cross-sections of short fibers have the feature of bend break. The observations of Pu Ren et al. [36] were based on semi-concentrated to concentrated regions in an extrusion unit, but the results still indicated the importance of force types (a) and (c) in Figure 2-6 to fiber breakage.

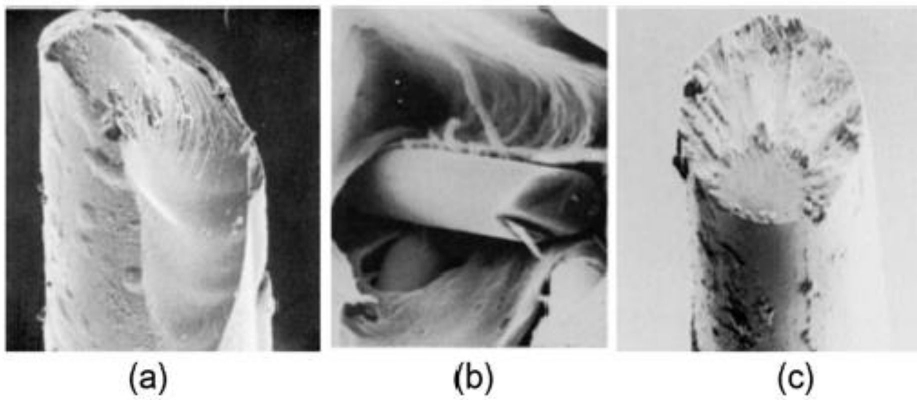

Figure 2-7: Cross-sections of fibers created by (a) twist, (b) bend, and (c) tensile [34].

Hinch et al. [37] considered (a) and (c) in Figure 2-6 and evaluated stresses using the slender body theory. Because the thickness (diameter) was neglected, the fiber was unable to sustain any bending moment, and stresses were thus purely tensile.

Salinas et al. [33] proposed that fibers broke because they were bent too sharply. An empirical model evaluating the critical radius, R_{break}, at the occurring of breaking, was given by:

$$\frac{2R_{break}}{d} = \frac{E_y}{T}, \tag{2-24}$$

here T is the ultimate tensile strength of the fiber. This model indirectly included both the pure bending and buckling mechanism for fiber breakage. The predicted results were in good agreement with the experimental data when hydrodynamic forces dominated.. However, this model has only been tested for dilute fiber suspensions in a Newtonian matrix, but still needs to be validated more intensively under more realistic polymer processing conditions.

Using Salinas and coworker's [33] theory, Kabanemi et al. [38] carried out a simulation of pure fiber bending in simple shear flow. Each fiber was represented as a series of rigid beads connected by elastic springs. Bending deformation was modeled by two adjacent bonds defined by three adjacent sphere as shown in Figure 2-8. The numerical predictions qualitatively matched with experimental data [33]. However, the twisting deformation proposed by the authors [38] in the model development section was neglected. Besides, direct simulation was too cumbersome to be applied for real polymer processing, e.g. concentrated regime.

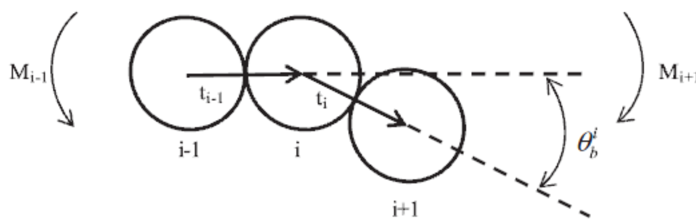

Figure 2-8: Schematic diagram showing deformation due to bending made by two adjacent bonds [38].

The above fiber breakage models have limitations. First, only the axial mechanical properties of the fiber are considered for developing them. These models need to be validated more intensively for fibers with anisotropic mechanical properties, e.g. carbon fibers [39]. Second, these fiber breakage models only account for the fiber-polymer interaction mechanism; indeed, most of the fiber length reduction occurs in the solid convey and melting zones of the plasticating unit because of the fiber-fiber and fiber-machine interactions and the effect of fiber-fiber interaction on fiber breakage in mold filling process is still not clearly understood [32, 40].

Mittal et al. [41] proposed a breakage mechanism including both bending and buckling of the fibers during extrusion process. The authors believed most of the fiber breakage occurred in the transition zone. A single fiber constrained in the solid bed with one end will no longer be able to freely rotate and orient in the suspension. Normal forces vertical to the fiber axis will be induced on the extruded section of the anchored fiber. As a result those fibers may be broken from the solid bed due to pure bending. The broken pieces will start flowing with polymer and experience further breakage due to excessive deformation like buckling. This work is more like an extended application of the fiber-polymer interaction mechanism to the extrusion process. It should be noted that any fiber attrition in the solid-convey region was ignored in this work. Besides, this study only considered the flow induced fiber breakage and excluded the fiber-fiber interaction effects.

Bereaux et al. [42] applied Mittal and coworker's [41] fiber breakage model to the extrusion process for long fiber reinforced composites. The experimental and computed length matched well with each other. However, their method of extending this specific single fiber breakage model to track the fiber length distribution evolution for a population of fibers was not explained in any detail.

Wolf et al. [43] identified possible mechanisms of fiber breakage specific to the plasticating process. These mechanisms include: squeezing of solid pellets at the inlet, interaction among granules at solid conveying region, friction between granules and the flight clearance, the barrel wall and the screw root, and finally the bending of fibers in the melt. The majority of these mechanism are presented in Figure 2-9. Notably, Wolf and coworkers [43] found that the extent of pinch of pellets occurred at the inlet was determined by the ratio between the channel depth and the pellet size. The breakage mechanism in the transition zone proposed by Wolf was very similar to Mittal's theory, which is based on Tadmor's melting pattern [44]. Specifically, in the transition zone, fiber touching or passing the gap between the barrel and the solid bed would experience breakage due to shear or friction. In the metering zone, fiber breakage can be explained by the fiber buckling theory in suspension. However, the effect of pressure buildup and fiber-fiber interaction in that area should also be considered [43].

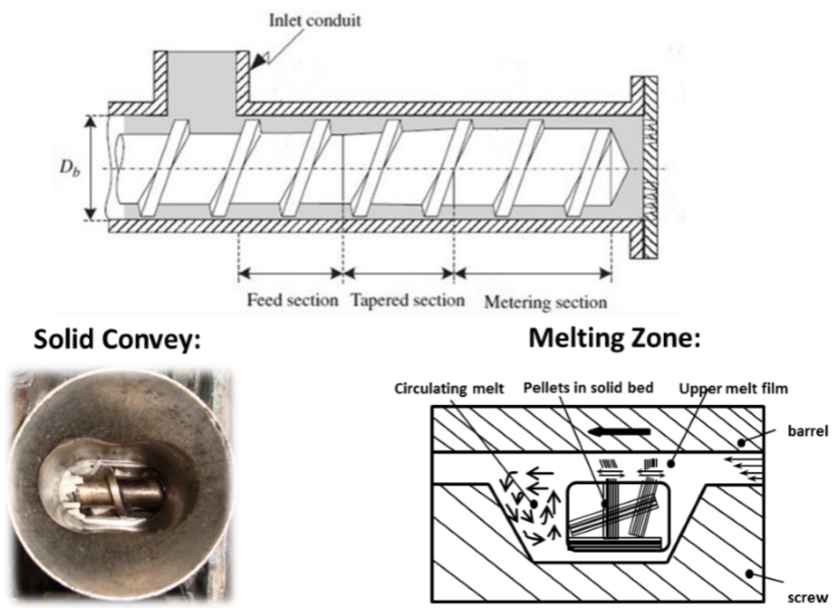

Figure 2-9: Major fiber breakage mechanism in the screw plasticating unit.

In contrast to in-suspension fiber breakage, in-machine fiber breakage is much more complicated to describe mathematically. Several authors used empirical models to track the average fiber length evolution during screw processing [26, 45, 46]. Typically, these empirical models are described by:

$$\frac{dL}{dt} = -k(L - L_{\infty}), \tag{2-25}$$

where, L is the number or weight average fiber length, L_∞ is the corresponding unbreakable fiber length in that system, t is the residence time, and k the kinetic constant treated as a fitting parameter. Inceoglu et al.[45] added a specific mechanical energy (SME) term to this type of model, which allowed them to correlate the rates of fiber length degradation in different devices including both lab-scale and industry scale extruders. However, this model only predict fiber breakage after the melting zone [47] since it only consider the breakage mechanism of melt induced fiber buckling.

2.2.2 Effect of Processing on Fiber Breakage

Injection molding of long fiber thermoplastics pellets (Figure 1-2) leads to final parts in which average fiber length (L_n &L_w) is much higher than that in the conventional injection molding short fiber reinforced thermoplastics. However, few fibers of the original fiber length will survive during injection molding. According to Bailey et al. [17], most of the breakage occurs in the plasticating unit. It is of great significance to gain understanding toward the effect of processing conditions such as screw speed, screw size, compression ratio and rate, back pressure, injection speed, gate size, and nozzle design on fiber breakage.

Gupta et al. [20] investigated the fiber length distribution along the screw channel with a special designed screw from which the frozen material filling the channel can be easily unloaded in the frm a helix. They measured fiber length distribution of samples at different channel locations, and found that the number average fiber length can be reduced from initially 9 mm to around 1 mm at the last channel of the screw. Gupta et al. [20] also revealed that fiber breakage occurred predominantly from the 7th to the 12th channel.

Wolf et al. [43] investigate the effects of different processing conditions on fiber breakage in a single screw extruder. Final average fiber length increased as screw speed increased from 25 rpm to 70 rpm. This finding is similar to the work of Lafranche and coworkers [48], which showed that the extent of fiber breakage was reduced as the increase of the screw speed. However, some authors have observed that low screw rotation speed may help to decrease the fiber degradation [32, 49]. For the simulation side, Bereaux et al. [42] suggested that screw speed had a very complex influence on fiber breakage and it was hard to make any conclusive conclusion. The effect of screw speed on fiber length attrition still remains controversial and needs to be debated.

Wolf et al. [43] also found that the phase change (melting) speed was an important factor influencing the fiber attrition. A rapid phase conversion resulted in a severe separation between the solid layer and the fibers in the melt pool resulting increased fiber breakage. On the other hand, a slow and gradual conversion was conducive in preserving the fiber bundles. The phase transition speed was related to the compression rate and ratio of the screw. Typically, a short compression section with low barrel temperatures would lead to fast phase conversion which is detrimental for preserving fiber bundles. Similarly, Lafranche et al. [48] also suggested that improvement of the residual fiber lengths could still be achieved with a lower compression ratio of the screw, a longer melting zone (lower compression rate), and larger melt channels. According to Campbell et al. [50] the channel pressures increased with increasing compression ratio (and compression rate). Pu Ren et al. [36] suggested that only when the pressure reached a threshold value, the melt could effectively impregnate the internal region of the fiber agglomerates.

Another factor influence the fiber length degradation is the fiber concentration [6, 32, 51]. Joshi et al. [52] found that fiber attrition increased with glass fiber content due to increased fiber-fiber interactions with higher fiber content. Bijsterbosch et al. [53] found that the average fiber length decreased from 1.6 mm to 0.6 mm as fiber concentration was increased from 2 vol% to 25 vol%. Fu et al. [19] found that the degradation of carbon fiber followed the same trend as glass fiber where the mean fiber lengths decreased with increasing fiber volume content.

The effect of injection molding variables on the length of fibers has been widely studied. Villarroel et al. [54] found that increasing injection velocity resulted in a higher extent of fiber length degradation, as a result the mechanical properties also experienced degradation. They also noticed that fiber length and mechanical properties are independent of melt temperature and cycle time. According to Tremblay [55], high injection speed resulted in higher fiber attrition. Cianelli et al. [56] found that attrition of glass fiber was very sensitive to injection molding conditions such as screw speed, back pressure, screw speed, injection speed and etc. Basically, severer processing conditions resulted in greater fiber attrition. Bailey et al. [17] have related the significant reduction of fiber length to the using of higher backpressure, showing backpressure was more influential than injection speed [57]. In the plasticating unit of injection mold machine, melt is constantly transferred to the screw tip, and a pressure is gradually built up to push the screw to move back. In order to preventing screw back too fast and ensure uniform melt mixing, a pressure in the opposite direction is applied. Generally, higher back pressure corresponds to longer residence time.

Besides the controllable injection molding parameters, other factors might also impact the fiber breakage. Bijsterbosch et al. [53] noticed that fiber attrition during injection molding was also dependent on the degree of impregnation of fibers. Results indicated that poorly impregnated fibers (impregnation < 10%) experienced greater degree of fiber attrition and turned out to have lower mechanical properties. Hamada et al. [58] suggested that coating silane treated fiber surface with polyamide (PA) sizing agent helped to reduce fiber fracture during polymer processing. Pu Ren et al. [36] commented that coupling agent can also enhance the adhesion between the individual fibers which would be detrimental to fiber dispersion. However, the authors did not study the effect of coupling agent on fiber breakage. It is intuitive to speculate that coupling agent might help to preserve fiber length.

Baily et al. [17] related the pseudoplastic properties of the melt to the gate size and assessed the effect of gate size on fiber breakage. In a smaller gate, with the same volumetric flow rate materials experienced greater pseudoplasticity and as a result the flow pattern tended towards plug flow. The higher shear rate near the wall and the corresponding greater shear thinning effect contributed to this phenomenon. The net results of these effects would be the small gate giving rise to a very high level of fiber attrition near the wall, and reduced fiber breakage in other locations because of lower shear forces. The large gate would produce relatively more Newtonian flow, which would give rise to fiber breakage across the entire thickness, but to a lower degree compared to narrower gate.

It is a general and intuitive finding that mild processing conditions like slow screw speed, low back pressure, low injection speed, and slow phase conversion might help to reduce fiber breakage. However, studies on the effect of screw geometry, like the screw diameter, channel width and depth on fiber breakage are seldom reported. These factors may also significantly influence the fiber breakage during polymer processing.

2.3 Numerical Predictions of Fiber Orientation Evolution during Flow

The predictions of fiber orientation during mold-filling of the injection molding process is quite important, since it give insight into the improvement of mold design favoring the increase of mechanical properties of the final injection molded parts. In §2.3.1 the equations for modeling the evolution of fiber orientation during flow are introduced. In §2.3.2 the development of stress models for fiber suspension systems is discussed. Finally, in §1.1.2 numerical simulations of fiber orientation will be reviewed.

2.3.1 Orientation Evolution Models

In order to optimize the design of an injection mold so as to obtain a part with desired properties, it is important to find the reliable mathematical model to describe the evolution of fiber orientation during flow. Therefore, the equations for tracking fiber orientation and the corresponding closure model for the fourth order orientation tensor will also be reviewed in this section.

2.3.1.1 Jeffery's Equation

The pioneering work of Jeffery [59] described the motion of fiber in flow with dilute fiber concentration in the absence of fiber-fiber interactions. Jeffery's model described the angular evolution of an ellipsoid in simple shear flow with $v_1 = \dot{\gamma} y$, $v_2 = v_3 = 0$ which is given by:

$$\frac{\partial \theta}{\partial t} = \xi \frac{\dot{\gamma}}{4} \sin 2\theta \sin 2\phi \tag{2-26}$$

$$\frac{\partial \phi}{\partial t} = \frac{\dot{\gamma}}{a_r^2 + 1} (a_r^2 \cos^2\phi + \sin^2\phi), \tag{2-27}$$

where $\xi = \frac{a_r^2 - 1}{a_r^2 + 1}$ defines the shape of the ellipsoid. The periodic motion has been commonly named as the Jeffery orbit [23] (Figure 2-10) and the period, T, is defined by:

$$\mathrm{T} = \frac{2\pi}{\dot{\gamma}}\left(a_r + \frac{1}{a_r}\right). \tag{2-28}$$

The motion of a single fiber can be further written in vector form given as [60]:

$$\frac{\partial \mathbf{p}}{\partial t} + \mathbf{v} \cdot \nabla \mathbf{p} = \mathbf{W} \cdot \mathbf{p} + \xi[\mathbf{D} \cdot \mathbf{p} - (\mathbf{p} \cdot \mathbf{D} \cdot \mathbf{p})\mathbf{p}] \tag{2-29}$$

where $\mathbf{v}$ is the velocity vector, $\mathbf{W} = \frac{1}{2}[(\nabla \mathbf{v})^t - \nabla \mathbf{v}]$ the vorticity tensor, and $\mathbf{D} = \frac{1}{2}[\nabla \mathbf{v} + (\nabla \mathbf{v})^t]$ the rate of deformation.

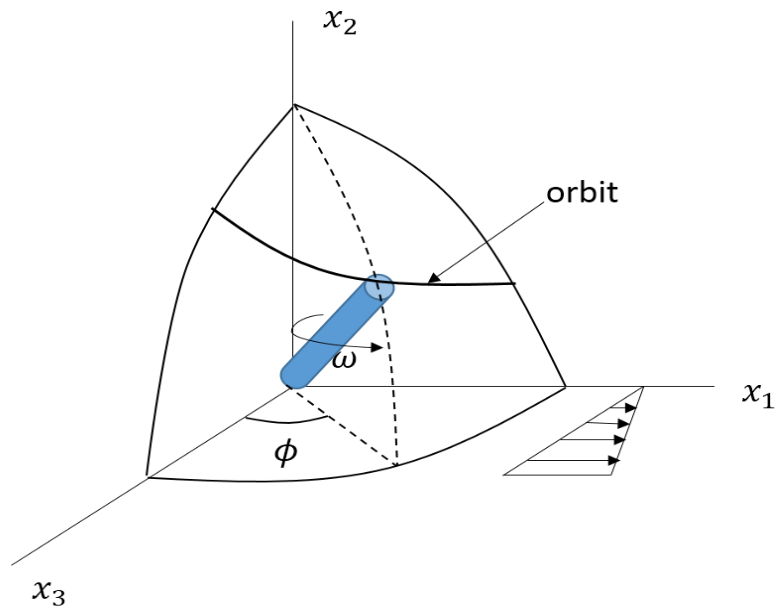

Figure 2-10: Schematic representation of Jeffery Orbit in simple shear flow (the particle also undergoes spin about its major axis at an angular velocity ω).

The orientation model described in Eq. (2-29), tracking the orientation for a single fiber, is too cumbersome for describing the orientation state of a large population of fibers in a suspension. However, the probability distribution function $\psi(\theta, \phi)$ or $\psi(\mathbf{p})$ is a statistical, unambiguous description of the orientation state for a population of particles in a suspension. Specifically, the orientation distribution function represents the probability that a fiber will be orientated between the angles (θ, ϕ) and $(\theta + d\theta, \phi + d\phi)$. The function ψ must obey several physical rules. First, the orientation of a particle is indistinguishable between a vector **p** and **–p,** so the value of ψ has to be periodic and follows: $\psi(\mathbf{p}) = \psi(-\mathbf{p})$. Second, the normalization condition must be satisfied such that the function summed over all orientation states must equal unity.

To describe the change in ψ with time when fibers are re-orientating during flow, a Smoluchowski equation is defined as [61]:

$$\frac{D\psi(\mathbf{p})}{Dt} = -\frac{\partial}{\partial \mathbf{p}} \cdot (\psi(\mathbf{p})\dot{\mathbf{p}}). \qquad (2\text{-}30)$$

The substitution of Eq. (2-29) into Eq. (2-30) provides a description for the evolution of fibers' orientation in dilute suspensions. However, numerical simulation tracking the evolution of ψ is too cumbersome, because ψ is a function of θ and ϕ, and as a result the discretization of θ and ϕ in space will generate a formidable amount of information during a simulation. To compactly describe the orientation state for a population of fibers, structure tensors have been widely used in fiber orientation models. This method was explored by Erickson [62-64] for liquid crystalline polymers and later applied by Advani and Tucker [61] to describe the orientation state for a population of fibers. The second and fourth order orientation tensors are given by:

$$\mathbf{A} = \langle \mathbf{pp} \rangle = \int \mathbf{pp}\psi(\mathbf{p}, t)\, \mathrm{d}\mathbf{p} \tag{2-31}$$

$$\mathbf{A_4} = \langle \mathbf{pppp} \rangle = \int \mathbf{pppp}\psi(\mathbf{p}, t)\, \mathrm{d}\mathbf{p}. \tag{2-32}$$

Odd moments of orientation are zero because the function itself is even for axisymmetric particles. Additionally, trace of $\mathbf{A}$ always equals 1 according to the normalization condition. Furthermore, higher order tensors provide complete information about lower orders, because of the existence of the following relationships $A_{ijkk} = A_{ij}$ and $A_{ijklmm} = A_{ijkl}$.

By multiplying Eq. (2-30) by $\mathbf{p}$, a new continuum form of Jeffery's equation based on the second and fourth order tensors is then given as:

$$\frac{D\mathbf{A}}{Dt} = \frac{\partial \mathbf{A}}{\partial t} + \mathbf{v} \cdot \nabla\mathbf{A} = \mathbf{W} \cdot \mathbf{A} - \mathbf{A} \cdot \mathbf{W} + \xi(\mathbf{D} \cdot \mathbf{A} + \mathbf{A} \cdot \mathbf{D} + 2\mathbf{D} : \mathbf{A_4}). \tag{2-33}$$

To get the values for the fourth-order tensor $\mathbf{A_4}$, a closure approximation based on the second-order tensor are necessary during the simulation. The second-order tensor is the most concise non-trivial description of orientation, and would provide the most efficient calculations [65]. Instead of using closure approximations, the evolution of higher order tensors can still be developed using the same method [61, 66].

2.3.1.2 Folgar-Tucker model

The fiber-fiber interactions plays an important role determining the orientation state of fibers in concentrated regime [67]. Moreover, it was experimentally observed that the behaviors of fibers deviated increasingly from Jeffery's theory as the concentration increased [68-70]. Folgar and Tucker [71] included fiber-fiber interactions for non-dilute systems and developed their model extended from Jeffery's model. An isotropic rotary diffusion term has been added into Eq. (2-29) and the model in tensor format is given by:

$$\frac{D\boldsymbol{A}}{Dt} = \mathbf{W}\cdot\mathbf{A} - \mathbf{A}\cdot\mathbf{W} + \xi(\mathbf{D}\cdot\mathbf{A} - \mathbf{A}\cdot\mathbf{D} + 2\mathbf{D}:\mathbf{A_4}) + 2C_I\dot{\gamma}(\mathbf{I} - 3\mathbf{A}), \qquad (2\text{-}34)$$

here C_I is a phenomenological constant and **I** the unit tensor. The interaction between fibers is quite an inherent property of the concentrated fiber suspension. Additionally, values of C_I must be determined from experimental data [71, 72]. Addition of this rotary diffusion term was shown to improve the predictions considerably in comparison with Jeffery's equation [72].

The fiber interaction coefficient, C_I, has been extensively studied, but by far an well accepted empirical model of the interaction coefficient still does not occur [73]. Yamane et al. [74, 75] performed numerical simulations on semi-dilute suspensions using values of C_I of order $10^{-7}\sim10^{-4}$. Yamane et al. [74] suggested that C_I increased with the increase of concentration, since the collisions took place more frequently at higher concentration. From the damped oscillations in fiber orientation, an empirical relationship of C_I for semi-dilute concentration was obtained as follow [74]:

$$C_I = 0.011(nL^3)^{1.10}a_r^{-1.47}, \qquad (2\text{-}35)$$

where n is the density of fibers, L the fiber length and a_r the aspect ratio of fiber.

In the concentrated region, increased fiber interactions are represented by larger values for C_I than what is reported for semi-dilute suspensions. Phelps et al. [1] suggested that the values of C_I are in a range of 0.003 – 0.016 for rigid fiber suspensions in the concentrated regime. Several researchers [71, 76, 77] also indicated that C_I is a function of fiber volume concentration and fiber aspect ratio.

Ranganathan et al. [77] proposed an average inter-fiber spacing a_c which is dependent on both fiber orientation and fiber length [24]. They [78] suggested that the degree of fiber-fiber contacts should vary inversely with the inter-fiber spacing and derived a linear inverse relation between C_I and a_c as:

$$C_I = \frac{K}{a_c/d}, \tag{2-36}$$

here d is the fiber diameter, and K is a proportionality constant. This formulation allows the interaction coefficient to change with orientation state, but rotary diffusion still remains isotropic.

Bay et al. [79] have estimated an empirical model for the interaction coefficient that best fit the observed experimental values of orientation state, which is described by:

$$C_I = 0.0184 \exp(-0.7148\phi_v a_r), \tag{2-37}$$

where ϕ_v is the volume fraction of fibers, and a_r the fiber aspect ratio. This model is opposed to the trend observed by Folgar et al. [71]. The author argued that a caging effect proposed by Doi and Edwards [80] might help to explain this trend, because the increased fiber volume resulted in increased fiber-fiber interactions, as a result the motion of fibers turned out to be more difficult. Bay et al. [79] has also pointed out that the distribution of fiber lengths in the suspension was important. The suspension concentration classification assumed that L and d were constant in the suspension, and a new scaling that accounted for the actual distribution of fiber lengths might help to explain the different C_I trends between their's and Folgar's work.

Phan-Thien and coworkers [76] considered both long-range and short-range hydrodynamic interactions among fibers during their simulation for a fiber suspension in a Newtonian fluid. As a result, they proposed an expression for the isotropic rotary diffusion constant as:

$$C_I = 0.03[1 - \exp(-0.224\phi_v a_r)]. \tag{2-38}$$

The value of C_I increases monotonically with $\phi_v a_r$. Additionally, at an infinitely low concentration, C_I equals zero indicating the motion of fiber does not deviate from Jeffery's orbit in the absence of fiber interaction.

2.3.1.3 Strain Reduction Factor (SRF) Model

Although the standard Folgar-Tucker model is commonly used and well recognized by both of the academic and industrial societies [72, 79, 81], experimental evidence including measurements of fiber orientation and rheological measurements of stress growth show that the orientation kinetics in concentrated fiber systems evolved slower than Folgar-Tucker model predicted [82-84]. A slip parameter, α, which has a value between 0 and 1 was suggested to slow down the predicted fiber orientation rates to better reflect the experimental observed trends [84-86], as seen in Eq. (2-39):

$$\frac{D\mathbf{A}}{Dt} = \alpha[\mathbf{W}\cdot\mathbf{A} - \mathbf{A}\cdot\mathbf{W} + \xi[\mathbf{D}\cdot\mathbf{A} + \mathbf{A}\cdot\mathbf{D} - 2\mathbf{D}:\mathbf{A_4}] + 2C_I\dot{\gamma}(\mathbf{I} - 3\mathbf{A})]. \quad (2\text{-}39)$$

The addition of the empirical parameter α leads to improved accuracy of the simulation, but it also results in a loss of material objectivity [87]. If the coordinate frame were to rotate, translate or change to a different coordinate system, the computations could produce non-physical results.

2.3.1.4 Reduced Strain Closure (RSC) Model

To maintain the objectivity, Wang and coworker [87] developed the reduced strain closure (RSC) fiber orientation model, in which only the evolution rate of the eigenvalues of the orientation tensor were reduced by an empirical factor $\kappa < 1$, with the eigenvectors unchanged. This objective model is summarized in Eqs. (2-40) to (2-42), where $\mathbf{L_4}$ and $\mathbf{M_4}$ are additional fourth order tensors, and λ_i and $\boldsymbol{e_i}$ are the eigenvalues and eigenvectors of $\mathbf{A}$, respectively:

$$\frac{D\boldsymbol{A}}{Dt} = \mathbf{W}\cdot\mathbf{A} - \mathbf{A}\cdot\mathbf{W} + \xi\{\mathbf{D}\cdot\mathbf{A} + \mathbf{A}\cdot\mathbf{D} - \mathbf{2}[\mathbf{A_4} + (1-\kappa)(\mathbf{L_4} - \mathbf{M_4}:\mathbf{A_4})]:\mathbf{D}\} + 2C_I\dot{\gamma}(\mathbf{I} - 3\mathbf{A}) \quad (2\text{-}40)$$

$$\mathbf{L_4} = \sum_{i=1}^{3}\lambda_i(\boldsymbol{e_i e_i e_i e_i}) \quad (2\text{-}41)$$

$$\mathbf{M_4} = \sum_{i=1}^{3}(\boldsymbol{e_i e_i e_i e_i}). \quad (2\text{-}42)$$

The value of κ is generally in a range between 0.05 and 0.2. In addition, this factor is determined by the intrinsic property of the fiber suspension. For example, Tucker [88] pointed out two significant criteria:

(i) A decrease in the κ value corresponds to an increase in fiber length and fiber concentration, as well as a decrease in matrix viscosity [84].

(ii) The increase of κ value leads to an increase in fiber elastic modulus.

Mazahir et al. [89] conducted fiber orientation simulations with both the SRF and RSC models and compared the predictions with experimental measurements. They found that both models provided similar predictions in the transient and steady regions in terms of fiber orientation kinetics.

2.3.1.5 Anisotropic Rotary Diffusion (ARD) Model

Nguyen et al. [90] has reported that for long-fiber thermoplastics the model need to be further modified to increase accuracy. It appears that an modification of C_I are necessary to make the rotary diffusion to be dependent on the anisotropic fiber orientation states [65]. Koch et al. [91] accounted for the anisotropic nature of fiber suspensions and proposed anisotropic diffusion as a function of the fourth and sixth moments of orientation. Koch's theory was based on a semi-dilute suspension including the effects from long-range hydrodynamic fiber-fiber interactions [1]. Phelps and Tucker [40] tested the Koch model using the moment-tensor notation and found that it provided no advantage for predicting fiber orientation in LFTs Composites. Fan [92] and Phan-Thien et al.[76] developed a diffusion contribution term making A follow the symmetry requirement. Phan-Thien et al. [76] further modified the equations from Fan et al. [92] to make sure the trace of **A** is always equal to 1. But, the major flaw of their model was that the diffusion contribution did not equal zero when fibers are isotropically distributed [1]. Realizing the drawbacks of the above mentioned theories, Phelps and Tucker [40] developed a new rotary diffusion which is a dependent on the rate of deformation, $\mathbf{D}$, the second moment of fiber orientation, $\mathbf{A}$, and constants $b_1 - b_5$ being empirically fit parameters shown in Eq. (2-43):

$$\mathbf{C_A} = b_1\mathbf{I} + b_2\mathbf{A} + b_3\mathbf{A}^2 + \frac{b_4}{\dot{\gamma}}\mathbf{D} + \frac{b_5}{\dot{\gamma}}\mathbf{D^2} \tag{2-43}$$

Phelps et al. [40] developed an anisotropic form of the reduced strain closure model known as ARD-RSC model, shown in Eq. (2-44):

$$\begin{aligned}\frac{D\mathbf{A}}{Dt} = &\ \mathbf{W}\cdot\mathbf{A} - \mathbf{A}\cdot\mathbf{W} \\ &+\xi\{\mathbf{D}\cdot\mathbf{A} + \mathbf{A}\cdot\mathbf{D} - \mathbf{2}[\mathbf{A_4} + (1-\kappa)(\,\mathbf{L_4} - \mathbf{M_4}\!:\mathbf{A_4})]\!:\mathbf{D}\} \\ &+\dot{\gamma}\{2[\mathbf{C_A} - (1-\kappa)\mathbf{M_4}\!:\mathbf{C_A}] - 2\kappa tr(\mathbf{C_A})\mathbf{A} - 5(\mathbf{C_A}\cdot\mathbf{A} + \mathbf{A}\cdot\mathbf{C_A}) \\ &+10[\mathbf{A} + (1-\kappa)(\,\mathbf{L_4} - \mathbf{M_4}\!:\mathbf{A_4})]\!:\mathbf{C_A}\}\end{aligned} \tag{2-44}$$

This ARD tensor $\mathbf{C_A}$ based on Hand's [93] tensor is difficult to apply in general, because numerous parameters themselves are so sensitive as to affect the stability of numerical results. Phelps and Tucker [40] further reported two points to evaluate the ARD tensor: (i) Three of these parameters, b_1, b_2, and b_4 are selected by matching experimental orientation tensor data; (ii) the residual parameters, b_3 and b_5, serve to ensure a stable convergence in numerical computation. The lack of simple criteria for determination of parameters and lack of physical meaning of the parameters are the model's major shortcomings [94]. To address these critical problems, Tseng et al. [94] proposed an improved ARD (iARD) model and yielding the new anisotropic rotary diffusion term given by:

$$\dot{\mathbf{A}}^{iARD} = 2C_I\dot{\gamma}(\mathbf{I} - 3\mathbf{A})$$
$$+2\dot{\gamma}C_I C_M \left\{(\mathbf{A} - \tilde{\mathbf{L}}) + 5[\frac{1}{2}\mathbf{A}\cdot\tilde{\mathbf{L}} + \frac{1}{2}(\mathbf{A}\cdot\tilde{\mathbf{L}})^{\mathrm{T}} - \mathbf{A_4}:\tilde{\mathbf{L}}]\right\} \tag{2-45}$$

$$\tilde{\mathbf{L}} = \frac{\mathbf{L}^{\mathrm{T}}\cdot\mathbf{L}}{\mathbf{L}^{\mathrm{T}}:\mathbf{L}}, \tag{2-46}$$

where C_I and C_M are the phenomenological parameters which represent fiber-fiber and fiber-matrix interaction, respectively. $\tilde{\mathbf{L}}$ is a second-order symmetric tensor and $\mathbf{L}$ is the velocity gradient tensor. For a detailed mathematical derivation, interested readers are referred to Tseng et al. [94]. However, $\tilde{\mathbf{L}}$ is non-objective in the evolution equation. Additionally, the term $\mathbf{L}^{\mathrm{T}}:\mathbf{L}$ might lead to singularity during the simulation. The iARD term can be linearly added to the standard FT, SRF and a retarding principal rate (RPR) model [95]. The modeling efforts including the anisotropic nature of the suspensions has shown improvement in the out of plane fiber orientation prediction [40, 94]. However, the anisotropic models have not been applied to flexible fiber systems yet, therefore comments of the accuracy of such modeling efforts cannot be made.

2.3.1.6 Semi-flexible Model

Long fibers might deform and bend during complex flow. It is necessary to modify fiber orientation models to account for these effects on fiber orientation kinetics [96]. A semi-flexible (bead-rod) orientation model proposed by Strautins et al. [15] aims to include the effects of bending of fibers on the orientation evoluiton. The flexible fiber was commonly characterized as two vectors, **p** and **q**, connected by a ball and socket joint with an internal resistivity to bending as shown in Figure 2-3. A new tensor, **r**, defined as the second moment of the end-to-end vector, is used to represent the orientation state of flexible fibers:

$$\mathbf{r} = \iint (\mathbf{p} - \mathbf{q})\,(\mathbf{p} - \mathbf{q})\psi(\mathbf{p}, \mathbf{q}, t)d\mathbf{p}d\mathbf{q}. \tag{2-47}$$

The notation of semi-flexible orientation equations are similar to that of rigid fiber models. However, two vectors are included in the semi-flexible model, as a result three moments are need and are defined as:

$$\mathbf{A} = \iint \mathbf{pp}\psi(\mathbf{p}, \mathbf{q}, t)d\mathbf{p}d\mathbf{q} \tag{2-48}$$

$$\mathbf{B} = \iint \mathbf{pq}\psi(\mathbf{p}, \mathbf{q}, t)d\mathbf{p}d\mathbf{q} \tag{2-49}$$

$$\mathbf{C} = \iint \mathbf{p}\psi(\mathbf{p}, \mathbf{q}, t)d\mathbf{p}d\mathbf{q}. \tag{2-50}$$

The **B** tensor is a mixed second moment of the orientation distribution function, where the trace of **B** describes the extent of fiber bending. In the limit where the slightly bent fiber returns to a straightened state, the mixed second moment **B** equals $-\mathbf{A}$ and the first moment tensor **C** goes to zero. The end-to-end tensor, **r**, defined in Eq. (2-47) is then normalized to obtain a tensor **R** in terms of **A** and **B** [97]:

$$\mathbf{R} = \frac{\mathbf{r}}{\mathrm{tr}(\mathbf{r})} = \frac{\mathbf{A} - \mathbf{B}}{1 - \mathrm{tr}(\mathbf{B})}. \tag{2-51}$$

This second moment of average orientation is normalized to make sure the trace equaling unity.

This semi-flexible model was originally developed only for dilute solution, which have been modified by Ortman et al.[97] by adding the isotropic rotary diffusion term given in Eqs. (2-52) to (2-55):

$$\frac{D\mathbf{A}}{Dt} = \alpha\Bigg(\mathbf{W}\cdot\mathbf{A} - \mathbf{A}\cdot\mathbf{W} + \mathbf{D}\cdot\mathbf{A} + \mathbf{A}\cdot\mathbf{D} - 2\mathbf{D}:\mathbf{A}_4 - 2C_I\dot{\gamma}(3\mathbf{A} - \mathbf{I}) + \frac{l_B}{2}(\mathbf{Cm} + \mathbf{mC} - 2(\mathbf{m}\cdot\mathbf{C})\mathbf{A}) - 2k\big(\mathbf{B} - \mathbf{A}\mathrm{tr}(\mathbf{B})\big)\Bigg) \tag{2-52}$$

$$\frac{\mathrm{D}\mathbf{B}}{\mathrm{Dt}} = \alpha\Bigg(\mathbf{W}\cdot\mathbf{B} - \mathbf{B}\cdot\mathbf{W} + \mathbf{D}\cdot\mathbf{B} + \mathbf{B}\cdot\mathbf{D} - 2(\mathbf{D}:\mathbf{A})\mathbf{B} - 4\mathrm{C_I}\dot{\gamma} + \frac{l_\mathrm{B}}{2}(\mathbf{Cm} + \mathbf{mC} - 2(\mathbf{m}\cdot\mathbf{C})\mathbf{B}) - 2k\big(\mathbf{A} - \mathbf{B}\mathrm{tr}(\mathbf{B})\big)\Bigg) \tag{2-53}$$

$$\frac{\mathrm{D}\mathbf{C}}{\mathrm{Dt}} = \alpha\Bigg(\nabla\mathbf{v}^\mathrm{t}\cdot\mathbf{C} - (\mathbf{A}:\nabla\mathbf{v}^\mathrm{t})\mathbf{C} - 2\mathrm{C_I}\dot{\gamma}\mathbf{C} + \frac{l_\mathrm{B}}{2}\big(\mathbf{m} - \mathbf{C}(\mathbf{m}\cdot\mathbf{C})\big) - \mathrm{k}\mathbf{C}\big(1 - \mathrm{tr}(\mathbf{B})\big)\Bigg) \tag{2-54}$$

$$\mathbf{m} = \sum_{i=1}^{3}\sum_{j=1}^{3}\sum_{k=1}^{3}\frac{\partial^2 v_i}{\partial x_j \partial x_k}A_{\mathrm{jk}}\boldsymbol{\delta}_i \tag{2-55}$$

$$k = \frac{\sum n_i k_i}{\sum n_i} \tag{2-56}$$

$$k_i = \frac{E_f}{8\eta_m}\left(\frac{d}{l_i}\right)^3 \tag{2-57}$$

where l_B is equal to $l_i/2$ (half of fiber length), and k_i is the intrinsic resistance of fiber toward bending which is given by Eq. (2-57) for a fiber with length l_i. The expression for k_i was obtained from the bending analysis of a supported beam with a load in the center (Figure 2-11) [97]. In the application for a population of fibers, it is necessary to estimate an average k by Eq. (2-56) [98] where n_i is the number of fibers has a flexibility parameter of k_i. Another way to calculate the averaged k is to directly input the averaged fiber length into Eq. (2-57) [98]. Strautins and Latz [15] developed the smei-flexible model by assuming the fibers are immersed in a non-uniform flow, and numerically the twice differentiable velocity filed contributed to fiber bending. The melt flow induced fiber bending is taken into account through the **m** vector. A limitation of this model is that in simple shear flow the value of **m** equals zero, and the bending predicted is only due to the fiber fiber interaction term. The slip parameter α has also been incorporated to slow down the orientation kinetics, but violates material objectivity. Additionally, except for the $\mathbf{A}_4$ term, the semi-flexible model is developed by using the quadratic closure approximation [96].

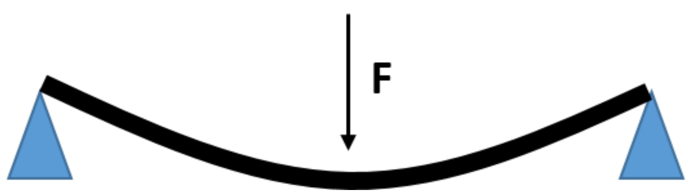

Figure 2-11: Skematic representation of a supported beam with a point force acting on the center.

1.1.1.1 Closure Approximation

The evolution equations for any second order moments in the orientation model always contain the next higher even-order moment [61]. A closure approximation is necessary to obtain higher order tensor in terms from the lower order tensors. The development of closure approximation for the fourth order orientation tensor $\mathbf{A_4}$ has attracted significant attention, the accuracy of which significantly influence the accuracy of the orientation predictions [65, 73].

According to Advani[99], there are several criteria for constructing closure approximations:

(i) The approximation of higher order orientation tenor should be constructed from the lower order orientation tensors.

(ii) The approximation must satisfy normalization conditions ($\sum_k A_{ijkk} = A_{ij}$).

(iii) The approximation should maintain the symmetries of the orientation tensors ($A_{ijkl} = A_{jikl} = A_{kijl} = A_{lijk} = A_{klij}$, etc.).

If different closure approximations satisfy all of these requirements, then they must be evaluated by their accuracy.

The first closure approximation developed was the linear method by Hand et al. [93] as shown in Eq. (2-58):

$$A_{ijkl} \approx -\frac{1}{35}\left(\delta_{ij}\delta_{kl} + \delta_{ik}\delta_{jl} + \delta_{il}\delta_{jk}\right) + \frac{1}{7}(A_{ij}\delta_{kl} + A_{ik}\,\delta_{jl} + A_{il}\delta_{jk} + A_{kl}\delta_{ij} + A_{jl}\delta_{ik} + A_{jk}\delta_{il}) \qquad \textit{(2-58)}$$

This method is to use all of the products of $\mathbf{A}$ and $\boldsymbol{\delta}$ (unit tensor) to calculate the 15 independent terms of $\mathbf{A_4}$. The linearly closure is exact for a completely random distribution of fiber orientation and maintains the symmetry and normalization requirements for $\mathbf{A_4}$. However, Advani and Tucker [65] have demonstrated this approximation showing non-physical instabilities.

A second way to form a closure approximation is to directly multiply the lower-order tensors and is known as the quadratic closure approximation [100, 101] shown in Eq. (2-59):

$$A_{ijkl} \approx A_{ij}A_{kl}. \tag{2-59}$$

The quadratic closure approximations are exact for perfect uniaxial alignment of the fibers, but gives poor results for random fibers and it does not possess the full symmetries of $\mathbf{A_4}$ ($A_{ijkl} \neq A_{ikjl}$) [61].

In order to improve the accuracy over the entire range of orientation, Advani and Tucker [61] mixed the quadratic and linear closure forms according to a scalar measure of 3D orientation, $f = \frac{3}{2}\sum A_{ij}A_{ji} - \frac{1}{2}$ or $f = 1 - 27\det(\mathbf{A})$ [73]. When fibers randomly oriented, the value of f is equal to zero. While perfectly aligned fibers, has a f with value of 1. The corresponding hybrid closure approximation can be is shown in:

$$A_{ijkl} \approx (1-f)A_{ijkl(\text{linear})} + fA_{ijkl(\text{quadratic})}. \tag{2-60}$$

Hybrid closure is useful over a larger range of orientations and it does not show any non-physical oscillatory behavior, but the results are still not very accurate and do not possess the full symmetries of $\mathbf{A_4}$ [102].

Cintra and Tucker [103] proposed a group of orthotropic fitted (ORF) closure approximations in terms of polynomial expansions of the eigenvalues of the 2nd order tensor. The type of approximation makes sure that the principal axes of the approximated 4th order orientation tensor match the principal axes of the second order tensor [104]. Parameters involved in the ORL and ORF approximations are determined by fitting the orientation data from solving the probability distribution function to experimental data [103]. This family of closures has improved orientation predictions. However, ORF was found to cause non-physical oscillations for orientation simulations in simple shear flow when $C_I < 0.001$. Cintra and Tucker came up with ORL by introducing orientation data for $C_I = 0.001$ instead of $C_I = 0.01$. Unfortunately, ORL had the same non-Physical oscillation simulating fiber orientation in a radial diverging flow for $C_I = 0.001$ [104]. To solve the oscillation issues, Chung and Kwon [104] selected two more flow types to be included in the parameters fitting and proposed two new models known as the ORW and ORW3 approximation closures. The method ORW employed 2nd order polynomial expansion of the two largest eigenvalues of **A**, while ORW3 employed 3rd order polynomial expansions.

Verleye and Dupret [105, 106] have proposed a "natural" closure (NAT) approximation method. Unknown coefficients in this method are determined by exact solutions of the probability distribution function setting C_I to be 0. The accuracy of NAT is acceptable, but has the issue of yielding singularities [102, 107].

to address the singularity issue and improve the computational efficiency, Chuang and Kwon proposed the invariant-based optimal fitting (IBOF) closure approximation which is more computational efficient over the eigenvalue-based closure approximations [102]. The expressions for IBOF is given by:

$$\begin{aligned} A_{ijkl} \approx\ & \beta_1 S(\delta_{ij}\delta_{kl}) + \beta_2 S(\delta_{ij}A_{kl}) + \beta_3 S(A_{ij}A_{kl}) \\ & + \beta_4 S(\delta_{ij}A_{km}A_{ml}) + \beta_5 S(A_{ij}A_{km}A_{ml}) \\ & + \beta_6 S(A_{im}A_{mj}A_{kn}A_{nl}), \end{aligned} \tag{2-61}$$

where $\beta_1 - \beta_6$ are unknown coefficients and S is the operator indicating the symmetric part given as:

$$S(T_{ijkl}) \approx \frac{1}{24}\left(T_{ijkl} + T_{jikl} + T_{jkli} + \cdots 24 \text{ terms}\right). \tag{2-62}$$

The choice of β_3, β_4, and β_6 as independent coefficients is recommended for IBOF. And the remaining β_i's are expressed in terms of β_3, β_4, and β_6 and the invariants. The IBOF can be considered a hybrid of the natural and orthotropic closures, and the accuracy of IBOF is comparable to that of eigenvalue-based optimal fitting closure approximations, but requires less computational time [73].

2.3.2 Stress Models

The fiber orientation is induced by the flow field. The properties of flow is also influenced by the existence of fibers [108]. Therefore, a stress model is necessary to couple fiber orientation with flow field. The main interest of this review is high aspect ratio fibers for which the Brownian motion can be neglected. We henceforth neglect the rotary Brownian motion term for all the stress models reviewed here.

2.3.2.1 Rigid Dilute Suspensions

For axisymmetric particles a general stress tensor equation of a dilute suspension based on the volume averaging is:

$$\boldsymbol{\sigma} = -P\mathbf{I} + 2\eta_m\mathbf{D} + \phi_0 \sum_{1}^{N_T} \boldsymbol{\sigma}^{(\boldsymbol{p})}, \tag{2-63}$$

where $\boldsymbol{\sigma}$ is the total stress tensor, $\boldsymbol{\sigma}^{(p)}$ the particle contributed stress, P the isotropic pressure, ϕ_0 the volume fraction of a single particle, N_T the total number of particles and η_m the viscosity of the matrix. The sum is carried out over all particles.

According to Ericksen [62], the stress tensor of a Transversely Isotropic Fluid (TIF) is given as follow:

$$\boldsymbol{\sigma}^{(p)} = 2\mu_0\mathbf{D} + (\mu_1 + \mu_2\mathbf{D}:\mathbf{pp})\mathbf{pp} + 2\mu_3(\mathbf{D}\cdot\mathbf{pp} + \mathbf{pp}\cdot\mathbf{D}), \tag{2-64}$$

here $\mathbf{p}$ is the orientation vector for rigid fiber, and $\{\mu_i\}$ are material constants. If a statistically significant population of particles is contained in a fluid element, the sum in Eq. (2-63) can be removed by using $\phi_0 \sum \boldsymbol{\sigma}^{(\boldsymbol{p})} = \phi_v \langle \boldsymbol{\sigma}^{(TIF)} \rangle$, where ϕ_v is volume fraction of particles and $\langle \cdots \rangle$ denotes orientation averaging. The most general form of the total stress for a dilute fiber suspension is then given by:

$$\boldsymbol{\sigma} = -P\mathbf{I} + 2\eta_m\mathbf{D} + \phi_v[2\mu_0\mathbf{D} + \mu_1\mathbf{A} + \mu_2\mathbf{D}:\mathbf{A_4} + 2\mu_3(\mathbf{D}\cdot\mathbf{A} + \mathbf{A}\cdot\mathbf{D})]. \tag{2-65}$$

Different stress model for a dilute suspension may have different expressions for the material coefficients in Eq. (2-65). Additionally, it has been shown that Eq. (2-65) can also describe the flow behavior for concentrated suspensions [109].

By comparing the stress obtained from the ellipsoid theory [110, 111] with the TIF model, Lipscomb et al. [112] have obtained the values/expressions for $\{\mu_i\}$ for long aspect ratio particle ($a_r \to \infty$):

$$\mu_0 = 2\eta_m \tag{2-66}$$

$$\mu_1 = \mu_3 = 0 \tag{2-67}$$

$$\mu_2 = \eta_m a_r^2/\ln(a_r). \tag{2-68}$$

Hinch and Leal [113] derived the same μ_0 and slightly different μ_2 and μ_3 given by:

$$\mu_2 = \eta_m a_r^2/[\ln(2a_r) - \frac{3}{2}] \tag{2-69}$$

$$\mu_3 = \eta_m[6\ln(2a_r) - 11]/a_r^2. \tag{2-70}$$

Based on the slender-body theory of Batchelor [114], Evans [115, 116] evaluated the only non-zero material parameter as:

$$\mu_2 = \eta_m 8a_r^2 / \, 6\ln(a_r). \tag{2-71}$$

Gernerally, most slender-body theories give $\mu_0 = 0$.

2.3.2.2 Rigid Semi-Concentrated Suspensions

For non-dilute suspensions, the stress equation based on slender body theory has a general form:

$$\boldsymbol{\sigma} = -P\mathbf{I} + 2\eta_m\mathbf{D} + 2\eta_m N_p \mathbf{A_4}\colon\mathbf{D}, \tag{2-72}$$

where N_p is a non-dimensional parameter which takes into account of fibers' contribution in the total stress[108].

Batchelor [114] has used extensional flow to determine material parameters for semi-dilute regime. The effect on one particle of its neighbors can be approximated by an equivalent cylindrical boundary around the particle. This "hydrodynamic screening" theory leads to an expression of N_p in Eq. (2-72) for close parallel particles subjected to pure straining motion [117]:

$$N_p = \frac{\pi n L^3}{6\ln(\pi/\phi_v)}, \tag{2-73}$$

where *n* is the density of fibers and all the fibers are assumed to have the same length L.

Dinh and Armstrong [24] extended Batchelor's [118] theory to arbitrary flows with arbitrary fiber orientation states and developed a new stress model. Their model does not include any mechanical contacts between fibers. The key step is to replace the multi-particle problem with a single–particle by using Batchelor's [118] cell model. The summation of each particle's contribution is replaced by the product of number density and the orientation averaging. Eventually, by comparing the derived elongational viscosity with Batchelor's [118] result, Dinh and Armstrong [24] proposed an expression for N_p given by:

$$N_p = \frac{\pi n L^3}{12\ln(2h/d)}, \tag{2-74}$$

here h is the average distance between fibers which is given by $h = (nL^2)^{-1}$ for random orientated fibers and $h = (nL)^{-1/2}$ for completely aligned fibers. This model over-predicted the flow viscosity compared to the theory for randomly oriented suspension [73]. Chung and Kwon [119] assumed h is proportional to a scalar f defined by :

$$f = 1 - 27\det[\mathbf{A}]. \tag{2-75}$$

For random orientation the value of f is zero ,while f is 1 for perfectly aligned orientation. Using this parameter f Chung and Kwon's [119] defined h as:

$$\begin{aligned} h &= (1-f)h_{random} + f h_{aligned} \quad \left(\tfrac{1}{L^3} < n \le \tfrac{1}{dL^2}\right) \\ h &= h_{aligned} \quad \left(\tfrac{1}{dL^2} \le n < \tfrac{1}{d^2L}\right). \end{aligned} \tag{2-76}$$

Shaqfeh and Fredrickson [120] have verified Bathcelor's [118] theory by utilizing a semi-rigorous "multiple-scattering" theory accounting for multi-particle hydrodynamic interactions and have proposed a slightly improved formula for N_p:

$$N_p = \frac{\pi L^3 n}{6[\ln(1/\phi_v) + \ln(\ln(1/\phi_v)) + \mathrm{A}]} \tag{2-77}$$

where A = -0.66 for suspensions in which the rods are isotropically oriented and A = 0.16 when they are aligned in a single direction. Bibbo [121] experimentally observed that Shaqfeh-Fredrickson equation considerably under-predicted the flow viscosity of their studied concentrated fiber suspensions compared to experimental results.

The slender body theory based models described above assume that the fibers have no thickness. To account for the finite fiber thickness, the parameter N_p can multiplied by a correction factor $f(\epsilon)$ [122] described by:

$$f(\epsilon) = \frac{1 + 0.64\epsilon}{1 - 1.50\epsilon} + 1.659\epsilon^2 \tag{2-78}$$

where ϵ is $1/\ln(2a_r)$. As a_r approaches to infinity, the value ϵ approaches 0 with $f(\epsilon)$ approaching 1. For example, when $a_r = 100$, the corresponding value of $f(\epsilon)$ would be 1.62. This is value lager than 1 is an substantial correction for the fiber thickness. However this modification predicted zero extra-stress for perfect aligned fiber suspension whisch is non-physical.

Another deficiency of the above reviewed semi-concentration models is that they only account for the long-range hydrodynamic interaction between fibers. Therefore, these semi-dilute models significantly under-predicted the overall stress than the experimental measurement for moderately concentrated fiber suspensions [123]. Djalili-Moghaddam and Toll [123] developed a model which combined short range hydrodynamic lubricant friction with the Shaqfeh-Fredrickson's [120] model accounting for long range hydrodynamic interaction. It was seen that this model predicted considerably higher stress response than that predicted by the Shaqfeh-Fredrickson theory. However, this model was based on convective discretization (often called direct simulation), and an extra adjustable parameter, *k*, was introduced [123]. Most recently, Ferec et al. [124] proposed a new extra-stress model for the semi-concentrated fiber suspension which was an extension of the Dinh-Armstrong [24] model. Linear lubrication forces was taken into account in this model to include the fiber-fiber interactions and this model performed well in predicting overall stress in simple shear for a glass fiber suspension with newtonian polybutene matrix. However, this model has extra equation and parameter to take into account of the fiber-fiber interactions.

2.3.2.3 Rigid Concentrated Suspensions

Phan-Thien et al. [125] have proposed an analogous phenomenological constitutive equation to describe the total stress given by:

$$\boldsymbol{\sigma} = -P\mathbf{I} + 2\eta_m\mathbf{D} + 2\eta_m\phi_v N_p(\phi_v, a_r)\mathbf{A_4}:\mathbf{D}, \tag{2-79}$$

where N_p accounts for the contribution from the fibers which takes the form of:

$$N_p = \frac{a_r^2(2-\phi_v/A_v)}{4(\ln(2a_r)-1.5)(1-\phi_v/A_v)^2}. \tag{2-80}$$

Here ϕ_v is the volume fraction of fibers, a_r the fiber aspect ratio and A_v is the upper boundary for the fiber volume fraction in the suspension. A linear regression through Kitano's [126] viscosity data shows that A_v can be approximated by the linear relation:

$$A_v = 0.53 - 0.013a_r, \qquad 5 < a_r < 30. \tag{2-81}$$

The usage of this model is limited by the limited range of aspect ratio and the corresponding maximum volume fraction. Besides, the parameter A_v needs to be determined by experiment.

Based on the early work of Ericksen [62] and Lipscomb et al. [112], another phenomenological model for the stress tensor in a concentrated suspension is given by:

$$\boldsymbol{\sigma} = -P\mathbf{I} + 2\eta_m(\mathbf{D} + c_1\phi_v\mathbf{D}) + N\mathbf{A_4}:\mathbf{D}. \tag{2-82}$$

Similar to μ_0 in Eq. (2-65), the value of c_1 attempts to quantify the stress enhancement due to the existence of fibers in the system. Eberle et al. [127] has chosen to use N as a fitting parameter and the value of $c_1$is often fitted as well. With different initial fiber orieantion states, Ortman et al. [128] has reported varying degrees of success by using this fitting technique.

2.3.2.4 Long Fiber Suspension

Direct simulations have been used to study the viscosity of suspensions containing flexible or semi-flexible fibers [10, 129]. Joung [129] have included a small amount of bending and torsion for the flexible fibers in simulation, as a result the predicted viscosity was notably larger than that without including these bending and torsion effects for rigid fiber suspension. Goto et al. [130] experimentally observed similar trends.

Keshtar et al. [131] investigated this topic by both experiment and simulation and reported that even in dilute range, the viscous and elastic properties increased significantly with fiber flexibility. Fiber orientation evolution was also faster for the more rigid fibers. Their simulation was performed using the general equation for non-equilibrium reversible-irreversible coupling (GENERIC).

The prediction of stress tensor of concentrated long fiber suspensions have seldom been reported. Most recently, Shaqfeh and Fredrickson's [120] model was used by cieslinski et al. [6] to predict the growth of shear stress of a glass fibers suspension during the startup of simple shear flow. Measured second and fourth order fiber orientation data were directly used in the stress prediction in order to avoid any error from the closure approximations. However, the experimentally observed stress overshoot was not predicted by Shaqfeh and Fredrickson's [120] model which also under-predicted the steady state value for 20 wt% to 40 wt% glass fiber suspensions. The authors [6] proposed that to extend the semi-concentrated theory to the concentrated fiber suspension, the direct fiber-fiber interactions or other interactions need to be included.

Ortman et al. [97] have included the fiber semi-flexibility in their proposed stress tensor which showed some success in modeling stress growth of concentrated semi-flexible fiber suspensions during the startup of simple shear flow. The stress tensor is presented as:

$$\boldsymbol{\sigma}_{flex} = -P\mathbf{I} + 2\eta_m(\mathbf{D} + f_1\phi_v\mathbf{D} + f_2\mathbf{A_4}:\mathbf{D}) + \eta_m k\,\frac{3\phi_v a_r}{2}(\mathbf{B} - \mathbf{A}\mathrm{tr}(\mathbf{B})) \tag{2-83}$$

where l_b is the half of the average fiber length. Ortman et al. [97] also provided quantitative expressions for the material parameters f_1 and f_2:

$$f_i = \begin{cases} \frac{c_1}{\dot{\gamma}_{min}^b} & \text{for } \dot{\gamma} \leq \dot{\gamma}_{min} \\ \frac{c_1}{\dot{\gamma}} & \text{for } \dot{\gamma} > \dot{\gamma}_{min} \end{cases} \tag{2-84}$$

$$f_2 = c_2 I_A II_A III_A \tag{2-85}$$

$$I_A = tr(\boldsymbol{A}) = 1 \tag{2-86}$$

$$II_A = \frac{1}{2}[tr(\boldsymbol{A})^2 - tr(\boldsymbol{AA})] \tag{2-87}$$

$$III_A = \det(\boldsymbol{A}) \tag{2-88}$$

This model relied on fitting transient stress curves to obtain 5 empirical parameters (2 parameters are for the bead-rod orientation model). Additionally, both of f_1 and f_2 fail to recover the value or expression for infinite dilute case [112], and the lack of physical meaning of its parameters is the model's another shortcoming. Modeling for the stress tensor in concentrated long fiber suspensions still remains controversial and no other theory has been presented which accounts for the additional bending that may occur.

1.1.2 Numerical Predictions of fiber orientation

To generate thermoplastic parts reinforced with fibers, the robust and fast injection molding process is commonly used in industry. Two simple geometries extensively studied are the center-gated disk (CGD) and end-gated plaque (EGP) as shown in Figure 2-12 (a) and (b), respectively. The CGD was used as a benchmark test geometry by a number of researchers because of the existence of extensional flow, shear flow and the mixture of both during the mold filling process, besides the geometry is relatively simple to carry out numerical simulation [85, 132, 133]. Modeling and experimental orientation in a CGD is traditionally performed along a plane of constant θ because it is axisymmetric in the θ direction. While the second common geometry, the EGP, is not axisymmetric, giving it a full 3-D velocity field, where orientation varies with the thickness, length and width of the plaque. In most studies, the orientation along the center plane has been examined [84, 85].

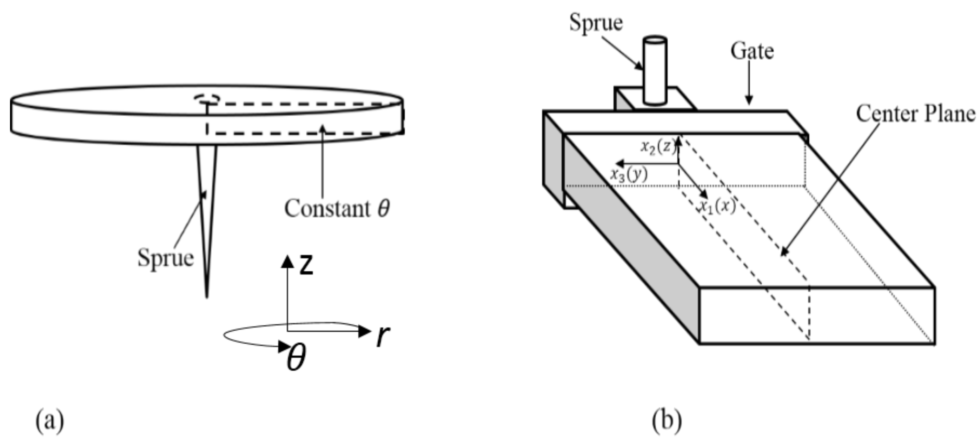

Figure 2-12: Schematic geometries of (a) center-gated disk and (b) end-gated plaque.

The filling stage during injection molding is of great importance on fiber orientation [68]. Features of flow during injection molding filling affecting fiber orientation include:

(i) strong elongational flows in the entry region;

(ii) shearing flow near the mold wall in the lubrication region;

(iii) the fountain flow at the advancing free surface.

An accurate prediction of the flow pattern with important features during mold filling process is the prerequisite for an accurate prediction of fiber orientation during injection molding. For this reason, the numerical simulation of fiber orientation is reviewed from the aspect of the effect of the flow pattern on fiber orientation. First the full system of balance equations are reviewed in §1.1.2.1. Next, a description of simulating systems by either a Hele-Shaw method or full simulation method is presented in §1.1.2.2. Finally, a review of fiber orientation simulations using the the decoupled and coupled method is given in §1.1.2.3.

1.1.2.1 Balance Equations for polymer flow

The solution to any flow problem begins with the equations of continuity and the equation of motion. For incompressible flow, the continuity and motion equations are given by Eq. (2-89) and Eq. (2-90):

$$\boldsymbol{\nabla} \cdot \mathbf{v} = 0 \tag{2-89}$$

$$\rho \frac{\partial \mathbf{v}}{\partial t} + \rho \mathbf{v} \cdot \boldsymbol{\nabla} \mathbf{v} - \boldsymbol{\nabla} \cdot \boldsymbol{\sigma} = \mathbf{0}, \tag{2-90}$$

where $\mathbf{v}$ is the velocity vector, ρ the fluid density, and $\boldsymbol{\sigma}$ the total (Cauchy) stress. Additionally, if thermal effects are included, then the energy equation must also be solved:

$$\rho c_p \frac{DT}{Dt} = \boldsymbol{\sigma} : \mathbf{D} + k \nabla^2 T, \tag{2-91}$$

where c_p is the heat capacity, T is the temperature and k is the thermal conductivity.

To further include the effects of fibers, the solution of the flow needs to be coupled with fiber orientation and extra stress equations [108]. However, the numerical strategy used in practical simulation of fiber orientations normally apllied several simplifications including: isothermal conditions [134], Hele-Shaw approximation [132] and decoupled method [108]. The isothermal approximation is justified when the filling phase is rapidly enough to experience only slight change in the melt temperature [135]. In the following two sub-sections more detailed discussions about the Hele-Shaw and decoupled simplification will be given.

1.1.2.2 Hele-Shaw Approximation vs. Full Simulation Effects

Many simulations of fiber orientation used the Hele-Shaw flow approximation to simplify the calculations and reduce the computational demands [136]. Predictions based on this approximation show reasonable agreement with experimental data when the effects of fountain flow can be neglected [72, 105, 107, 119, 137, 138]. Applying the lubrication approximation, the simplified Hele-Shaw flow is similar to pressure driven flow between parallel plates [139]. Important assumptions for the filling model of the Hele-Shaw approximation are:

- the cavity is very thin, h/L << 1, where L is the mold length along flow direction;
- fluid is moving at a low Reynolds number;
- the flow details near the gate and in the fountain flow region are ignored.

In the application Hele-Shaw flow in orientation simulation, a velociy profile and initial fiber orientation at the inlet need to be specified (Figure 2-13). The use of inaccurate velocity and fiber orientation profiles at the inlet, might result in inaccurate fiber orientation predictions compared to experimental data[73]. The effects of various inlet fiber orientation state on predictions of orientation evolution will be discussed.

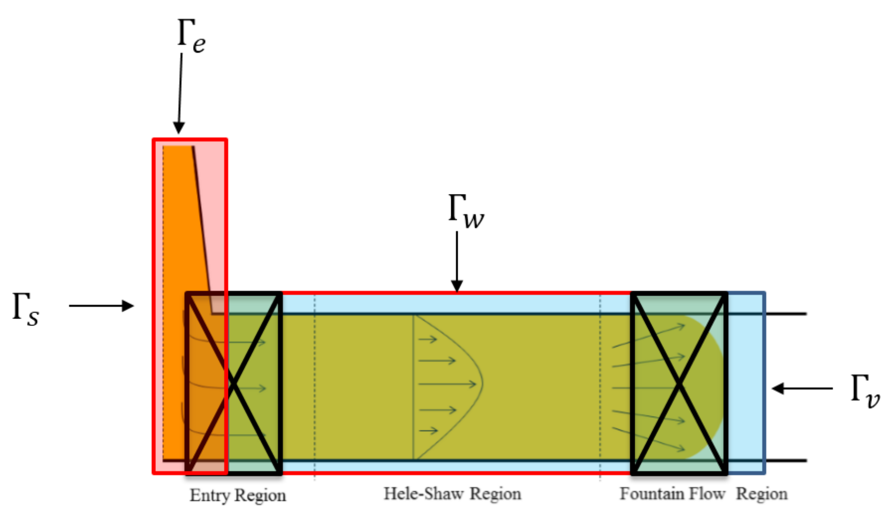

Figure 2-13: Schematic illustration of Hele-Shaw approximation.

Ranganathan et al. [140] used two different inlet orientation conditions (one is random, while the other is perfectly aligned) for orientation simulation with semi-concentrated fiber suspensions in an axisymmetric diverging radial flow. Significant difference between the orientation predictions using these two different inlet conditions was observed at a multiple regions as shown in Figure 2-14.

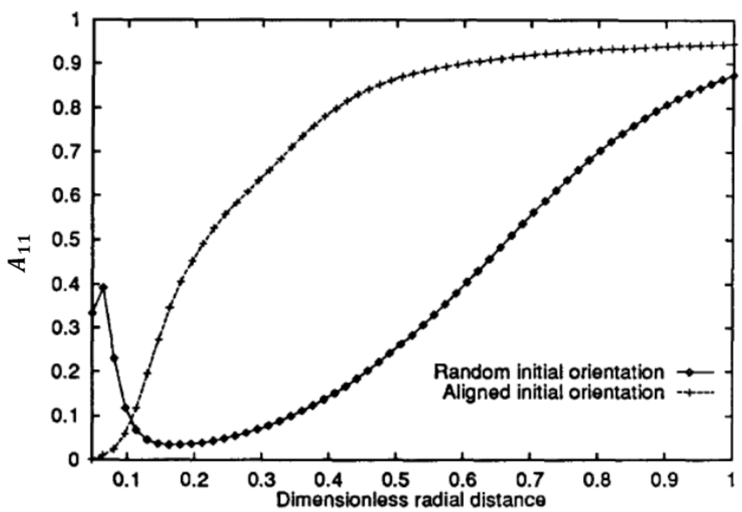

Figure 2-14: Predicted A_{11} component along the radial distance from random initial orientation and aligned initial orientation [140].

VerWeyst and Tucker [141] included the sprue in their simulations for a center-gated disk. It was found that the predicted orientation were asymmetry along the thickness direction of the disk, showing the effects of the sprue which make the inlet velocity profile deviate significantly from the assumed parabolic profile when sprue is excluded. This method generated a more realistic orientation state at the inner radius of the disk than the customarily assumed random orientation.

Chung and Kwon [133] also observed the same asymmetry in orientation through sample thickness when the sprue was included in the simulation of a center gated disk.

They found that once combined with the coupled simulation method, the entrance effects persist even near the shell layers. Chuang and Kwon [133] further observed that the center-gated disk was affected by the initial orientation more than the film-gated strip. Based on Tucker's [108] order of magnitude analysis and Altan's [142] steady state coupled simulation, Chung and Kwon [133] proposed that the duration of entrance effect increases with slenderness of gap, ε, was defined as the ratio of the typical mold thickness to the representative planar dimension. The film-gated strip has a smaller value of ε, and thus less influenced by the inlet conditions. These conclusions are based on several assumptions like isothermal condition and small out of plane orientation.

Velez-Garcia et al. [86] conducted fiber orientation prediction using a decoupled approach for short glass fiber in a center-gated disk geometry without including the sprue region. A slip parameter reflecting the slower the fiber orientation evolution kinetics was directly multiplied to the right hand side of the Folgar-Tucker model. In the simulation, both random orientation and experimentally measured values are used as inlet conditions. Even without the sprue, the inlet conditions had been washed out quickly without strain reduction factor. Predictions using the strain reduction factor with the experimentally determined orientation matched well with experimental data at the core region and near the front.

The exclusion of fountain flow in Hele-Shaw approximation may add inaccuracies to the resulted fiber orientation predictions [132]. Fountain flow, an intrinsic feature during mold filling, was introduced by Rose[143] used to describe the complex gap-wise flow profile immediately behind melt/air interface [68]. An advancing front between two parallel plates is shown in Figure 2-15. The reason for the occurring of fountain flow during injection molding is that the melt/air interface moves with the average velocity of the filling fluid. However, this average velocity is faster than that near the wall, while less than the velocity near the center resulting a deceleration of the fluid around the mid-plane as it approaches the slow moving front. As a result of incompressibility, the fluid elements acquires a transverse velocity, in the lagrangian reference frame, spilling outward towards the wall and developing a fountain-like profile.

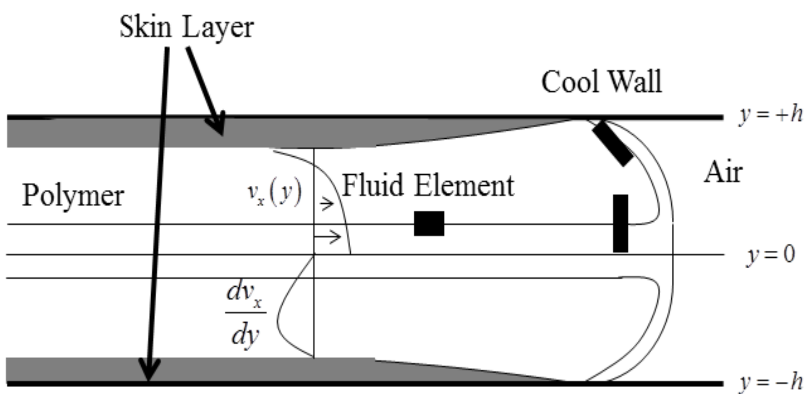

Figure 2-15: Flow patterns near the advancing front for flow between two parallel plates in a moving reference frame [144]. The fluid element reaches a stagnation point where the fluid is stretched and moved toward the outside wall.

Fountain flow has a critical effect on fiber orientation especially for those fibers driven by fountain flow and then immediately got frozen by the cold polymer near the wall. Bay et al. [79] has shown that complex flow field induced by the fountain-flow region changed the orientation of fibers passing through it accordingly and finally pushed the fibers toward the walls (Figure 2-16) thereby resulting a feature of wide core layers of orientation distribution especially near the the end of fill [85, 132, 133, 145]. In Figure 2-17 is shown markedly different predictions for fiber orientation through the gap thickness near the flow front of a center-gated disk, and simulation including fountain flow effects shows better agreement with the experimental results thus improved the predictions compared to Hele-Shaw approximation. Moreover, when non-isothermal cooling effect is important, the fibers transferred by the fountain flow from core to the wall, instantly solidifies forming a skin layer with relative lower flow direction orientation compared with the shell region away from the mold walls [86, 89]. The scaled dimensionless parameters Graetz number (Gz) and Brinkman number (Br) are helpful to understand the non-isothermal effects [72, 133]. VerWeyst et al. [81] suggested that a variation in viscosity of four orders of magnitude is sufficient to distinguish between molten and "frozen" regions. Incorporation of the fountain flow effects and the thermal effects is important to improve the fiber orientation predictions near the walls especially when non-isothermal effect is notable [146].

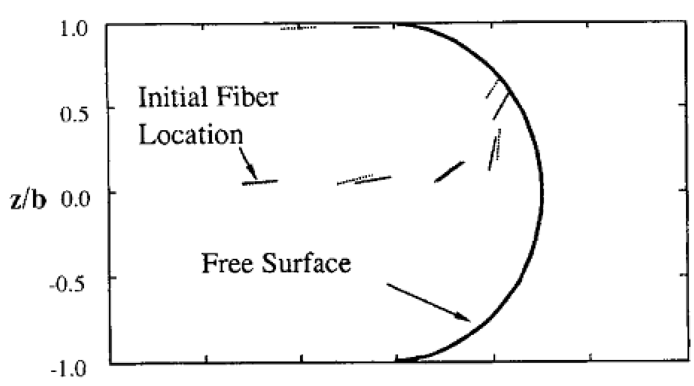

Figure 2-16: Motion of a single fiber in the fountain flow [132]. Solid lines represents the predicted results, while dashed lines are experimental results.

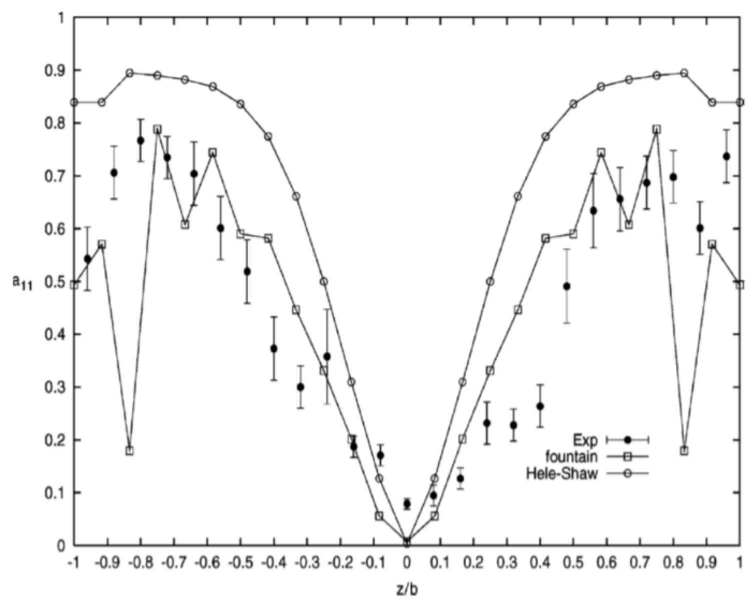

Figure 2-17: Comparison of A_{11} predictions from fountain flow and Hele-Shaw simulations, at r/b = 40.4 [133] through sample thickness positions (z/b).

1.1.2.3 Decoupled vs. Coupled Simulation

The decoupled method is widely used in the fiber orientation simulation in molded parts, where the fluid motion is computed without knowledge of the fiber orientation. While such procedures failed to include the complete physical features of the flow, they are widely used and can provide acceptable fiber orientation predictions when compared to experiments [99]. The validity of using decoupled method is based on the fact that, if the fiber orientation is effectively in-plane, then the existence of fibers has little influence on the gap-wise velocity profile.

A stress equation which includes the contribution due to the presence of fibers are commonly used in the coupled approach which make the orientation and flow profile to be mutually dependent on each other [108]. Here the influence of fiber orientation on flow pattern will be discussed first. Take a pressure-driven flow between parallel plates for example, fibers near the wall tended to orient faster than those in the center plane resulting various fiber orientation state from top to bottom. As a result the stress response of the suspension through the gap varied accordingly to the orientation state which in turn resulted in a relatively blunt velocity profile compared to the absence of fibers [78]. Another case is the radial diverging flow (center gated disk), with largest stretch rates near the mid-plane and zero stretch rate at the wall. According to Tucker [108], stretching flows produce flatter orientation distributions than simple shear flows. This may lead to greater out of plane orientation near the wall and flatter orientation near the mid-plane resulting in a relatively sharper velocity profile through the thickness (bell-shape).

Tucker [108] has used a non-dimensional parameter, $N_p\delta^2$, to identify four flow regimes for fiber suspensions in narrow planar gaps (Figure 2-18) in which the rotary diffusion term was neglected and fibers were assumed to lay nearly parallel to the surface of the gap. In regime I shown in Figure 2-18, the presence of fibers had no effect on flow field and the usage of decoupling was valid for this case. Regime II might occur for the case with largest stretch rates near the mid-plane and zero stretch rate at the wall. It is more difficult to anticipate velocity profiles for Regime III. An intuitive speculation is that when the wall region has flatter orientation than that of the mid-plane, flow pattern of Regime III might occur. Additionally, recent numerical calculations for a transversely isotropic fluid in axisymmetric squeeze flow suggest that the velocity profile will be blunter than the parabola of Regime I [147]. According to Tucker [108], a very different flow regime IV which might not be prevalent in the mold cavity for injection molding process, occurs when the material is highly anisotropic and moderately thick ($N_p\varepsilon$ is large), and the fiber orientation distribution is very flat (squeezing flow).

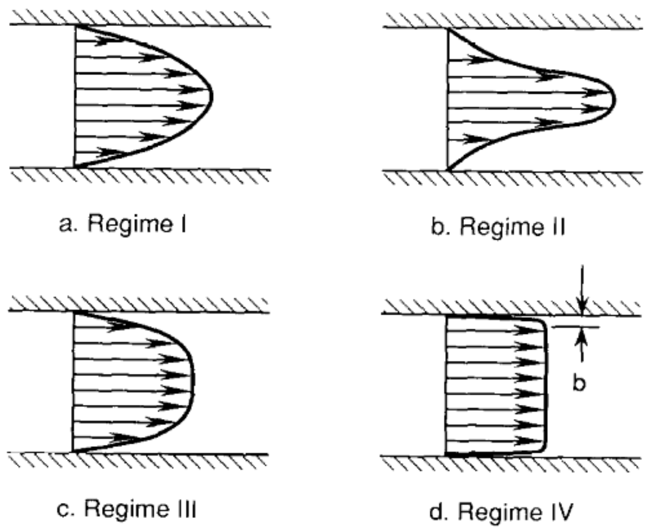

Figure 2-18: General character of the gap-wise velocity profiles for the different flow regimes [108].

Lipscomb et al. [112] conducted coupled simulation of the fiber suspension with long fibers (3.2 mm or 6.4 mm) going through an axisymmetric contraction geometry by incorporating the statistical orientation distribution function into the stress equation. Notably, Jeffery's orientation equation was used, and thus fiber-fiber interactions were neglected. They observed that even a dilute suspension behaved differently from that of the pure matrix , although the shear viscosity of the suspension was constant and close to that of matrix. They further concluded that the reason for this difference was associated with the presence of an extensional flow along the centerline.

Altan et al. [148] used a finite difference method to conduct coupled simulation of a suspension passing a straight channel. The authors specified that both orientation and flow were planar. The Dinh-Armstrong [24] model was used to model the overall stress and Jeffery's orientation equation was used to predict fiber motion. The velocity profile near the inlet was changing towards plug-flow behavior with the increase in N_p value. The fully developed region was shown no influence from the presence of fibers, which was due to the exclusion of the fiber-fiber interactions and in the Din-Armstrong's stress model the slender-body approximation was used.

Ranganathan and Advani [140] conducted a coupled steady state simulation for fiber suspensions in the semi-concentrated and concentrated ranges. Specifically, suspensions with 0.05 or 0.01 fiber volume fraction and a fiber aspect ratio of 50 were studied. Finite difference method was used to simulate a diverging radial flow. Random orientation was prescribed at the inlet boundary. Shaqfeh and Fredrickson's [120] model with a correction factor accounting for finite fiber thickness was used to calculate the rheology of the suspension. The governing equation for the orientation was cast in terms of the fourth-order orientation tensor, which also included the fiber-fiber interaction term. It was seen that the velocity at the center increases from the inlet value, gone through a maximum, and then decreased. This was because the shear viscosity near the wall initially increased and then decreased. The velocity profile in the higher volume-fraction suspension (0.05) was more plug-like (shaper near the inlet but became plug-like from the middle to the end) than the other case. Chuang and Kwon [137] suggested that this was an artifact of their wall boundary condition, in which fibers highly aligned toward the flow direction and thus significantly reduced the stress contribution form the fibers near the wall. Ranganathan and Advani [140] further investigated the effect of the interaction coefficient and reported that when a small C_I was used, the center-line velocity in result was not much different from that of Newtonian solution. Ranganathan and Advani [140] also found that the altered coupled velocity field was seen to have a pronounced effect on the solution of the orientation field.

Verweyst and Tucker [141] performed a coupled steady state simulation for concentrated fiber suspension in a center-gated disk with a sprue. The finite element method as well as isothermal assumption were used in this study. Average aspect ratio for fibers in this work was 20. It was observed that the presence of fiber did influence the flow profile and the predicted orientation. A gap-wise velocity profile slightly more pointed than a parabola was observed, which differed from Rangana and Advani's result [140]. Additionally, in coupled solutions the mid-plane velocity rose more slowly with radius (i.e. more blunt flow close to the gate) and eventually leveled out at a value slightly above the velocity value of Newtonian flow. However, as approaching the end of the disk, the effects coupling turned out to decrease as the orientation results did not show much difference from decoupled solution.

Chung and Kwon [119] also conducted coupled simulations when non-isothermal effects were included for a tension test specimen using Hele-Shaw assumption. The fibers studied had an aspect ratio of 25 and the orientation state at inlet was specified as random. As fiber volume fraction increased from 0.1% to 3.1%, the velocity profile close to the gate was turned out to be more. However, the presence of fibers had no effect on the velocity profile in the narrow bar of the tension test specimen. The fiber orientation state in the narrow region was quite planar with almost zero out of plane component, so the fibers there barely contributed to the overall stress. However, it is worth notice that, the in-plane velocity gradient was set to be zero in the stress equation.

In a continuous work, Chung and Kwon [137] used a similar numerical method and included the stresses resulted from the in-plane velocity gradients. In this study a ttransient simulation was conducted for short fiber suspension with aspect ratio of 20. The orientation at the inlet was obtained from a steady state simulation. Both isothermal and non-isothermal simulations were investigated and compared and the effects of in-plane stretching stress terms on pressure, velocity and fiber orientation fields were studied The results showed that the existence of in-plane stretching terms did altered the velocity at the center layer and near the gate. In addition, the in-plane velocity gradient effect on the fiber orientation were significant near the gate, more notably for a polymer matrix with a non-isothermal effect.

Most recently, Chung and Kwon [133] performed a finite-element method analysis of an axisymmetric non-isothermal flow using the pseudo-concentration method including the fountain flow effects. The Dinh-Armstrong model [24] of stress was used. Random orientation was prescribed at the inlet. It turned out that coupled velocity profile was more flat than the decoupled case especially near the inlet. This trend was different from their previous work [137]. It was also seen that the including of fountain flow enchanted the effect of coupling on orientation. In addition, coupling effect is more notable in the core and transition layers.

Mazahir et al. [89] used a discontinuous Galerkin finite element method to develop a transient simulations of fiber orientation with the Folgar-Tucker model and its slip and reduced strain closure versions. Decoupled and coupled transient simulations with Hele-Shaw approximation were performed using a measured orientation profile at the inlet of the cavity of a center gated disk. A 30 wt% short glass fibre polybutylene-terephthalate (PBT) suspension with average aspect ratio of 28.1 was investigated. The application of coupled simulations wasn't able to improve the agreement between the predictions and the experimental data. It was not necessary to conduct more complicated coupled simulation when de-coupled results were comparable to those using the coupled approach.

In a continued effort, Mazahir et al. [134] studied the fiber orientation of the same fiber suspension at the frontal region of the same center gated disk. Because the molding filling was pretty fast, isothermal assumption was used in the simulation. A pseudo concentration method was applied to include the fountain flow effects at the advancing front. Coupled and decoupled simulations were conducted and the results were compared with experimental orientation values. The value of the dimensionless coupling parameter was obtained either from theory or from rheological experiments. It was seen that the coupled simulation predicted a broader frontal region than that in decoupled simulations. The coupled RSC model with the largest coupling parameter was able to slightly slow down the evolution of orientation in the frontal region. However, the slowdown was not enough to match the even slower evolution observed in experimental data. In the region behind the frontal region, the simulation results of decoupled and coupled method do not show much difference which was contrary to Chung and Kwon's [133] finding. Chung and Kwon investigated a similar system as Mazahir et al [134], but they used a significantly different inlet boundary condition from Mazahir's case. It is hard to make any conclusion at this moment, but it may worth to investigate the influence of inlet boundary condition on the coupling effect.

However, most of coupling simulations only considered short fibers. No study has used a variable length in the stress model to investigate the effect of fiber breakage on fiber orientation. Moreover, only rigid fiber orientation models were used. As fiber length increased, it will have the ability to bend. Recent works were able to show that the semi-flexible fiber model gave improved orientation predictions when compared to rigid model [98, 149].

References

1. J.H. Phelps, Processing-microstructure models for short-and long-fiber thermoplastic composites, ProQuest, 2009.
2. A. Hassan, R. Yahya, A.H. Yahaya, A.R.M. Tahir, P.R. Hornsby, Tensile, Impact and Fiber Length Properties of Injection-Molded Short and Long Glass Fiber-Reinforced Polyamide 6,6 Composites, Journal of Reinforced Plastics and Composites, 23 (2004) 969-986.
3. J.L. Thomason, The influence of fibre length and concentration on the properties of glass fibre reinforced polypropylene: 5. Injection moulded long and short fibre PP, Composites Part A: Applied Science and Manufacturing, 33 (2002) 1641-1652.
4. J.L. Thomason, The influence of fibre length and concentration on the properties of glass fibre reinforced polypropylene. 6. The properties of injection moulded long fibre PP at high fibre content, Composites Part A: Applied Science and Manufacturing, 36 (2005) 995-1003.
5. J.L. Thomason, M.A. Vlug, Influence of fibre length and concentration on the properties of glass fibre-reinforced polypropylene: 4. Impact properties, Composites Part A: Applied Science and Manufacturing, 28 (1997) 277-288.
6. M.J. Cieslinski, P. Wapperom, D.G. Baird, Influence of fiber concentration on the startup of shear flow behavior of long fiber suspensions, Journal of Non-Newtonian Fluid Mechanics.
7. M. Doi, S.F. Edwards, The theory of polymer dynamics, Clarendon Press Oxford, 1986.
8. W.-K. Chin, H.-T. Liu, Y.-D. Lee, Effects of fiber length and orientation distribution on the elastic modulus of short fiber reinforced thermoplastics, Polymer Composites, 9 (1988) 27-35.

9. D.M. Bigg, Effect of compounding on the properties of short fiber reinforced injection moldable thermoplastic composites, Polymer Composites, 6 (1985) 20-28.
10. L.H. Switzer, D.J. Klingenberg, Rheology of sheared flexible fiber suspensions via fiber-level simulations, Journal of Rheology (1978-present), 47 (2003) 759-778.
11. L.H. Switzer, D.J. Klingenberg, Flocculation in simulations of sheared fiber suspensions, International Journal of Multiphase Flow, 30 (2004) 67-87.
12. C.F. Schmid, L.H. Switzer, D.J. Klingenberg, Simulations of fiber flocculation: Effects of fiber properties and interfiber friction, Journal of Rheology (1978-present), 44 (2000) 781-809.
13. B. Hausnerova, N. Honkova, A. Lengalova, T. Kitano, P. Saha, Rheology and fiber degradation during shear flow of carbon-fiber-reinforced polypropylenes, Polymer Science Series A, 48 (2006) 951-960.
14. A. Huq, J. Azaiez, Effects of length distribution on the steady shear viscosity of semiconcentrated polymer-fiber suspensions, Polymer Engineering & Science, 45 (2005) 1357-1368.
15. U. Strautins, A. Latz, Flow-driven orientation dynamics of semiflexible fiber systems, Rheologica Acta, 46 (2007) 1057-1064.
16. A. Kelly, a.W. Tyson, Tensile properties of fibre-reinforced metals: copper/tungsten and copper/molybdenum, Journal of the Mechanics and Physics of Solids, 13 (1965) 329-350.
17. R. Bailey, H. Kraft, A Study of Fibre Attrition in the Processing of Long Fibre Reinforced Thermoplastics, International Polymer Processing, 2 (1987) 94-101.
18. T. Vu-Khanh, J. Denault, P. Habib, A. Low, The effects of injection molding on the mechanical behavior of long-fiber reinforced PBT/PET blends, Composites Science and Technology, 40 (1991) 423-435.
19. S.-Y. Fu, B. Lauke, E. Mäder, C.-Y. Yue, X. Hu, Tensile properties of short-glass-fiber-and short-carbon-fiber-reinforced polypropylene composites, Composites Part A: Applied Science and Manufacturing, 31 (2000) 1117-1125.
20. V.B. Gupta, R.K. Mittal, P.K. Sharma, G. Mennig, J. Wolters, Some studies on glass fiber-reinforced polypropylene. Part I: Reduction in fiber length during processing, Polymer Composites, 10 (1989) 8-15.
21. L. Czarnecki, J.L. White, Shear flow rheological properties, fiber damage, and mastication characteristics of aramid-, glass-, and cellulose-fiber-reinforced polystyrene melts, Journal of Applied Polymer Science, 25 (1980) 1217-1244.
22. J.H. Phelps, A.I. Abd El-Rahman, V. Kunc, C.L. Tucker Iii, A model for fiber length attrition in injection-molded long-fiber composites, Composites Part A: Applied Science and Manufacturing, 51 (2013) 11-21.
23. O.L. Forgacs, S.G. Mason, Particle motions in sheared suspensions: IX. Spin and deformation of threadlike particles, Journal of Colloid Science, 14 (1959) 457-472.
24. S.M. Dinh, R.C. Armstrong, A Rheological Equation of State for Semiconcentrated Fiber Suspensions, Journal of Rheology (1978-present), 28 (1984) 207-227.
25. J.M. Burgers, On the Motion of Small Particles of Elongated Form. Suspended in a Viscous Liquid, Springer, 1995.
26. S.H. Bumm, J.L. White, A.I. Isayev, Glass fiber breakup in corotating twin screw extruder: Simulation and experiment, Polymer Composites, 33 (2012) 2147-2158.

27. A. Durin, P. De Micheli, J. Ville, F. Inceoglu, R. Valette, B. Vergnes, A matricial approach of fibre breakage in twin-screw extrusion of glass fibres reinforced thermoplastics, Composites Part A: Applied Science and Manufacturing, 48 (2013) 47-56.
28. X. Jin, J. Wang, Fiber length Distribution Calculation in Injection Molding Simulation, SPE ANTEC, 2011.
29. F. Desplentere, W. Six, H. Bonte, E. Debrabandere, Influence of the power law index on the fiber breakage during injection molding by numerical simulations, NOVEL TRENDS IN RHEOLOGY V, AIP Publishing, 2013, pp. 90-106.
30. Z. Tadmor, Molecular orientation in injection molding, Journal of Applied Polymer Science, 18 (1974) 1753-1772.
31. O.L. Forgacs, S.G. Mason, Particle motions in sheared suspensions: X. Orbits of flexible threadlike particles, Journal of Colloid Science, 14 (1959) 473-491.
32. R. von Turkovich, L. Erwin, Fiber fracture in reinforced thermoplastic processing, Polymer Engineering & Science, 23 (1983) 743-749.
33. A. Salinas, J.F.T. Pittman, Bending and breaking fibers in sheared suspensions, Polymer Engineering & Science, 21 (1981) 23-31.
34. J.W. Hearle, B. Lomas, W.D. Cooke, Atlas of fibre fracture and damage to textiles, Elsevier, 1998.
35. D. Valentin, F. Paray, B. Guetta, The hygrothermal behaviour of glass fibre reinforced Pa66 composites: A study of the effect of water absorption on their mechanical properties, Journal of Materials Science, 22 (1987) 46-56.
36. P. Ren, G. Dai, Fiber dispersion and breakage in deep screw channel during processing of long fiber-reinforced polypropylene, Fibers and Polymers, 15 (2014) 1507-1516.
37. E. Hinch, The distortion of a flexible inextensible thread in a shearing flow, Journal of Fluid Mechanics, 74 (1976) 317-333.
38. K.K. Kabanemi, J.-F. Hétu, Effects of bending and torsion rigidity on deformation and breakage of flexible fibers: A direct simulation study, The Journal of chemical physics, 136 (2012) 074903.
39. R. Maurin, P. Davies, N. Baral, C. Baley, Transverse properties of carbon fibres by nano-indentation and micro-mechanics, Applied Composite Materials, 15 (2008) 61-73.
40. J.H. Phelps, C.L. Tucker, An anisotropic rotary diffusion model for fiber orientation in short-and long-fiber thermoplastics, Journal of Non-Newtonian Fluid Mechanics, 156 (2009) 165-176.
41. R.K. Mittal, V.B. Gupta, P.K. Sharma, Theoretical and experimental study of fibre attrition during extrusion of glass-fibre-reinforced polypropylene, Composites Science and Technology, 31 (1988) 295-313.
42. Y. Béreaux, J.Y. Charmeau, M. Moguedet, Modelling of fibre damage in single screw processing, International Journal of Material Forming, 1 (2008) 827-830.
43. H.J. Wolf, Screw plasticating of discontinuous fiber filled thermoplastic: Mechanisms and prevention of fiber attrition, Polymer Composites, 15 (1994) 375-383.
44. Z. Tadmor, I. Klein, Engineering principles of plasticating extrusion, Van Nostrand Reinhold Co., 1970.
45. F. Inceoglu, J. Ville, N. Ghamri, J.L. Pradel, A. Durin, R. Valette, B. Vergnes, Correlation between processing conditions and fiber breakage during compounding of glass fiber-reinforced polyamide, Polymer Composites, 32 (2011) 1842-1850.

46. K. Shon, D. Liu, J.L. White, Experimental Studies and Modeling of Development of Dispersion and Fiber Damage in Continuous Compounding, International Polymer Processing, 20 (2005) 322-331.
47. F. Berzin, B. Vergnes, J. Beaugrand, Evolution of lignocellulosic fibre lengths along the screw profile during twin screw compounding with polycaprolactone, Composites Part A: Applied Science and Manufacturing, 59 (2014) 30-36.
48. E. Lafranche, P. Krawczak, J.-P. Ciolczyk, J. Maugey, Injection moulding of long glass fiber reinforced polyamide 66: Processing conditions/microstructure/flexural properties relationship, Advances in Polymer Technology, 24 (2005) 114-131.
49. R. Hafellner, M. Pichler, R. Worndle, G. Steinbichler, P. Egger, Injection moulding long fibres-Fibre damage and effect of fibre length on the properties of LFT, Kunststoffe-Plast Europe, 90 (2000) 44-48.
50. G.A. Campbell, M.A. Spalding, Analyzing and Troubleshooting Single-Screw Extruders, Carl Hanser Verlag GmbH Co KG, 2013.
51. B. Fisa, Mechanical degradation of glass fibers during compounding with polypropylene, Polymer Composites, 6 (1985) 232-241.
52. M. Joshi, S.N. Maiti, A. Misra, R.K. Mittal, Influence of fiber length, fiber orientation, and interfacial adhesion on poly (butylene terephthalate)/polyethylene alloys reinforced with short glass fibers, Polymer Composites, 15 (1994) 349-358.
53. H. Bijsterbosch, R.J. Gaymans, Polyamide 6—long glass fiber injection moldings, Polymer Composites, 16 (1995) 363-369.
54. R.A.M. S.L. Villarroel, The effect of the injecion point location on the fiber glass length, Antec, (2007).
55. S. Tremblay, P. Lafleur, A. Ait-Kadi, Effects of injection parameters on fiber attrition and mechanical properties of polystyrene molded parts, The Journal of injection molding technology, 4 (2000) 1-7.
56. D. Cianelli, J. Travis, R. Bailey, How to process long-fiber reinforced thermoplastics, Plastics technology, 34 (1988) 84-89.
57. M. Rohde, A. Ebel, F. Wolff-Fabris, V. Altstädt, Influence of Processing Parameters on the Fiber Length and Impact Properties of Injection Molded Long Glass Fiber Reinforced Polypropylene, International Polymer Processing, 26 (2011) 292-303.
58. T.K. Hamada H, Development of New-type Glass Fiber Reinforced Thermoplastics, Antec (2002).
59. G.B. Jeffery, The motion of ellipsoidal particles immersed in a viscous fluid, Proc. R. Soc. Lond. A, 102 (1922) 161-179.
60. G.L. Hand, A theory of dilute suspensions, Archive for Rational Mechanics and Analysis, 7 (1961) 81-86.
61. S.G. Advani, C.L. Tucker III, The use of tensors to describe and predict fiber orientation in short fiber composites, Journal of Rheology (1978-present), 31 (1987) 751-784.
62. J. Ericksen, Transversely isotropic fluids, Colloid & Polymer Science, 173 (1960) 117-122.
63. J. Ericksen, Anisotropic fluids, Archive for Rational Mechanics and Analysis, 4 (1959) 231-237.
64. J. Ericksen, Theory of anisotropic fluids, Transactions of The Society of Rheology (1957-1977), 4 (1960) 29-39.

65. S.G. Advani, C.L. Tucker, Closure approximations for three-dimensional structure tensors, Journal of Rheology (1978-present), 34 (1990) 367-386.
66. K. Ericsson, S. Toll, J.-A. Månson, The two-way interaction between anisotropic flow and fiber orientation in squeeze flow, Journal of Rheology (1978-present), 41 (1997) 491-511.
67. P. Saffman, J. Turner, On the collision of drops in turbulent clouds, Journal of Fluid Mechanics, 1 (1956) 16-30.
68. T. Papthanasiou, D.C. Guell, Flow-induced alignment in composite materials, Elsevier, 1997.
69. A. Okagawa, R. Cox, S. Mason, The kinetics of flowing dispersions. VI. Transient orientation and rheological phenomena of rods and discs in shear flow, Journal of Colloid and Interface Science, 45 (1973) 303-329.
70. M. Rahnama, D.L. Koch, E.S. Shaqfeh, The effect of hydrodynamic interactions on the orientation distribution in a fiber suspension subject to simple shear flow, Physics of Fluids (1994-present), 7 (1995) 487-506.
71. F. Folgar, C.L. Tucker, Orientation Behavior of Fibers in Concentrated Suspensions, J Reinf Plast Comp, 3 (1984) 98-119.
72. R.S. Bay, C.L. Tucker, Fiber orientation in simple injection moldings. Part II: Experimental results, Polymer Composites, 13 (1992) 332-341.
73. D.H. Chung, T.H. Kwon, Fiber orientation in the processing of polymer composites, Korea-Aust. Rheol. J., 14 (2002) 175-188.
74. Y. Yamane, Y. Kaneda, M. Doi, The Effect of Interaction of Rodlike Particles in Semi-Dilute Suspensions under Shear Flow, Journal of the Physical Society of Japan, 64 (1995) 3265-3274.
75. Y. Yamane, Y. Kaneda, M. Dio, Numerical simulation of semi-dilute suspensions of rodlike particles in shear flow, Journal of non-newtonian fluid mechanics, 54 (1994) 405-421.
76. N. Phan-Thien, X.-J. Fan, R. Tanner, R. Zheng, Folgar–Tucker constant for a fibre suspension in a Newtonian fluid, Journal of Non-Newtonian Fluid Mechanics, 103 (2002) 251-260.
77. S. Ranganathan, S.G. Advani, Fiber–fiber interactions in homogeneous flows of nondilute suspensions, Journal of Rheology (1978-present), 35 (1991) 1499-1522.
78. S. Ranganathan, Mechanics of fiber-fiber interactions during the flow of non-dilute short fiber suspensions, University of Delaware, Ann Arbor, 1993, pp. 270-270 p.
79. R.S. Bay, Fiber orientation in injection-molded composites: a comparison of theory and experiment, University of Illinois at Urbana-Champaign, 1991.
80. M. Doi, S.F. Edwards, Dynamics of rod-like macromolecules in concentrated solution. Part 2, Journal of the Chemical Society, Faraday Transactions 2: Molecular and Chemical Physics, 74 (1978) 918-932.
81. B.E. VerWeyst, C.L. Tucker III, P.H. Foss, J.F. O'Gara, Fiber orientation in 3-D injection molded features: prediction and experiment, International Polymer Processing, 14 (1999) 409-420.
82. M. Sepehr, G. Ausias, P.J. Carreau, Rheological properties of short fiber filled polypropylene in transient shear flow, Journal of Non-Newtonian Fluid Mechanics, 123 (2004) 19-32.

83. A.P.R. Eberle, The dynamic behavior of a concentrated composite fluid containing non-Brownian glass fibers in rheometrical flows, Virginia Polytechnic Institute and State University, 2008.
84. H.M. Huynh, Improved fiber orientation predictions for injection-molded composites, University of Illinois at Urbana-Champaign, 2001.
85. J. Wang, Improved fiber orientation predictions for injection molded composites, ProQuest, 2007.
86. G. Vélez-García, S. Mazahir, P. Wapperom, D. Baird, Simulation of injection molding using a model with delayed fiber orientation, International Polymer Processing, 26 (2011) 331-339.
87. J. Wang, J.F. O'Gara, C.L. Tucker III, An objective model for slow orientation kinetics in concentrated fiber suspensions: Theory and rheological evidence, Journal of Rheology (1978-present), 52 (2008) 1179-1200.
88. C.L. Tucker III, J. Wang, J.F. O'gara, Method and article of manufacture for determining a rate of change of orientation of a plurality of fibers disposed in a fluid, Google Patents, 2007.
89. S.M. Mazahir, G.M. Vélez-García, P. Wapperom, D. Baird, Evolution of fibre orientation in radial direction in a center-gated disk: Experiments and simulation, Composites Part A: Applied Science and Manufacturing, 51 (2013) 108-117.
90. B.N. Nguyen, S.K. Bapanapalli, J.D. Holbery, M.T. Smith, V. Kunc, B.J. Frame, J.H. Phelps, C.L. Tucker, Fiber Length and Orientation in Long-Fiber Injection-Molded Thermoplastics — Part I: Modeling of Microstructure and Elastic Properties, Journal of Composite Materials, 42 (2008) 1003-1029.
91. D.L. Koch, A model for orientational diffusion in fiber suspensions, Physics of Fluids (1994-present), 7 (1995) 2086-2088.
92. X. Fan, N. Phan-Thien, R. Zheng, A direct simulation of fibre suspensions, Journal of Non-Newtonian Fluid Mechanics, 74 (1998) 113-135.
93. G.L. Hand, A theory of anisotropic fluids, Journal of Fluid Mechanics, 13 (1962) 33-46.
94. H.-C. Tseng, R.-Y. Chang, C.-H. Hsu, Phenomenological improvements to predictive models of fiber orientation in concentrated suspensions, Journal of Rheology (1978-present), 57 (2013) 1597-1631.
95. E.M. Silverman, Effect of glass fiber length on the creep and impact resistance of reinforced thermoplastics, Polymer Composites, 8 (1987) 8-15.
96. U. Strautins, Flow-driven orientation dynamics in two classes of fibre suspensions, Ph. D. thesis, Technical University Kaiserslautern, 2008.
97. K. Ortman, D. Baird, P. Wapperom, A. Whittington, Using startup of steady shear flow in a sliding plate rheometer to determine material parameters for the purpose of predicting long fiber orientation, Journal of Rheology (1978-present), 56 (2012) 955-981.
98. K.J. Meyer, Improved Prediction of Glass Fiber Orientation in Basic Injection Molding Geometries, (2013).
99. S.G. Advani, C.L. Tucker, A numerical simulation of short fiber orientation in compression molding, Polymer Composites, 11 (1990) 164-173.
100. D. MASAO, Molecular dynamics and rheological properties of concentrated solutions of rodlike polymers in isotropic and liquid crystalline phases, Journal of Polymer Science: Polymer Physics Edition, 19 (1981) 243.

101. M. Doi, Molecular-dynamics and rheological properties of concentrated-solutions of rodlike polymers in isotropic and liquid-crystalline phases, Journal of Polymer Science Part B-Polymer Physics, 19 (1981) 229-243.
102. D.H. Chung, T.H. Kwon, Invariant-based optimal fitting closure approximation for the numerical prediction of flow-induced fiber orientation, Journal of Rheology (1978-present), 46 (2002) 169-194.
103. J.S. Cintra Jr, C.L. Tucker III, Orthotropic closure approximations for flow-induced fiber orientation, Journal of Rheology (1978-present), 39 (1995) 1095-1122.
104. D.H. Chung, T.H. Kwon, Improved model of orthotropic closure approximation for flow induced fiber orientation, Polymer Composites, 22 (2001) 636-649.
105. V. Verleye, A. Couniot, F. Dupret, Prediction of fiber orientation in complex injection molded parts, ICCM/9., 1993, pp. 642-650.
106. f. Dupret, V. Verleye, Modelling the flow of fiber suspensions in narrow gaps, in: D.D.K. D.A. Siginer, R.P. Chhabra (Eds.) Rheology Series, Elsevier, 1999, pp. 1347-1398.
107. B. Ver Weyst, C. Tucker III, P. Foss, The Optimized Quasi-Planar Approximation for Predicting Fiber Orientation in Injection-Molded Composites 1, International Polymer Processing, 12 (1997) 238-248.
108. C.L. Tucker III, Flow regimes for fiber suspensions in narrow gaps, Journal of Non-Newtonian fluid mechanics, 39 (1991) 239-268.
109. G. Ausias, J.-F. Agassant, M. Vincent, P. Lafleur, P.-A. Lavoie, P. Carreau, Rheology of short glass fiber reinforced polypropylene, Journal of Rheology (1978-present), 36 (1992) 525-542.
110. G.B. Jeffery, The motion of ellipsoidal particles immersed in a viscous fluid, Proceedings of the Royal Society of London. Series A, Containing Papers of a Mathematical and Physical Character, (1922) 161-179.
111. F.P. Bretherton, The motion of rigid particles in a shear flow at low Reynolds number, Journal of Fluid Mechanics, 14 (1962) 284-304.
112. G.G. Lipscomb Ii, M.M. Denn, D.U. Hur, D.V. Boger, The flow of fiber suspensions in complex geometries, Journal of Non-Newtonian Fluid Mechanics, 26 (1988) 297-325.
113. E. Hinch, L. Leal, The effect of Brownian motion on the rheological properties of a suspension of non-spherical particles, Journal of Fluid Mechanics, 52 (1972) 683-712.
114. G. Batchelor, The stress system in a suspension of force-free particles, Journal of fluid mechanics, 41 (1970) 545-570.
115. J.G.V. Evans, flow of a suspension of force-free rigid rods in a Newtonian fluid, 1975.
116. J. Evans, The effect of non-Newtonian properties of a suspension of rod-like particles on flow fields, Theoretical Rheology, Halstead Press, New York, (1975) 224-232.
117. R.G. Larson, The Structure and Rheology of Complex Fluids (Topics in Chemical Engineering), RG Larson.—1998.—688 p, (1998).
118. G.K. Batchelor, The stress generated in a non-dilute suspension of elongated particles by pure straining motion, Journal of Fluid Mechanics, 46 (1971) 813-829.
119. S. Chung, T. Kwon, Numerical simulation of fiber orientation in injection molding of short-fiber-reinforced thermoplastics, Polymer Engineering & Science, 35 (1995) 604-618.
120. E.S.G. Shaqfeh, G.H. Fredrickson, The hydrodynamic stress in a suspension of rods, Physics of Fluids A: Fluid Dynamics (1989-1993), 2 (1990) 7-24.
121. M.A. Bibbó, Rheology of semiconcentrated fiber suspensions, Massachusetts Institute of Technology, 1987.

122. C.A. Stover, The dynamics of fibers suspended in shear flows, Cornell University, Ann Arbor, 1991, pp. 197-197 p.
123. M. Djalili-Moghaddam, S. Toll, A model for short-range interactions in fibre suspensions, Journal of Non-Newtonian Fluid Mechanics, 132 (2005) 73-83.
124. J. Férec, G. Ausias, M. Heuzey, P. Carreau, Modeling fiber interactions in semiconcentrated fiber suspensions, Journal of Rheology (1978-present), 53 (2009) 49-72.
125. N. Phan-Thien, A. Graham, A new constitutive model for fibre suspensions: flow past a sphere, Rheologica acta, 30 (1991) 44-57.
126. T. Kitano, T. Kataoka, T. Shirota, An empirical equation of the relative viscosity of polymer melts filled with various inorganic fillers, Rheologica Acta, 20 (1981) 207-209.
127. A.P. Eberle, D.G. Baird, P. Wapperom, G.M. Vélez-García, Obtaining reliable transient rheological data on concentrated short fiber suspensions using a rotational rheometer, Journal of Rheology (1978-present), 53 (2009) 1049-1068.
128. K.C. Ortman, N. Agarwal, A.P. Eberle, D.G. Baird, P. Wapperom, A.J. Giacomin, Transient shear flow behavior of concentrated long glass fiber suspensions in a sliding plate rheometer, Journal of Non-Newtonian Fluid Mechanics, 166 (2011) 884-895.
129. C.G. Joung, N. Phan-Thien, X.J. Fan, Direct simulation of flexible fibers, Journal of Non-Newtonian Fluid Mechanics, 99 (2001) 1-36.
130. S. Goto, H. Nagazono, H. Kato, The flow behavior of fiber suspensions in Newtonian fluids and polymer solutions, Rheologica Acta, 25 (1986) 119-129.
131. M. Keshtkar, M.-C. Heuzey, P.J. Carreau, M. Rajabian, C. Dubois, Rheological properties and microstructural evolution of semi-flexible fiber suspensions under shear flow, Journal of Rheology (1978-present), 54 (2010) 197-222.
132. R.S. Bay, C.L. Tucker, Fiber orientation in simple injection moldings. Part I: Theory and numerical methods, Polymer Composites, 13 (1992) 317-331.
133. D.H. Chung, T.H. Kwon, Numerical studies of fiber suspensions in an axisymmetric radial diverging flow: the effects of modeling and numerical assumptions, Journal of Non-Newtonian Fluid Mechanics, 107 (2002) 67-96.
134. S.M. Mazahir, G.M. Vélez-García, P. Wapperom, D. Baird, Fiber orientation in the frontal region of a center-gated disk: Experiments and simulation, Journal of Non-Newtonian Fluid Mechanics, 216 (2015) 31-44.
135. P.C. Wu, C.F. Huang, C.G. Gogos, Simulation of the mold-filling process, Polymer Engineering & Science, 14 (1974) 223-230.
136. M.C. Altan, S. Subbiah, S.I. Güçeri, R.B. Pipes, Numerical prediction of three-dimensional fiber orientation in Hele-Shaw flows, Polymer Engineering & Science, 30 (1990) 848-859.
137. S.T. Chung, T.H. Kwon, Coupled analysis of injection molding filling and fiber orientation, including in-plane velocity gradient effect, Polymer Composites, 17 (1996) 859-872.
138. M. Gupta, K.K. Wang, Fiber orientation and mechanical properties of short-fiber-reinforced injection-molded composites: Simulated and experimental results, Polymer Composites, 14 (1993) 367-382.
139. J.A. Dantzig, C.L. Tucker, Modeling in materials processing, Cambridge university press, 2001.

140. S. Ranganathan, S.G. Advani, A simultaneous solution for flow and fiber orientation in axisymmetric diverging radial flow, Journal of Non-Newtonian Fluid Mechanics, 47 (1993) 107-136.
141. B.E. Verweyst, C.L. Tucker, Fiber suspensions in complex geometries: flow/orientation coupling, The Canadian Journal of Chemical Engineering, 80 (2002) 1093-1106.
142. M.C. Altan, Rheology of fiber suspensions and fiber orientation analysis in flow processes, 1990.
143. W. Rose, Fluid-fluid interfaces in steady motion, Nature, 191 (1961) 242-243.
144. D.G. Baird, D.I. Collias, Polymer processing: principles and design, John Wiley & Sons, 2014.
145. K.-H. Han, Y.-T. Im, Numerical simulation of three-dimensional fiber orientation in infection molding including fountain flow effect, Polymer Composites, 23 (2002) 222.
146. G.M. Vélez-García, Experimental evaluation and simulations of fiber orientation in injection molding of polymers containing short glass fibers, Virginia Polytechnic Institute and State University, 2012.
147. W.F. Haverty, Squeeze flow behavior of short fiber/thermoplastic composites, 1991.
148. M.C. Altan, S.İ. Güçeri, R.B. Pipes, Anisotropic channel flow of fiber suspensions, Journal of Non-Newtonian Fluid Mechanics, 42 (1992) 65-83.
149. S.M. Mazahir, Improvement in Orientation Predictions of High-Aspect Ratio Particles in Injection Mold Filling Simulations, (2013).

Chapter 3 Development of a Fiber Length Measurement Method for Injection Molded Discontinuous Fiber Reinforced Thermoplastics

3.1 Abstract

The residual fiber length in the final part is of great significance influencing the properties of injection molded discontinuous fiber reinforced thermoplastic composites. During the plasticating stage of injection molding, intense fiber attrition occurs leading to a broad fiber length distribution. In this article a new fiber length measurement method with reproducible sampling procedure in a timely manner was described. In this work was also proposed an automatic fiber length measurement algorithm supported by Matlab®. The accuracy of this automatic algorithm was evaluated by comparing the measured results using this in-house developed tool with the manual measurement and good agreement between the two methods is observed. Finally, the developed measurement technique was used to investigate the fiber breakage as a function of fiber concentration and geometry location for samples produced in an injection molded center-gated-disk (CGD). The results showed that increased fiber concentration lead to more intense fiber attrition, and a slight increase in fiber length is observed in the advancing front compared to the fully-developed Hele-Shaw region.

3.2 Introduction

Discontinuous fiber-reinforced thermoplastics created by injection molding are widely used in the automotive industry [1]. The increased importance of these materials is contributed to the combination of mechanical properties and melt processability leading to relatively low manufacturing cost with high application value. During the injection molding process, especially in the plasticating unit, fiber breakage occurs and leads to a broad fiber length distribution (FLD) [2]. In the mold cavity, the complex flow pattern contributes to another microstructural variable, the fiber orientation distribution (FOD) [3]. Mechanical performance of a part is strongly dependent on these microstructural variables [4]. Ultimately, an accurate characterization of both fiber length and fiber orientation is the prerequisite for accurate predictions of the heterogeneity in mechanical properties. The main goal of this article is to develop a reliable experimental fiber length measurement method with an automatic image processing algorithm quantifying the FLD from the scanned images containing collected fibers.

Although long fibers are favored over short ones in terms of better mechanical properties, the injection molding process subjects the fibers to extensive fiber breakage. The inevitable fiber attrition can reduce the fiber length from the initial ~ 10 mm to slightly above 1 mm, resulting in decreased tensile strength and impact resistance. The majority of fiber breakage occurs in the plasticating stage during injection molding. Wolf et al. [5] identified several major mechanisms of fiber breakage during the plasticating phase including squeezing of solid pellets in the feed, interaction between granules during the solid conveying region, shear and friction at various locations (through flight clearance, near barrel wall and screw root), and bending as well as buckling of fibers in the melt.

To gain insight into the underlying physics of fiber breakage, it is important to study the effects of processing parameters on the residual fiber length in the injection–molded parts. Lafranche et al. [6] showed that a faster screw rotational speed help to preserve the residual fiber length. In contrast, several authors reported that lower speeds help to maintain the fiber length [7, 8]. Villarrorel et al. [9] investigated the injection speed and suggested that a lower value helped to reduce fiber breakage. Cianelli et al. [10] found that considerable damage to glass fiber occurred if processing was carried out with high back pressure. This conclusion was also confirmed by Bailey et al. [11]. Although the mechanisms of fiber breakage have still not been fully understood, it is a general finding that mild processing conditions might be beneficial to reduce the extent of fiber breakage and maintain the residual fiber length.

A reliable characterization of the fiber length distribution is the prerequisite to gain insight into the fiber breakage mechanism. An ideal procedure for fiber length measurement is to do a full analysis of a sufficiently large sample which normally contains hundreds of thousands of fibers [12]. However, the time-consuming analysis of such a large number of fibers might limit the application of this approach. A down-sampling step is widely used to decrease the collected number of fibers that needs to be characterized from hundreds of thousands of fibers [13]. The selection of the sub-sample is commonly done manually by collecting fibers at the location of interest using general tools like tweezers. However, the handling of the fibers with tweezers is quite arbitrary and results in the loss of very short fibers. For the first time, Kunc et al. [14] proposed a systematic down-sampling method significantly improved the fiber length measurement procedure. In this method, a continuous stream of epoxy is injected through the entire thickness of the fiber stack to form an epoxy-plug with fibers captured within the epoxy plug volume. The number of fibers collected from the specimen is proportional to the epoxy plug volume (diameter of the cylinder). From our trials and other authors' reports [13] the collected number of fibers by this epoxy-plug method can be above 10,000 . This sampling method biases longer fibers, and the measured number of fiber needs to be corrected based on the fiber length and the diameter of the epoxy-plug. The diameter is normally assumed to be constant, which is most likely not be true. Kunc et al. [14] used an actuator for better control of needle withdrawal rate. However, they didn't comment on the uniformity of the diameter of the epoxy-plug. However, the extracted glass fiber-and-epoxy "plug" specimen as shown in ref. [15] has a diameter with noticeable variation in size from top to bottom. Figure 3-3 (c) shows a typical glass fiber-and-epoxy "plug" specimen obtained in our lab using the same resin showing a significant diameter deviation from top to bottom. Goris et al. [13] generated a fairly uniform epoxy column which mostly contains 15,000 to 50,000 fibers. They chose a type of ultraviolet curable epoxy which can be easily injected through a 20 G hypodermic needle and form a plug with uniform thickness. In this work, we developed a novel and simple "needle" method generating quite a uniform sampling diameter which is independent of the choice of epoxy. Furthermore, the total number of collected fibers can be controlled by using different sizes of needles. The smallest needle (0.8 mm diameter) used in this study can significantly reduce the number of collected fibers when compared to the epoxy-plug method and, thus, reduce the amount of work like fiber dispersion and generation of the digital image

Normally, the next step following the collection of fibers is to burn off the epoxy (if epoxy used in the previous step), disperse the collected fibers and create digital images of fibers using either a microscope or an office scanner. The scanner is favored over the microscope, because of its lower cost and larger imaging size (which is necessary for longer fibers with length much longer than 1 mm). The size of scanned image and the resolution (dpi) allowed are two competing factors. The quality of the scanned image is commonly not good enough and certain image processing is necessary to improve the “clarity” of the fibers. In this article, the canny-edge-detection algorithm [16] was applied which can significantly improve the image quality. Manual fiber length measurement using software (ImageJ®) is a cumbersome task. Therefore, in this paper we also proposed an automatic fiber length measurement technique. The accuracy of this automatic algorithm was evaluated by comparing the measured results using this in-house developed tool with the manual measurement, showing good agreement between the two.

Finally, the developed measurement technique was used to investigate the fiber breakage as a function of fiber concentration and geometry location in an injection molded center-gated-disk (CGD). The results showed that increased fiber concentration lead to more intense fiber attrition, and a slight increase in fiber length is observed in the advancing front compared to the fully-developed Hele-Shaw region.

3.3 Experimental

3.3.1 Injection Molding of Center-Gated Disk

The materials used in this paper are 10, 30, 40 and 50 wt% glass fibers with a polypropylene (PP) matrix. The material was supplied by SABIC Innovative Plastics as 12.5 mm long pellets created through a pultrusion process for 30 and 50 wt% formulations. Samples with 10 wt% fibers were generated by diluting the 30 wt% pellets with neat polypropylene, while 30 and 50 wt% pellets were combined to create the 40 wt% composites. The injection molding of these materials was conducted on a Boy 35 E injection molding machine. The temperature zones in the injection molding machine was set to 200, 210, 230, 230, and 230 ℃ with a mold temperature of 90 ℃. The mold filling time was about 1 s. The sample geometry investigated is a simple center-gated disk (CGD) as in Figure 3-1. In this work, the Hele-Shaw region A (60% disk radius) and the advancing front region B (85% disk radius) as shown in Figure 3-1 were investigated for fiber length to study the concentration effects on fiber breakage.

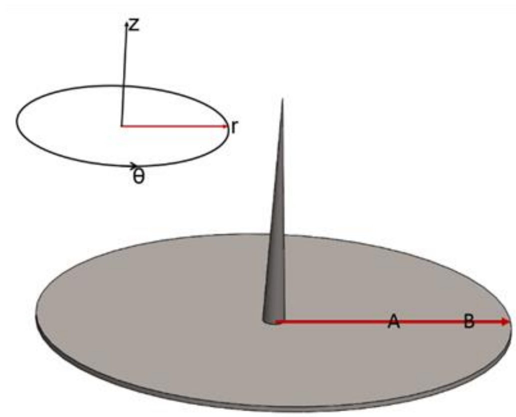

Figure 3-1: The injection–molded center-gated-disk: the Hele-Shaw region A (60% disk radius) and advancing front region B (85% disk radius) were investigated in this study.

Due to the compounding process, the injection molded LFTs will end up with a very broad fiber length distribution. The actual fiber length information can be described by the experimentally obtained probability of finding a fiber with length l_i given by:

$$pl(l_i) = \frac{N_i}{\sum N_i}. \tag{3-1}$$

Here, N_i is the measured number of fibers with length l_i. A realatively concise way is to replace the FLD with a single length, namely the number or weight average length defined, respectively, as:

$$L_n = \frac{\sum N_i \, l_i}{\sum N_i} \tag{3-2}$$

$$L_w = \frac{\sum N_i \, l_i^2}{\sum N_i l_i}. \tag{3-3}$$

3.3.2 A Novel Fiber Length Measurement Method

We developed a novel fiber length measurement technique as described in Figure 3-2. In this method, the z-poxy® 15 minute formula was used. The sample is wrapped and constrained tightly by aluminum foil to ensure that the fibers stay in place during pyrolysis. The general steps including pyrolysis, fiber dispersion and image scan are basically the same as for other measurement techniques. The key feature of this new method is to use a needle coated with a thin layer of epoxy to collect the fibers at the point of interest. Specifically, the needle is inserted through the entire thickness of the fiber stack, and the fibers contacted with the needle surface are thereby bonded *in-situ* to the thin epoxy layer. After the epoxy is cured, all surrounding fibers not attached to the needle surface are removed carefully by applying short blasts of low pressure air. Because only a very thin layer of epoxy is applied on the surface of the needle, and the epoxy surface is fully covered by collected fibers, it is hard to see any irregular geometry formed by the cured epoxy as shown in Figure 3-3. Bailey and Kraft [11] found the average fiber length in the center layer was three times of those in the skin layer near the wall, a phenomenon attributed to the high shear rates in the skin during mold filling. Phelps and Tucker's [17] numerical simulation also indicated the fiber length was location dependent across the cavity thickness. A uniform sampling region through the entire thickness of the fiber stack is the first step to avoid measurement bias. Even under this prerequisite, the down-sampling of fibers is still biased due to the preferential capture of long fibers as shown in Figure 3-4. The correction of the type of skewed result is also based on the geometry (diameter) of the sampling region. Therefore, creating a uniform geometry through the entire thickness of the sampling region is important to get a reliable measurement of fiber length.

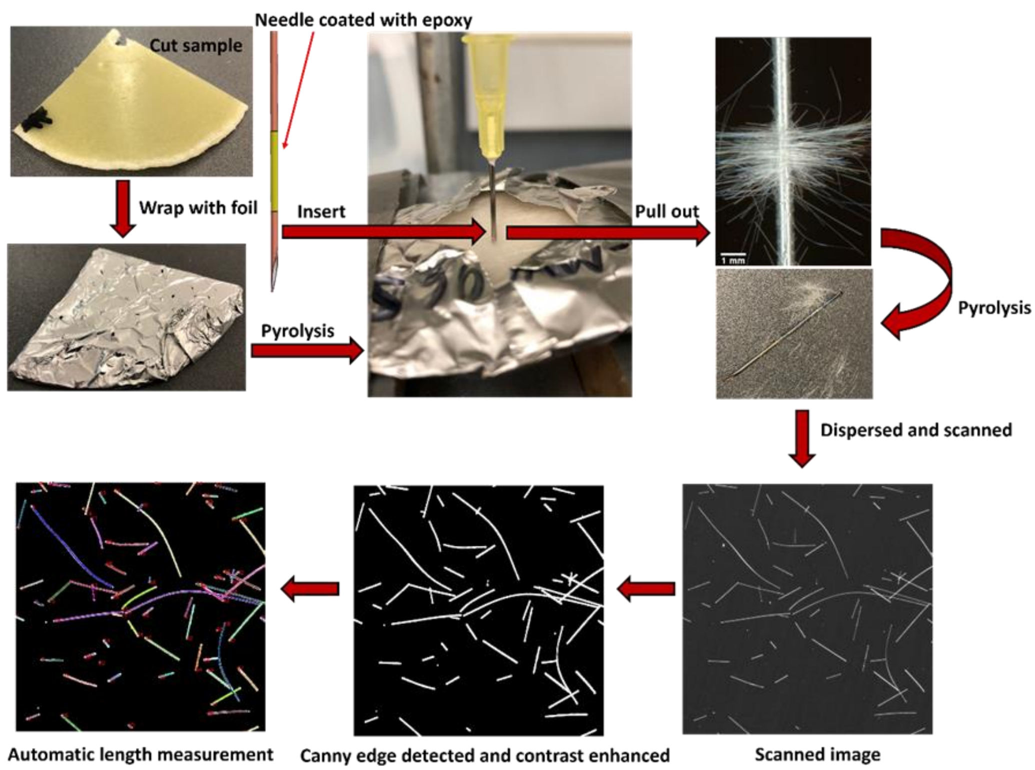

Figure 3-2: Main steps of the novel fiber length measurement method ("needle" method).

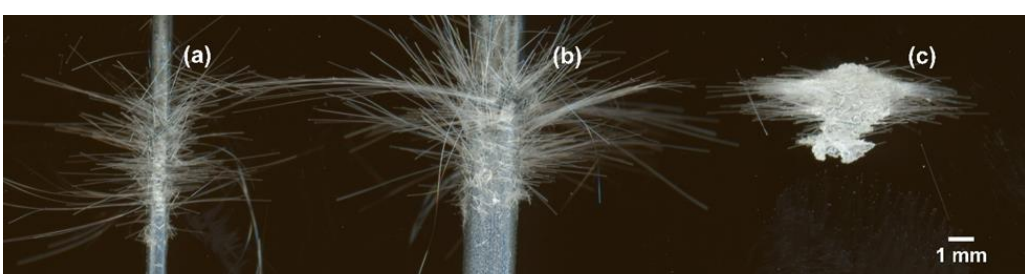

Figure 3-3: Collected glass fibers through the entire thickness of the sample using (a) 0.8 mm diameter needle, (b) 2.09 mm diameter needle, and (c) epoxy-plug.

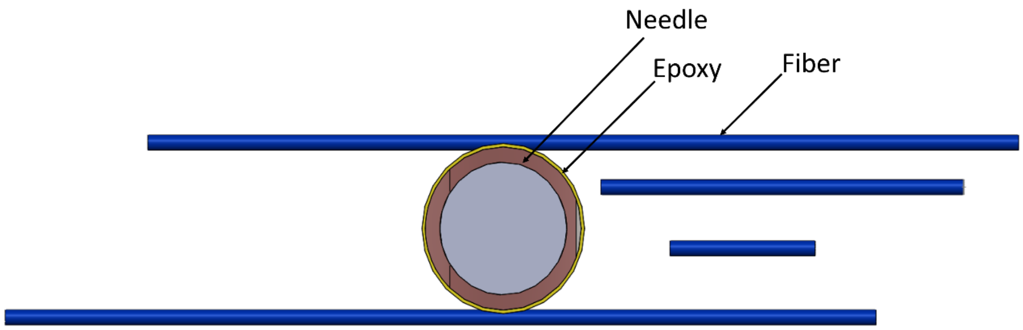

Figure 3-4: Schematic representation indicating the bias of down-sampling of fibers due to the preferential capture of long fibers.

3.4 Automatic Fiber Length Measurement Method

Manual fiber length measurements using software (ImageJ®) is a cumbersome task. Therefore, in this paper we also proposed an automatic fiber length measurement technique. Normally, the next step following the collection of fibers is to burn off the epoxy (if epoxy used in the previous step), disperse the collected fibers and create digital images of fibers using either a microscope or an optical document scanner. The scanner is favored over the microscope, because of its lower cost and larger imaging size (which is necessary for longer fibers with length much longer than 1 mm). The quality of the scanned image is commonly not good enough and certain image processing is necessary to improve the "clarity" of the fibers. In this article, the canny-edge-detection algorithm [16] is applied which can improve the image quality in the black and white format.

The automatic fiber length measurement is conducted with a black and white format image. The pixels of value one are elements of a fiber (white), while the pixels of value zero are the background (black). The fiber length measurement mechanism is illustrated in

Figure 3-5. To start tracing the fibers, the fiber end is used as the first tracing point. To find the fiber end, the fiber is transformed into a one pixel thick line. Ends are identified by choosing the points with the least number of local neighbors with a value of one. The located fiber end in Figure 3-5 (a) is presented by a blue-star marker. To find the second tracing point, pixels (points) with a constant distance r from the fiber end are located and found along the fiber direction as illustrated by the black-star markers. The next step is to calculate the length/distance from these black-star points to their corresponding closest background points (with a value of zero). The black-star point with the largest value has a great chance to locate along the center line of the fiber. So, this point is chosen as the second tracing point and highlighted by the green circle as shown in Figure 3-5 (a). After the first two tracing points are identified, an additional criterion is applied to locate the following tracing points. Specifically, the angle between the line connecting the previous two tracing point, and the line connecting the currently located black-star point and the closest previous tracing point is calculated. If the value is larger than a threshold value (170°), then this black-star point will be selected as a potential tracing point and highlighted with red-square marker shown in Figure 3-5 (a). Then the tracing point is further identified among those red-square points using the previously used length/distance criterion. The reason for applying this additional angle threshold condition is to guarantee an optimal choose of the tracing point at the intersection of crossing fibers. A fully traced crossing fiber network is presented in Figure 3-5 (b). The traced color lines show good agreement with the fibers. The fiber length is determined by the traced multiple length of r started from the first fiber end to the following tracing points.

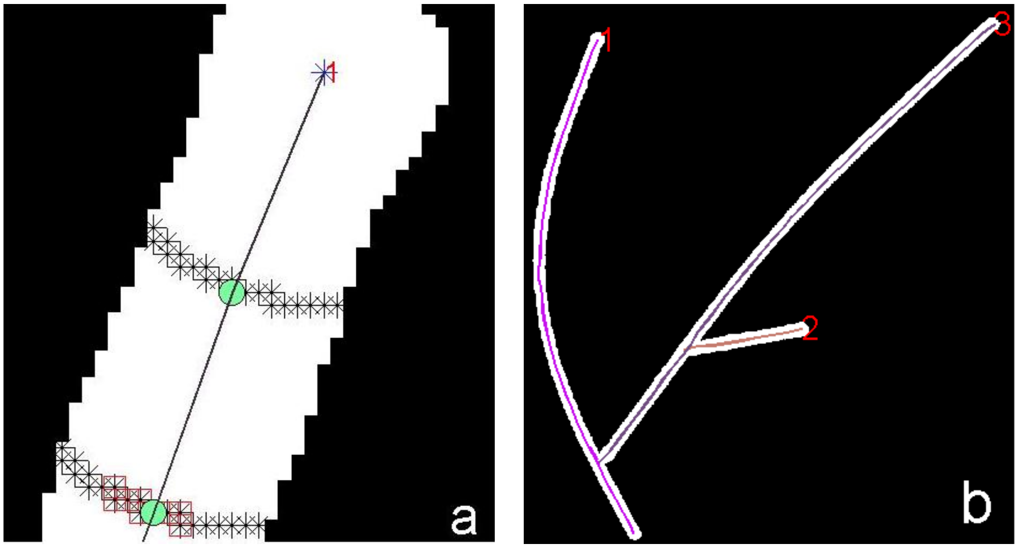

Figure 3-5**:** Automatic fiber length measurement: (a) fiber tracing mechanism, and (b) fully measured crossing fibers.

3.5 Results and Discussion

3.5.1 Verification of the New Fiber Length Measurement Technique

To evaluate this novel "needle" method and develop a function to correct the skewed result from the preferential capture of long fibers, five needles with different sizes were applied to collect fibers at the same radius location of the 30 wt% glass fiber and polypropylene CGD as shown in Figure 3-6. All measurements for each needle size were repeated 3 times to ensure accurate results. The cumulative distribution of measured fiber length shown in Figure 3-7 (a) was evaluated by the summation of three repeated results for each needle size. The experimental probability described by Eq. (3-1) was used to calculate the corresponding cumulative value. All results from different needles show very similar trends. Generally, the percentage of shorter fibers collected is increased with the needle diameter attributed to the increased surface area of larger needle. The only exception occurs from 0.45 to 1.36 mm between 2.09 mm and 2.78 mm diameter needles. This might be due to some artificial factors during the measurement or the difference between the short fiber capturing ability decreases with the increase of needle diameter (contact surface area). However, beyond 1.36 mm, the cumulative distribution curve of the largest needle (2.78 mm) surpasses the results from all the other needles, giving the shortest L_n and L_w shown in Figure 3-7 (b). Both values of the L_n and L_w turn out to decrease with the rise of needle diameter. Moreover, the number of measured fibers shows a monotonic increase from the smallest needle to the largest one. These results confirmed the bias of down-sampling and suggest that a sufficiently large sample might provide measurement approaching the 'true' length distribution. The goal of developing a new fiber length measurement method is to reduce the sampling size (increase the efficiency) but still obtain a reliable measurement. A correction equation based on each fiber length and the geometry of the sampling region is necessary to fulfill this object. We believe the measured fiber length should be independent of the needle size and after the correction the deviations among results from the five different needles should be very small.

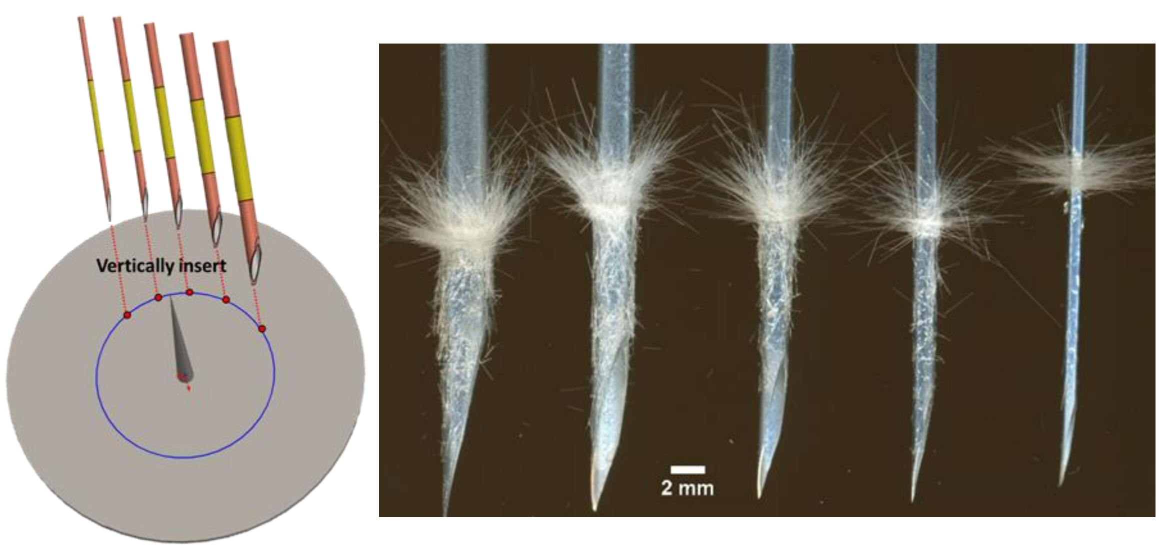

(a) (b)

Figure 3-6**:** A designed experiment to evaluate this new "needle" method and develop a function to correct the skewed result from the preferential capture of long fibers: (a) in this experiment, five needles with different sizes were applied to collect fibers at the same radius location, and (b) collected glass fibers through the entire thickness of the sample using five sizes needles.

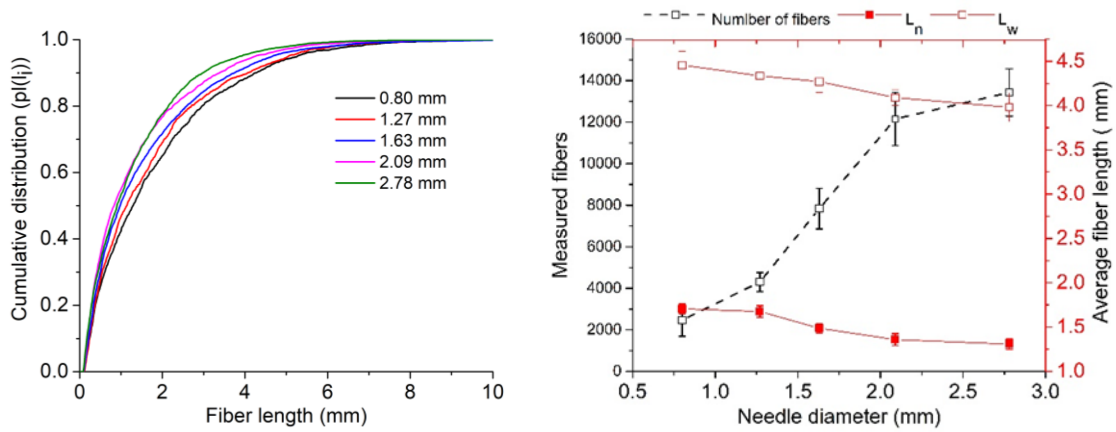

(a) (b)

Figure 3-7**:** Fiber length results obtained using 5 different needles at the same radius location: (a) cumulative fiber distribution, and (b) number average, weight average fiber length, and total number of measured fibers for each needle size.

Intuitively, the possibility of capturing a fiber near the needle is proportional to the ratio of the fiber surface area to the epoxy surface area described as: $(\pi * d_0) * l_i \Big/ (\pi * H) * d_n$. Here d_0 is the single fiber diameter and H the fiber stack thickness, which are fixed for each system. The variable parameters are the specific fiber length l_i and the needle diameter d_n. We referred to the format provided by Kunc [18] and proposed our correction equation as :

$$N_i(corrected) = N_i(measured)/(1 + \frac{L_c * l_i}{d_n}). \quad (3\text{-}4)$$

Where, N_i is the number or possibility of fibers with length l_i, and L_c the empirical length correction parameter includes all the uncertain effects. According to this equation, when the fiber length l_i is small enough compared to a sufficiently large needle diameter d_n, then $N_i(corrected) \approx N_i(measured)$. While, a longer fiber relative to the needle size would result in a higher degree of correction. To obtain the value for the empirical parameter L_c, the proposed model was used to reduce the deviations among L_n obtained from different needles for 30 wt% GF-PP composites using non-linear least-squares solver. As a result, the value of the dimensionless empirical parameter L_c was determined as 0.485. The L_w is also corrected using the same L_c. The results before and after correction are shown in Figure 3-8. The magnitudes of both L_n and L_w from 5 different needles were reduced and turned to be more uniform after the correction. This new measurement technique were used for all of our fiber length measurement using a 0.8 mm diameter needle and the correction equation in the form of Eq. (3-4) with $L_c = 0.485$.

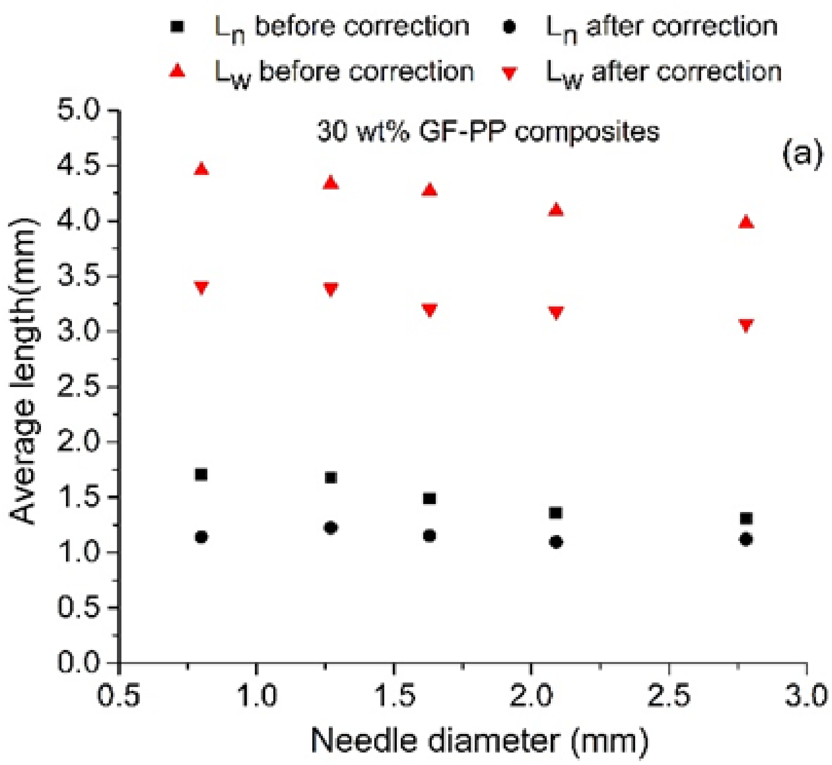

Figure 3-8: The measured L_n and L_w before and after the correction for 30 wt% GF-PP composites.

3.5.2 Verification of the Automatic Fiber Length Measurement Algorithm

To evaluate the accuracy of the fiber length measurement algorithm (using codes), the automatic measured fiber length distribution is compared with the manual measurement (using ImagJ®) as shown in Figure 3-9. This is a side by side comparison in which the neighbored red and black bar share the same value of l_i corresponding to the x axis value at their shared boundary. The fiber length distributions from two types of measurements show good agreement, and only a slight difference has been observed. The results of L_n, L_w, and measured number of fibers are listed in Table 3-1. The measured average fiber lengths from automatic codes and manual method using ImageJ® are pretty comparable. There is only about a 10 % difference between the values of L_w. The codes measured more fibers than the manual measurement. First, there is inevitable noise in the scanned image due to dust and fingerprints, which are considered as fibers by the codes. Second, during the manual measurement, operator might neglect those fibers with very small sizes. However, the automatic measurement algorithm can generate a reliable fiber length distribution compared to manual processing.

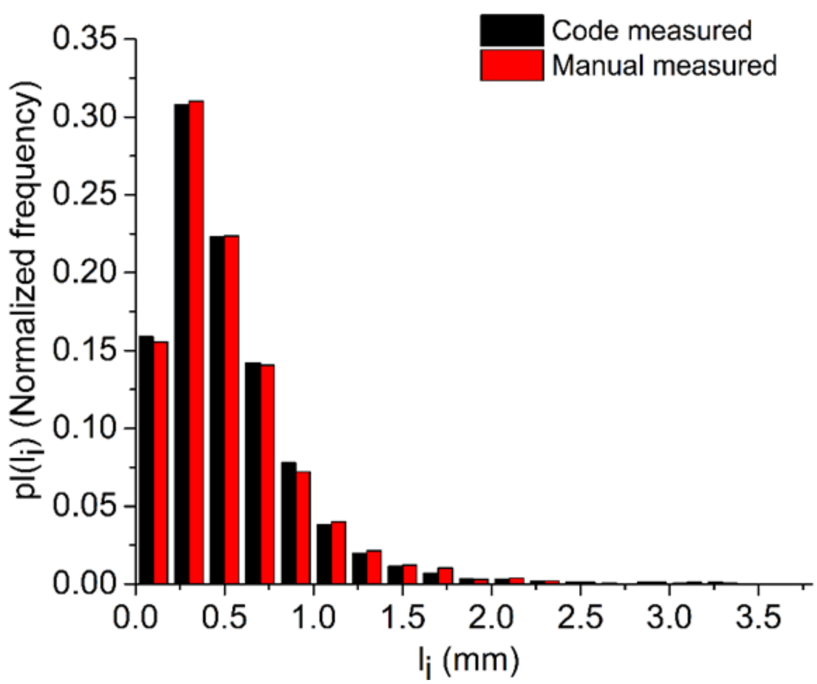

Figure 3-9: Side by side comparison of fiber length distribution between automatic and manual measurements (this is a side-by-side comparison in which the neighbored red and black bar share the same value of l_i corresponding to their shared boundary).

Table 3-1: Comparison between manual and automatic measurements.

	L_n(mm)	L_w(mm)	Measured fibers
Manual	0.53	0.84	3275
Automatic	0.52	0.78	3588

3.5.3 Concentration Effects on Fiber Breakage

The developed measurement technique was used to investigate the fiber breakage as a function of fiber concentration and geometry location in an injection-molded center-gated disk (CGD). The results are shown in Figure 3-10. The number average fiber lengths in these samples decrease with increasing fiber content. Results of Weight average fiber length have a similar trend, but the only exception occurs for 10 wt% concentration at advancing front. The value measured at this location for 10 wt% has a very large error bar. This might due to artificial factors during fiber length measurement. The number average fiber length at advancing front is slightly larger than those at the hele-shaw region for 10 wt% and 30 wt% materials. Similar phenomena was also observed by Phelps and Tucker [17]. An hypothesis for this observed phenomenon is the effect of fiber pull-out at the interface between the solidified layer and molten core during mold filling [19].

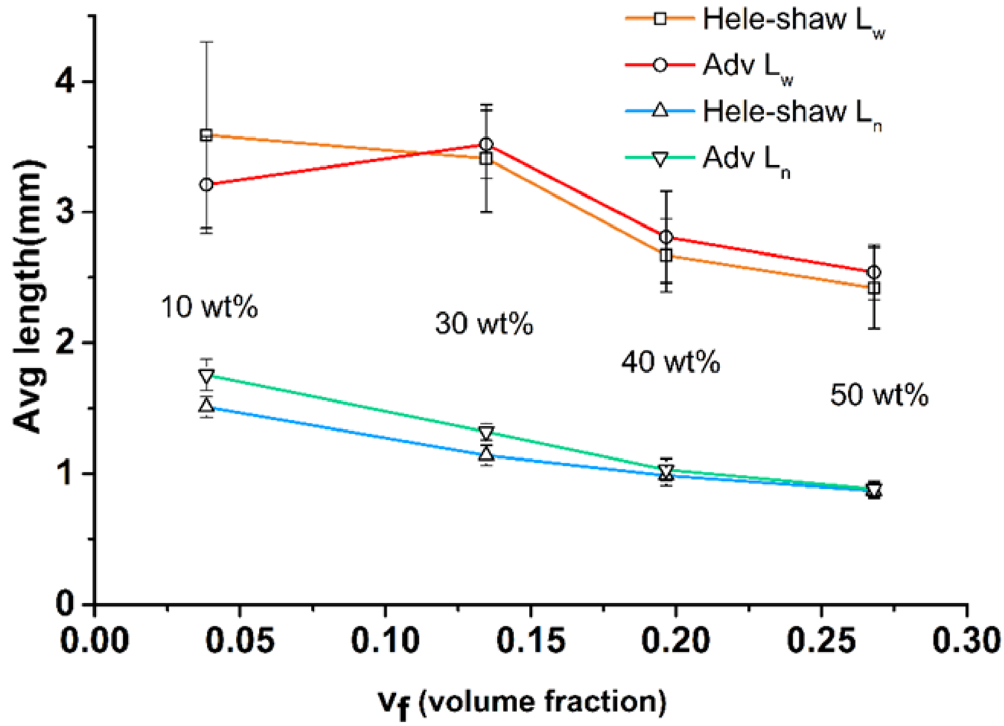

Figure 3-10: Measured L_n and L_w for 10 wt% , 30 wt%, 40 wt% and 50 wt% GF-PP CGD at both hele-shaw (60 % disk radius) and advancing front (85 % disk radius).

3.6 Conclusion

A reliable measurement of the residual fiber length distribution is the prerequisite to gain insight into the fiber breakage mechanism. In this work, we developed a new and simple "needle" method generating quite uniform sampling diameter which is independent of the choosing of epoxy. Furthermore the total number of collected fibers can be controlled by using different sizes of needles. The smallest needle (0.8 mm diameter) used in this study can significantly reduce the number of collected fibers when compared to the epoxy-plug method, and thus reduce the amount of work like fiber dispersion and generation of the digital image. A correction equation was developed to modify the skewed result due to the preferential capturing of long fibers. After applying this equation, the measured results from using five different needles turned out to be more uniform compared to the original results.

Manual fiber length measurement using software (ImageJ®) is a cumbersome task. Therefore, in this paper we also proposed an automatic fiber length measurement technique. The accuracy of this automatic algorithm was evaluated by comparing the measured results using this in-house developed tool with the manual measurement, showing good agreement between the two.

The developed measurement technique was used to investigate the fiber breakage as a function of fiber concentration and geometry location in injection molded center-gated-disk (CGD). The results showed that increased fiber concentration lead to more intense fiber attrition and a slight increase in number average fiber length is observed in the advancing front compared to the fully-developed hele-shaw region for 10 wt% and 30 wt% GF-PP composites.

References

1. F. Henning, H. Ernst, R. Brüssel, LFTs for automotive applications, Reinforced Plastics, 49 (2005) 24-33.
2. J.H. Phelps, A.I. Abd El-Rahman, V. Kunc, C.L. Tucker Iii, A model for fiber length attrition in injection-molded long-fiber composites, Composites Part A: Applied Science and Manufacturing, 51 (2013) 11-21.
3. R.S. Bay, C.L. Tucker, Fiber orientation in simple injection moldings. Part II: Experimental results, Polymer Composites, 13 (1992) 332-341.
4. J.H. Phelps, Processing-microstructure models for short-and long-fiber thermoplastic composites, University of Illinois at Urbana-Champaign, 2009.
5. H.J. Wolf, Screw plasticating of discontinuous fiber filled thermoplastic: Mechanisms and prevention of fiber attrition, Polymer Composites, 15 (1994) 375-383.
6. E. Lafranche, P. Krawczak, J.-P. Ciolczyk, J. Maugey, Injection moulding of long glass fiber reinforced polyamide 66: Processing conditions/microstructure/flexural properties relationship, Advances in Polymer Technology, 24 (2005) 114-131.

7. R. Hafellner, M. Pichler, R. Worndle, G. Steinbichler, P. Egger, Injection moulding long fibres-Fibre damage and effect of fibre length on the properties of LFT, Kunststoffe-Plast Europe, 90 (2000) 44-48.
8. R. von Turkovich, L. Erwin, Fiber fracture in reinforced thermoplastic processing, Polymer Engineering & Science, 23 (1983) 743-749.
9. R.A.M. S.L. Villarroel, The effect of the injecion point location on the fiber glass length, Antec, (2007).
10. D. Cianelli, J. Travis, R. Bailey, How to process long-fiber reinforced thermoplastics, Plastics technology, 34 (1988) 84-89.
11. R. Bailey, H. Kraft, A Study of Fibre Attrition in the Processing of Long Fibre Reinforced Thermoplastics, International Polymer Processing, 2 (1987) 94-101.
12. D.L. Krasteva, Integrated prediction of processing and thermomechanical behavior of long fiber thermoplastic composites, (2009).
13. S. Goris, T. Back, A. Yanev, D. Brands, D. Drummer, T.A. Osswald, A novel fiber length measurement technique for discontinuous fiber-reinforced composites: A comparative study with existing methods, Polymer Composites, (2017).
14. V. Kunc, B.J. Frame, B.N. Nguyen, C.L. Tucker III, G. Velez-Garcia, Fiber length distribution measurement for long glass and carbon fiber reinforced injection molded thermoplastics, Proceedings of the 7th Annual SPE Automotive Composites Conference and Exposition, 2007.
15. V. Kunc, B. Frame, J. Pryor, B.N. Nguyen, C.L.T. III, S. Case, D. Penumadu, E.W. Guffey, Techniques and Results for Fiber Length Distribution Determination as a Function of Thickness in Long Fiber Reinforced Injection Molded Thermoplastics, Oak Ridge National Laboratory (ORNL), Tennessee, (2008).
16. A.L. Kabade, D.V. Sangam, Canny edge detection algorithm, International Journal of Advanced Research in Electronics and Communication Engineering (IJARECE), 5 (2016) 1292-1295.
17. J.H. Phelps, A.I.A. El-Rahman, V. Kunc, C.L. Tucker III, A model for fiber length attrition in injection-molded long-fiber composites, Composites Part A: Applied Science and Manufacturing, 51 (2013) 11-21.
18. V. Kunc, B.J. Frame, B.N. Nguyen, C.L. Tucker III, G. Velez-Garcia, Fiber length distribution measurement for long glass and carbon fiber reinforced injection molded thermoplastics, Research Gate, (2007).
19. G. Sebastian, B. Teresa, Y. Angel, B. Dave, D. Dietmar, O.T. A., A novel fiber length measurement technique for discontinuous fiber-reinforced composites: A comparative study with existing methods, Polymer Composites, 0.

Chapter 4 The Use of Flow-Type Dependent Strain Reduction Parameter in Fiber Orientation Predictions

4.1 Abstract

Reliable predictions of fiber orientation profile are important for the improvement of mold design and processing conditions to optimize mechanical performances of the as formed composites. To better reflect slower orientation evolution observed experimentally, various models were developed with a scalar factor α or κ which takes a value between 0 and 1. Normally, this scalar factor is obtained by fitting to orientation data from simple rheological flow. However, in during the mold filling, the flow types including extensional, simple shear, rotational flow and mixed flows, have significant impact on fiber orientation kinetics. This study utilizes a flow-type parameter to locally describe the relative magnitudes of shearing, extension and pure rotation. As a result, a variable strain reduction factor is determined locally by the corresponding local flow-type and used in fiber orientation simulation. The application of the variable strain reduction factor in fiber orientation simulations for both non-lubricated squeeze flow and injection molded center-gated disk, allows the simulated fiber re-orient rate to be dependent on local flow-type. The predicted orientation results show improved qualitative agreement of the profile shape with the experimental data. This empirical variable strain reduction factor might help to improve the fiber orientation predictions especially in complex flow, because it can reflect the different rates at which fibers orient during different flow conditions.

4.2 Introduction

The enhanced demand for lightweight materials in automotive industry has resulted in the increased usage of injection molded discontinuous fiber-reinforced thermoplastics [1]. During the intensive injection molding process, severe fiber breakage arises in the plasticating stage leading to a broad fiber length distribution [2, 3]. Fiber orientation distribution (FOD) is another highly anisotropic feature of the final injection molded parts [4] induced by the complex flow conditions inside the mold including shear, extensional, rotational and mixed flows [5, 6]. The mechanical and other properties can be highly dependent on the orientation distribution [7, 8]. Therefore, it is necessary to obtain accurate fiber orientation predictions for the optimization of various performances of injection-molded parts.

The well-known Jeffery's [9] model describes the motion of fiber in flow with dilute fiber concentration in the absence of fiber-fiber interactions. Folgar and Tucker [10] developed the isotropic rotary diffusion fiber orientation (FT) model for concentrated fiber suspensions. However, it was observed that in shear the prediction using the FT model was much faster than the experimental fiber orientation evolution [11]. Huynh et al. [12] developed the strain reduction factor (SRF) model by straightforwardly scaling the right-hand side of the orientation equation by a factor α $(0 < \alpha < 1)$ to better reflect slower orientation kinetics. Nevertheless, direct scaling of the FT model violates material frame indifference (Objectivity). To achieve an objective orientation equation, Wang [13] developed the improved reduced strain closure (RSC) model. Recently, Phelps et al. [14] further employed the anisotropic rotary diffusion to account for anisotropic fiber interactions.

The empirical parameters in fiber orientation equations need to be determined for orientation prediction purpose. These parameters are typically found by fitting to fiber orientation data in the injection-molded part [15]. Cieslinski et al. [16] obtained the parameters by fitting the models to the fiber orientation evolution during simple rheological flow. Fitting the transient stress response in startup of shear flow to an equation of stress including the contribution from the presence of fibers which is dependent on fiber orientation is another approach to obtain the empirical parameters [17]. For injection-molded parts, optimal values of the empirical parameters can be selected by fitting experimental orientation at a specific region within the parts [18]. However, these procedures might tie the fiber orientation model parameters to specific rheological flow and particular processing conditions. Therefore, a single set of fiber orientation model parameters might fail to fully include the versatile features of fiber motion according to various flow conditions during mold filling process.

Most recently, Lambert et al. [19] suggested that fiber orientation evolution rate in shearing flow deviate quite significantly from that in extensional flow. The fiber orientation evolution was evaluated in both pure shear (in a sliding plate) and pure extension (in a lubricated squeeze flow), and they found that the fitted strain reduction factors from these two flows were significantly different. In continuation of obtaining further understanding toward fiber orientation kinematics according to flow-type, Lambert et al. [20] compared predictions of fiber orientation with experimental results during non-lubricated squeeze. It turned out that both the SRF an RSC models failed to accurately prediction the fiber orientation profile through the entire sample thickness using a constant set of model parameters. The non-lubricated squeeze flow has features of pure shear, pure extensional and the mixture of both flow-types, which might lead to variable fiber reorientation rate according to the local flow kinematics. In this study, we used a flow-type parameter proposed by Astarita et al. [21, 22] to locally describe the relative magnitudes of shearing and extension in a flow. The local strain reduction factor was then interpolated between a typical value for simple shear flow, a value for extensional flow or a value specified for pure rotational flow using a function of this flow-type parameter. The application of a variable strain reduction factor according to flow conditions in fiber orientation simulations shows better qualitative agreement of the profile shape with the experimental data when compared with that using a constant value.

4.3 Fiber Orientation Models

To represent the alignment (orientation) of a rigid particle or fiber, a unit vector, **p**, along the its major axis is customarily used to specify its orientation [23]. The overall fiber orientation state of a fiber suspension can be described by a probability density function, $\psi(\mathbf{p}) = \psi(\phi, \theta)$, which provides a general statistical orientation information in the surface spherical coordinate. To concisely present the fiber orientation state of a fiber suspension, Advani and Tucker [23] proposed to use the second order orientation tensor as:

$$\mathbf{A} = \int \mathbf{pp}\psi(\mathbf{p})\mathrm{d}\mathbf{p}. \tag{4-1}$$

The diagonal components of **A** are the most important ($\mathrm{A}_{11}, \mathrm{A}_{22}$ and A_{33}). They describe the alignment of the population with respect to the axis of the coordinate system. A value of A_{ii} that approaches one indicates alignment in that i direction. Moreover, **A** is symmetric and the trace of $\mathbf{A}$, $\mathrm{A}_{11} + \mathrm{A}_{22} + \mathrm{A}_{33}$, is equal to 1. The fourth order orientation tensor is described as:

$$\mathbf{A_4} = \int \mathbf{pppp}\psi(\mathbf{p})\mathrm{d}\mathbf{p}. \tag{4-2}$$

The evolution equation of $\mathbf{A}$ involves $\mathbf{A_4}$. The $\mathbf{A_4}$ can be approximated in terms of $\mathbf{A}$ using a closure method. In this study, the values of $\mathbf{A_4}$ were evaluated using the so called "invariant-based optimal fitted" (IBOF) closure [24], which was found to give equivalent results when compared to eigenvalue based closures [25].

The classic Folgar-Tucker [10] model includes a phenomenological rotary diffusion term which accounts for fiber interactions. Huynh [12] further modified this model by multiplying its right hand side with a factor α as shown in the following SRF model:

$$\frac{\mathrm{D}\mathbf{A}}{\mathrm{Dt}} = \alpha[\mathbf{W}\cdot\mathbf{A} - \mathbf{A}\cdot\mathbf{W} + \xi[\mathbf{D}\cdot\mathbf{A} + \mathbf{A}\cdot\mathbf{D} - 2\mathbf{D}:\mathbf{A_4}] + 2C_I\dot{\gamma}(\mathbf{I} - 3\mathbf{A})], \tag{4-3}$$

where $\mathbf{I}$ is the unit tensor, $\mathbf{W} = (\nabla\mathbf{v}^t - \nabla\mathbf{v})/2$ is the vorticity tensor and $\mathbf{D} = (\nabla\mathbf{v}^t + \nabla\mathbf{v})/2$ is the rate-of-deformation tensor. The shape factor of an ellipsoid with the aspect ratio, $a_r = \mathrm{length/diameter}$, is defined as $\xi = (a_r^2 - 1)/(a_r^2 + 1)$. There are two empirical parameters in this model: α is the strain reduction factor ranging from 0 to 1 and C_I is the interaction coefficient. However, direct scaling of the FT model violates material frame indifference (Objectivity).

To achieve an objective orientation model, Wang and coworkers [26] proposed the reduced strain closure (RSC) model by only scaling the evolution of the eigenvalues of $\mathbf{A}$:

$$\frac{\mathrm{D}\mathbf{A}}{\mathrm{Dt}} = \mathbf{W}\cdot\mathbf{A} - \mathbf{A}\cdot\mathbf{W} + \xi\{\mathbf{D}\cdot\mathbf{A} + \mathbf{A}\cdot\mathbf{D} - \mathbf{2}[\mathbf{A_4} + (1-\kappa)(\mathbf{L_4} - \mathbf{M_4}:\mathbf{A_4})]:\mathbf{D}\} \\ + 2\mathrm{C_I}\dot{\gamma}(\mathbf{I} - 3\mathbf{A}), \tag{4-4}$$

$$\mathbf{L} = \sum_{i=1}^{3} \lambda_i \boldsymbol{e_i e_i e_i e_i}, \tag{4-5}$$

$$\mathbf{M} = \sum_{i=1}^{3} \boldsymbol{e}_i \boldsymbol{e}_i \boldsymbol{e}_i \boldsymbol{e}_i, \quad (4\text{-}6)$$

where **L** and **M** are 4th order tensors in terms of the eigenvalues, λ_i, and eigenvectors, e_i, of **A**. In Eq.(4-4), κ is the strain reduction factor taking a value between 0 and 1. Both the SRF and RSC models are used in this study.

4.4 Classifier of Flow-Type and Flow-Type Dependent Strain Reduction Factor

In a complex flow, the fluid element experiences pure shearing, elongation, pure rotation or the combination of these cases. During injection molding, all these kinds of flow conditions are existing which have a great impact on fiber orientation kinetics. Specifically, the evolution of fiber orientation in extensional flow is much faster than that in a simple shear flow. In general, the flow condition or flow-type is often thought of as an intrinsic criterion to reflect the fundamental response of fluid element in complex flow. Therefore, it is important to have a mathematical expression or classifier to classify the flow conditions or flow types. The criterion proposed by Astarita [21] was used in this study and is defined as:

$$\beta = \frac{\mathbf{D}:\mathbf{D} + \bar{\mathbf{W}}:\bar{\mathbf{W}}}{\mathbf{D}:\mathbf{D} - \bar{\mathbf{W}}:\bar{\mathbf{W}}} \quad (4\text{-}7)$$

$$\bar{\mathbf{W}} = \mathbf{W} - \boldsymbol{\Omega} \quad (4\text{-}8)$$

$$\boldsymbol{\Omega} = \frac{\mathrm{d}\mathbf{E}}{\mathrm{dt}} \cdot \mathbf{E}. \quad (4\text{-}9)$$

In the definition, $\boldsymbol{\Omega}$ is the rate-of-rotation of the principle directions of **D** and **E** is the matrix of right eigenvectors of **D**. To make an objective flow-type parameter β, $\boldsymbol{\Omega}$ is subtracted from the vorticity tensor **W** as in Eq.(4-8). When the eigenvectors of **D** do not rotate, $\mathbf{\Omega}$ vanishes and $\bar{\mathbf{W}} = \mathbf{W}$. In this study, we assumed $\bar{\mathbf{W}} = \mathbf{W}$ and the codes applying the objective version of β is under development.

The flow-type can be identified by the non-dimensional scalar β. The value of β is 1 in purely extensional flows, 0 in shear flows, and -1 in a pure rotational flows. Values between 1 and 0 indicate a mixture of extension and shear, and values between 0 and -1 indicate mixed shear and rotation. According to the value of β, the local strain reduction factor of orientation model will be interpolated between a typical value of strain reduction factor α_s(or κ_s) for simple shear flow, a value α_e (or κ_e) for extensional flow or a value specified for pure rotational flow. Normally, lower values of α_s and κ_s were used for shear flow according to Ceislinski et al. [4]. While, Lambert and Baird [19] found that a value of strain reduction factor close to 1, can reflect the fast fiber orientation rate during startup of lubricated planar extension flow of a glass fiber reinforced polypropylene suspension. In a following paper, Lambert et al. [20] compared predictions of fiber orientation with experimental results during non-lubricated squeeze flow which includes features of pure shear , pure extensional and the combination of both flow conditions. Predictions using a constant value for strain reduction factor were not capable of describing the fiber orientation state. Specifically, simulations using α_s(orκ_s) only matched well with the experimental data near the wall where shear dominated, while applying a value of 1 for strain reduction factor only fitted the orientation near the center where extension dominated. Therefore, we set the value of α_e or κ_e to be 1, and interpolate the local strain reduction factor from α_s(or κ_s) and α_e (or κ_e) based on the value of β when $0 \leq \beta \leq 1$:

$$\alpha = \beta * 1 + (1 - \beta) * \alpha_s \quad (0 \leq \beta \leq 1) \tag{4-10}$$

$$\kappa = \beta * 1 + (1 - \beta) * \kappa_s \quad (0 \leq \beta \leq 1) \tag{4-11}$$

When $\beta < 0$, the flow has components of rigid body rotation. In rigid body rotation, the deformation is zero or so small it can be neglected [27, 28]. That is to say, the distance between any two given points remains constant with time. The slow down effect for fiber orientation can be ignored for pure rigid body rotation and the original Folgar-Tucker model ($\alpha = 1$ or $\kappa = 1$) can be used to describe fiber motions in such case. Therefore, we also set the strain reduction factor as 1 for the rigid body rotation component. As a result the expressions for the variable strain reduction factors when $-1 \leq \beta \leq 0$ are given as:

$$\alpha = -\beta * 1 + (1 + \beta) * \alpha_s \quad (-1 \leq \beta \leq 0) \tag{4-12}$$

$$\kappa = -\beta * 1 + (1 + \beta) * \kappa_s \quad (-1 \leq \beta \leq 0) \tag{4-13}$$

To sum up, we used the local velocity gradient to evaluate the local flow-type parameter β. Then, a local strain-reduction-factor was calculated using an expression from Eq.(4-10) to Eq.(4-13) according to the range of β and the fiber orientation model chosen. Through this method, a variable strain reduction factor instead of a constant value was used for fiber orientation simulations.

4.5 Experimental

The composites under investigation were 30 wt% glass fibers with a polypropylene matrix. The material was supplied by SABIC Innovative Plastics as 12.5 mm long pellets created through a pultrusion process using 30 wt% formulations.

4.5.1 Non-Lubricated Squeeze Flow

The experimental technique used in the investigation of fiber orientation kinetics in non-lubricated squeeze flow is described in detail by Lambert et al [20]. The samples were prepared by compression molding purge material came out of nozzle of injection molding machine. We followed the same procedure as described in ref. [20] to create a 6.5 mm thick plaque. The plaque was then placed in a rectangular channel mounted on the bottom fixture, and it was compressed by the compression head of the upper fixture. A schematic of the test is shown in Figure 4-1. Both fixtures were mounted on Instron 5969 and the temperature was controlled by an environmental chamber (Instron 3119-609) and maintained at 200 ℃ during the tests . A constant Hencky strain rate, $\dot{\varepsilon} = \dot{H}/H$, of -0.50 s^{-1} was used for all tests.

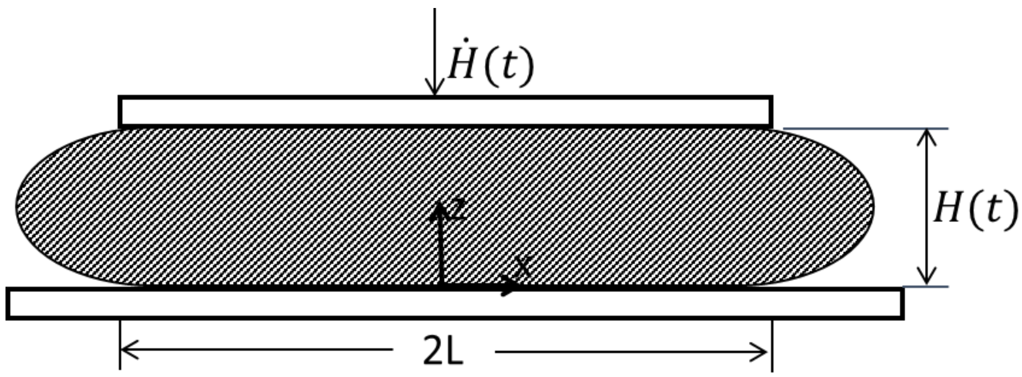

Figure 4-1: Schematic of the non-lubricated squeeze flow experiment. The sample (patterned with upward diagonal lines) is compressed by the top platen with a time-dependent rate of $\dot{H}$. Therefore, the sample thickness, H, is also time-dependent. The fluid flow is symmetric about $x = 0$. The channel has length $2L = 50.8$ mm and an initial thickness.

4.5.2 Injection Molding of Center-Gated Disk

Center-gated-disks were injection-molded from the as-received pellets. The temperature profile in the injection molder (BOY, 35E) was set to 200, 210, 230, 230, and 230 ℃ with a mold temperature of 90 ℃. The mold filling time was about 1 s. The disks made have internal radius $r_{in} = 4$ mm, and an averaged outer radius $r_{out} = 56$ mm. The lengths of the glass fibers in the disks were determined from a burn-off procedure based on that used by Kunc et al [29]. The number average fiber length L_n was 1.14 mm, and the weight average fiber length L_w was 3.41 mm.

4.5.3 Fiber Orientation Characterization

Fiber orientation was measured using the method of ellipses. The desired plane on the sample was polished using metallographic techniques. Fibers intersecting this plane were exposed as ellipses, and their orientation was evaluated based on their minor and major axes. Details of the sample preparation and orientation measurement procedure can be found in Refs [30] and [31]. For the non-lubricated flow test, orientation measurements were taken along the centerline of the samples at $x = L/2$ in the flow direction. While, for the center-gated disk, measurements of fiber orientation on the rz plane were made at a constant thickness-wise positions at the inlet and 60 % of the disk radius.

4.6 Modeling and Simulation of Fiber Orientation

The SRF [Eq.(4-3)] and RSC [Eq.(4-4)] models were used to simulate the fiber orientation evolution. The solutions of velocity profile were obtained from the mass balance and the momentum balance equations:

$$\nabla \cdot \mathbf{v} = 0 \tag{4-14}$$

$$\nabla \cdot (-p\mathbf{I} + 2\eta_s \boldsymbol{D}) = \mathbf{0}, \tag{4-15}$$

where ∇ is the gradient operator, $\mathbf{v}$ the velocity, p the pressure, $\mathbf{I}$ the identity tensor, and η_s the matrix viscosity. The approximate velocity and pressure fields were solved from Eq. (4-14) and Eq. (4-15) for non-lubricated squeeze flow and is described in detail according to Lambert et al. [20]. The approximate velocity were specified as a function of coordinates and time, and the moving upper boundary of the upper platen was incorporated through the arbitrary Lagrangian/Eulerian method [32]. The discontinuous Galerkin finite element method [33] was used to solve fiber orientation models using the specified velocity fields.

For the transient filling simulation of a center-gated disk, the finite element solution was obtained for Eq. (4-14) and Eq. (4-15), and the pseudo-concentration method [34] is additionally used to include the fountain flow effects during mold filling. Therefore three decoupled system of equations are solved at every time step: the flow equations, orientation equations, and a transport equation. In the pseudo-concentration method, air is introduced as a fictitious fluid with zero density and viscosity 0.1% of the filling fluid. A pseudo-concentration variable c is defined to distinguish between the filling fluid and the air. The transport equation that determines the evolution of the variable c takes the form of:

$$\frac{\partial c}{\partial t} + \mathbf{v} \cdot \boldsymbol{\nabla} c = 0. \tag{4-16}$$

The polymer-air interface moves according to this equation and polymer fills the region initially filled with air. A value of $c = 1$ indicates the suspension, a value of $c = 0$ indicates air, and the interface is indicated by a value of $c = 0.5$. The variable c is convected with the fluid velocity $\mathbf{v}$.

For the non-lubricated squeeze flow simulation, parameters of both SRF and RSC models used in the simulation are obtained by Cieslinski et al. [4]. Specifically, α_s was determined to be 0.25 and C_I was determined to be 0.005 by fitting the SRF model to fiber orientation evolution data during startup of simple shear. Following the same procedure, the parameters for the RSC model were determined as: $\kappa_s = 0.2$ and $C_I = 0.005$. For the center-gated disk simulation, we used the same strain reduction factors (α_s and κ_s) as the non-lubricated squeeze flow but with a larger value of C_I, 0.02, which would predict less alignment with the flow direction in steady state compared to C_I of 0.005.

4.7 Results and Discussion

4.7.1 Non-Lubricated Squeeze Flow

The contour plot of the post-calculated flow-type β over half of the symmetric flow domain at a Hencky strain of 1.0 ($t = 2$ s) is shown in Figure 4-2. In the plot, the z axis is the axis of symmetry for this 2D plot. Surrounding the axis of symmetry, the flow-type features extension. The area of the extensional flow domain notably decreases as the x increases, especially in the range of $0 < x < 0.28$. Near the center ($z/H = 0.5$), the flow-type is also extension flow dominated, while at the locations near the wall except those close to the symmetric axis, flow-types feature pure shear flow. These features of the flow-type qualitatively matched well with the approximate solutions of velocity profiles described in detail by Lambert et al. [20].

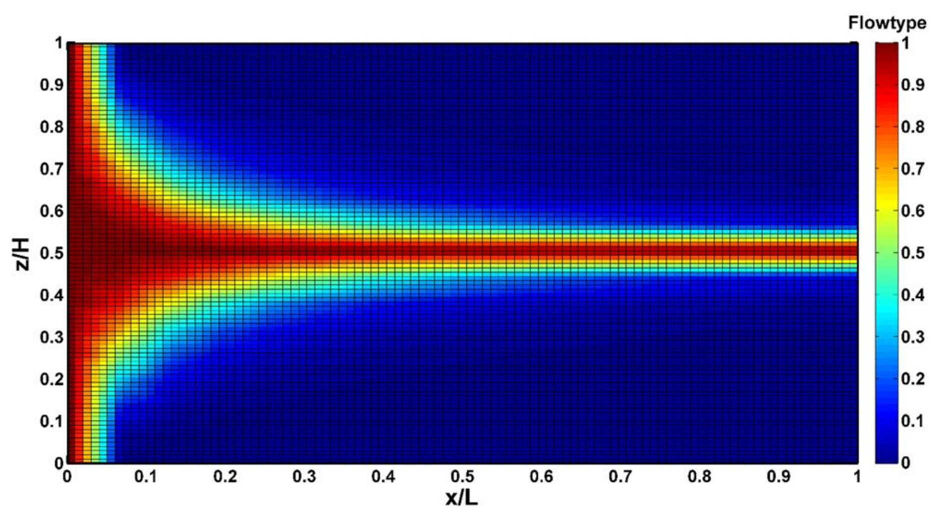

Figure 4-2: Contour plots of flow-type β in half of the symmetric flow domain at a Hencky strain of 1.0 ($t = 2\ s$). Here, the z axis is the axis of symmetry for this 2D plot.

When the local flow-type parameter β is given, the variable strain reduction parameters can be calculated according to Eq.(4-10) and Eq. (4-11), because the non-lubricated flow has no rotational flow component and only contains flow conditions of shear flow, extensional flow, and the mix of both. The values of parameter α along the thickness of the sample at $x = L/2$ and Hencky strain of 1 are shown in Figure 4-3. Here, the value of α_s was set as 0.25 and α_e was 1.0. Near the wall regions ($z/H = 0$ and 1) where shear flow dominates, the values of α are very close to that of α_s. The magnitude of α gradually increases from the wall toward the center, and as approaching the center, the increase turns out to be much more significant and finally α reaches the value of α_e at the center.

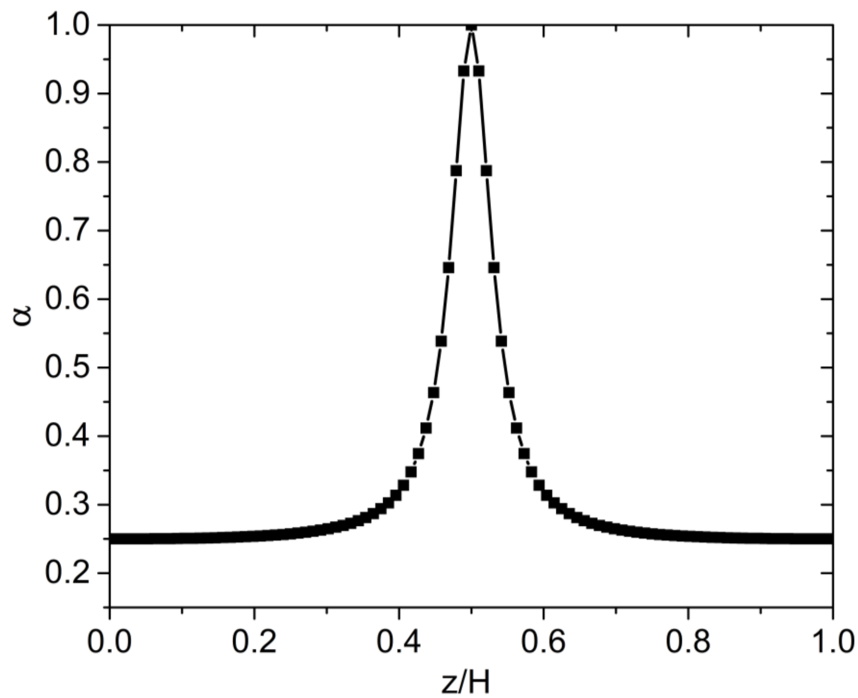

Figure 4-3. Calculated variable strain reduction factor α using equation Eq. (4-10) through the thickness of the sample at $x = L/2$ and Hencky strain of 1. Here, the value of α_s was set to be 0.25 and α_e was 1.0.

To conduct fiber orientation simulations, the initial values of **A** are necessary. The measured initial through-thickness fiber orientation profile at $x = L/2$, is shown in Figure 4-4 and used over the entire domain during simulation. The initial conditions of fiber orientations at the walls ($z/H = 0$ and $z/H = 1$) are specified the same as the measured values at the closest locations. The initial state is close to a planar orientation state, where the fibers are highly aligned toward the y (neutral) direction. The though-thickness fiber orientation profile at the same location after a Hencky strain of 1.0, is shown in Figure 4-5. The fibers evolved into significant flow direction alignment state, as evidenced by the significant increase in A_{xx}. Furthermore, x-direction alignment is stronger toward the center of the samples where extensional flow dominates shear flow.

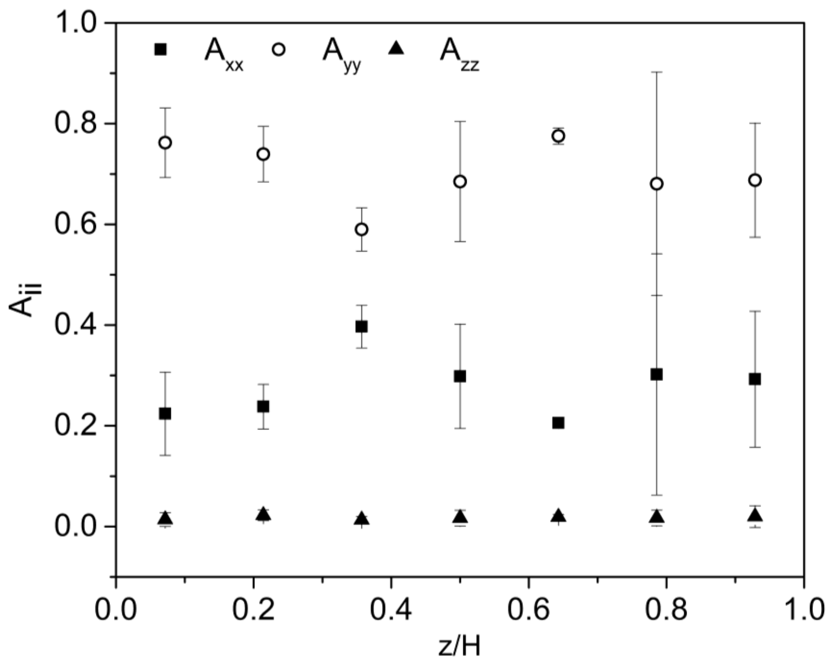

Figure 4-4. The measured initial fiber orientation profile through the entire sample thickness at $x = L/2$ [35]. Here, A_{xx} is the flow direction orientation component, A_{yy} the neutral-direction orientation component, and A_{zz} the thickness-direction orientation component.

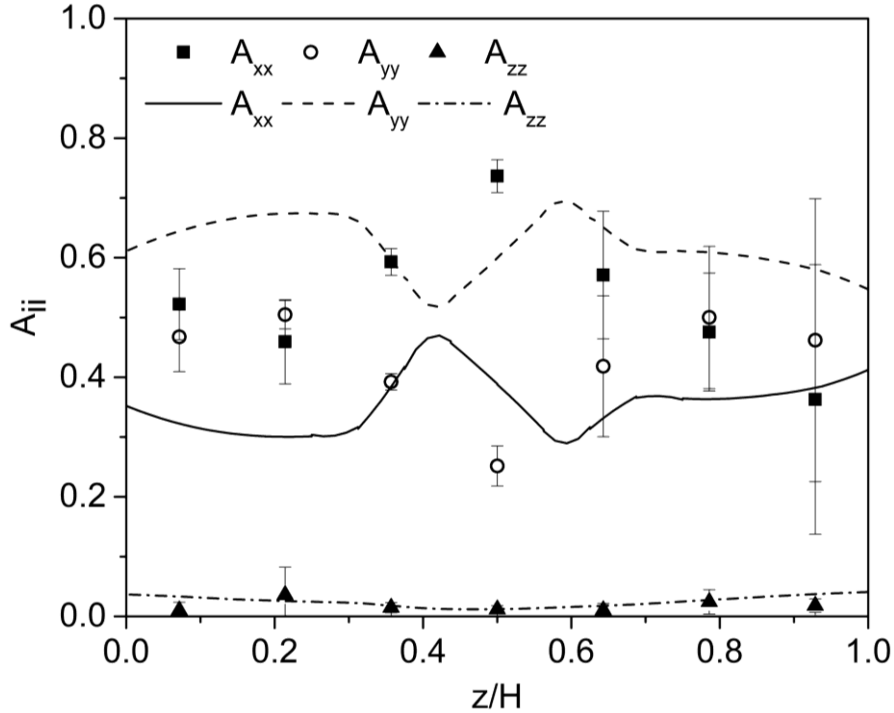

1.0
0.8
0.6
0.4
0.2
0.0
A_ii
0.0
0.2
0.4
0.6
0.8
1.0
z/H
A_xx
A_yy
A_zz
A_xx
A_yy
A_zz

(a)

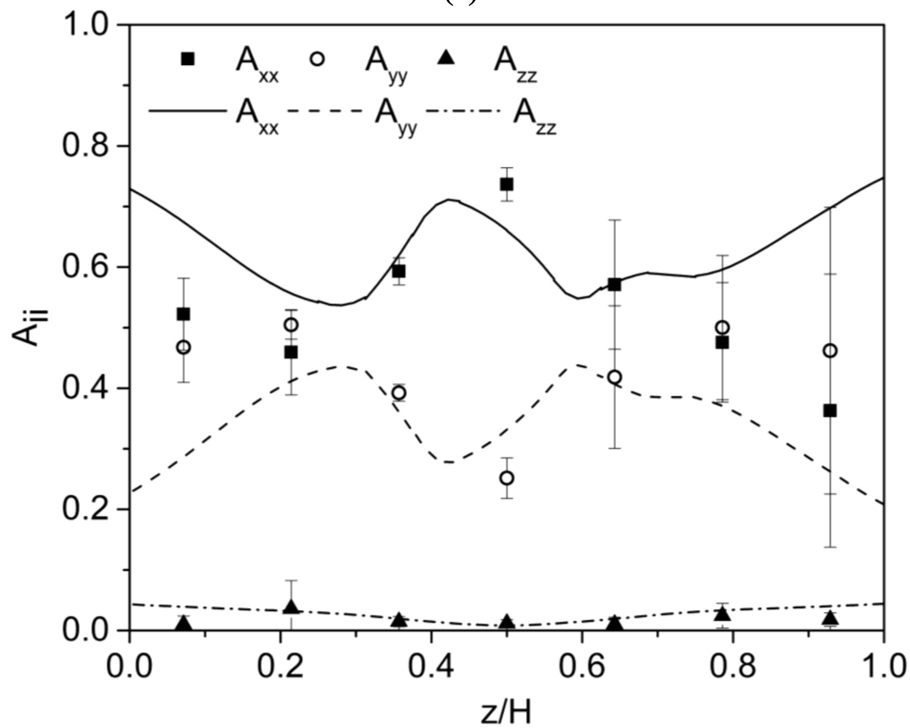

1.0
0.8
0.6
0.4
0.2
0.0
A_ii
0.0
0.2
0.4
0.6
0.8
1.0
z/H
A_xx
A_yy
A_zz
A_xx
A_yy
A_zz

(b)

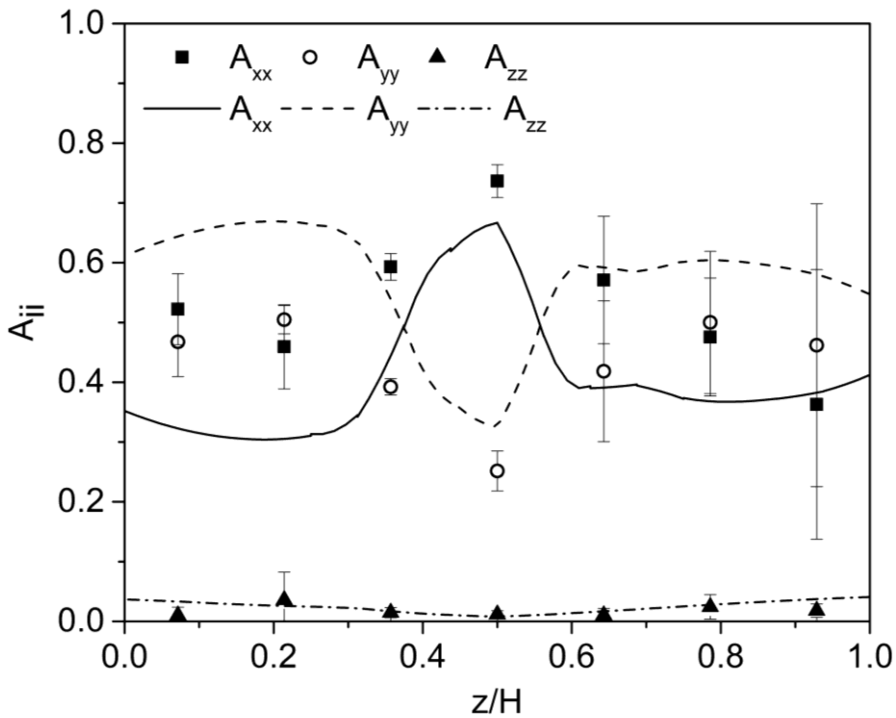

(c)

Figure 4-5. Through-thickness fiber orientation profiles at $x = L/2$ after a Hencky strain of 1.0 at a constant Hencky strain rate of -0.5 s^{-1}. Scatter symbols are measured fiber orientation [35]. Solid lines correspond to predictions from the SRF model using $C_I = 0.005$, with different strain reduction factors: (a) $\alpha_s = 0.25$, (b) $\alpha_e = 1.0$, and (c) a variable α calculated from Eq.(4-10).

All predictions from the SRF model with C_I of 0.005 are shown in Figure 4-5. In Figure 4-5(a), the constant strain reduction factor α_s applied in the model was 0.25. As a result, the SRF model under-predicts A_{xx} and over-predicts A_{yy}, although A_{zz} is well-predicted. In Figure 4-5(b), the constant strain reduction factor α_e applied in the model was 1.0. The predictions better match the fiber orientation profile around $z = H/2$. However, in the shell regions, the predicted values of A_{xx} keep increasing toward the wall, while the values of A_{yy} follow the opposite trend. These features deviate quite significantly from the measured fiber orientation in the shell regions. The predictions from the SRF model using a variable strain reduction factor α as a function of α_s, α_e, and the flow-type parameter β

are shown in Figure 4-5 (c). In the core-region around z = $H/2$, the simulations slightly under-predict A_{xx} and over-predict A_{yy}, but there is a notable improvement when compared to the results of using a constant α_s. At the shell regions (from about $z = 0$ to $z = 0.3H$, and $z = 0.7H$ to $z = H$), the predictions are almost the same as the results of using a constant α_s. This is because the value of the calculated variable α is very close to that of α_s in the shell regions as shown in Figure 4-3. Although the results using a variable α still under-predict A_{xx} and over-predict A_{yy} in the shell regions, the predicted orientation profile show better qualitative agreement of the shape with the experimental data when compared with the predictions using a constant α_e. It seems that the predictions from a variable α is a combination of the features of predictions from the shear parameter α_s and the extensional parameter α_e. The use of a variable α help to adjust fiber orientation rates according to the flow-types and as a result improve the predictions to some extent.

The SRF model violates the requirement of objectivity except when α is 1, so we also conducted simulations using the objective RSC orientation model. Following the same procedure of obtaining the empirical parameters for the non-objective model, Cieslinski et al. [4] determined that κ was 0.20 and C_I was 0.005. With these parameters, the RSC model predicts slightly less flow-direction orientation for most of the through thickness locations and slightly greater flow-direction orientation around $z = 0.84H$ to $z = H$ than the non-objective SRF model, as seen in Figure 4-6 (a). To exclude the possibility that the different predictions is not due to the different values of strain reduction parameters, predictions for the RSC model with the SRF model parameters (i.e., $\kappa = \alpha_s = 0.25$) are also shown in Figure 4-6 (a). With the matched parameters, the RSC model predicts greater flow-direction orientation, especially near the walls (platens). The comparison of A_{xx}

predictions between SRF and RSC models using variable strain reduction factors are also shown in Figure 4-6(b). For SRF mode, the variable α was determined from Eq. (4-10), in which $\alpha_s = 0.25$ and $\alpha_e = 1$. The variable κ of RSC model was calculated from Eq. (4-11), in which the parameters used were $\kappa_e = 1$, and either $\kappa_s = 0.2$ or $\kappa_s = 0.25$. The predictions of the three cases almost overlapped in the core region ($z = 0.31H$ to $z = 0.59H$). While at other locations, the trends are very similar to those using constant strain reduction factors as shown in Figure 4-6 (a).

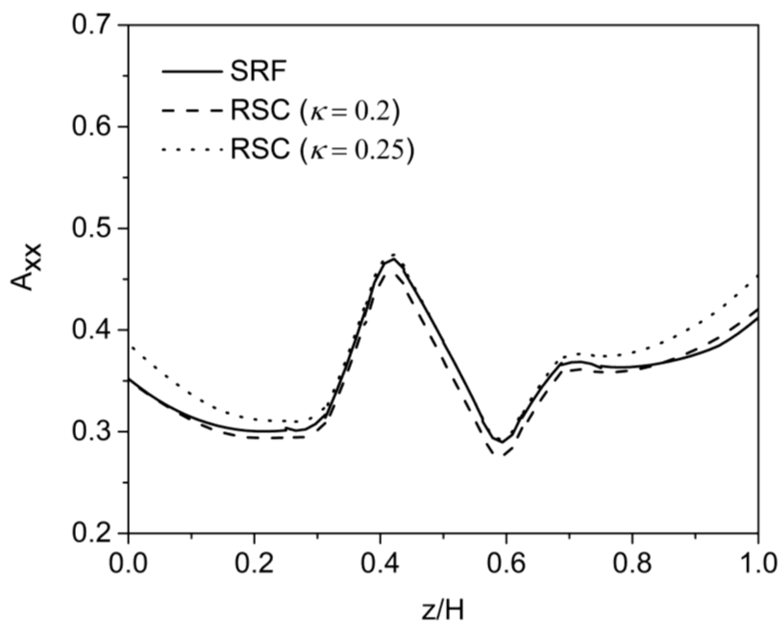

(a)

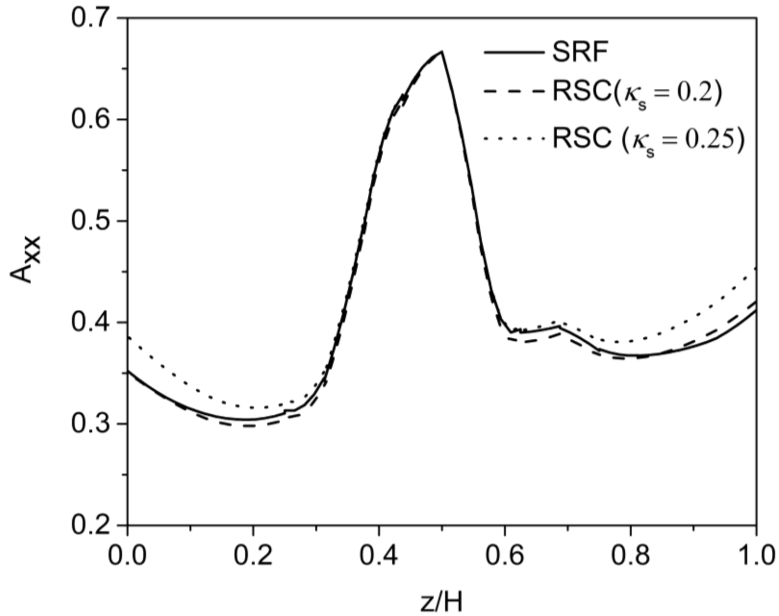

(b)

Figure 4-6. (a) Comparison of A_{xx} predictions between SRF (non-objective, solid line) and RSC (objective, dashed and dotted lines), using constant strain reduction factors. Parameters for the SRF model are $\alpha = 0.25$ and $C_I = 0.005$. Parameters for the RSC model are $C_I = 0.005$ and either $\kappa = \kappa_s = 0.2$ or $\kappa = \alpha_s = 0.25$. (b) Comparison of A_{xx} predictions between SRF (non-objective, solid line) and RSC (objective, dashed and dotted lines), using variable strain reduction factors calculated from Eq. (4-10) or (4-11). Parameters for the SRF model are $\alpha_s = 0.25$, $\alpha_e = 1$ and $C_I = 0.005$. Parameters for the RSC model are $C_I = 0.005$, $\kappa_e = 1$ and either $\kappa_s = 0.2$ or $\kappa_s = \alpha_s = 0.25$.

The NLSF contains flow conditions of shear flow, extensional flow, and the mix of both. It seems that a single set of fiber orientation model parameters failed to capture all the features of the fiber orientation evolution during NLSF. Predictions using parameters obtained from startup of simple shear significantly under-predicted the fiber orientation around $z = H/2$ where extension dominates the flow field. On the other hand, the orientation model without slow-down effect ($\alpha = \alpha_e = 1$), reasonably predicted fiber orientation around the extension-dominated region, but failed to qualitatively capture the orientation profile shape away from there. The value of a variable strain reduction factor based on Eq. (4-10) or (4-11) can be adjusted according to the flow-type. As a result, the prediction near the walls (platens) followed the feature of the prediction of using a constant α_s, and the prediction around $z = H/2$ featured a much faster orientation evolution due to the increased contribution of $\alpha_e = 1$ to the magnitude of the variable α. Although, using a locally variable α still under-predicted the fiber orientation, the predicted orientation results show improved qualitative agreement of the profile shape with the experimental data when compared to those using a constant α. The empirical parameters from the fiber orientation models are dependent on the details of the suspension, for example the fiber length. Obtaining parameters from the startup of simple shear containing a suspension has similar fiber length distribution as the NLSF suspension might improve the predictions.

4.7.2 Center-Gated Disk

The simulation of the filling process of the injection molded center-gated disk started from the inlet of the disk as shown in Figure 4-7. The experimental orientation was obtained at the inlet as shown in Figure 4-8, and specified as the inlet condition during simulation. The initial fiber orientations are asymmetric at the inlet, and varies though the sample thickness. Near the walls, fiber orientation is flow-direction dominated, while the core region has preferential orientation that is transverse to the direction of flow.

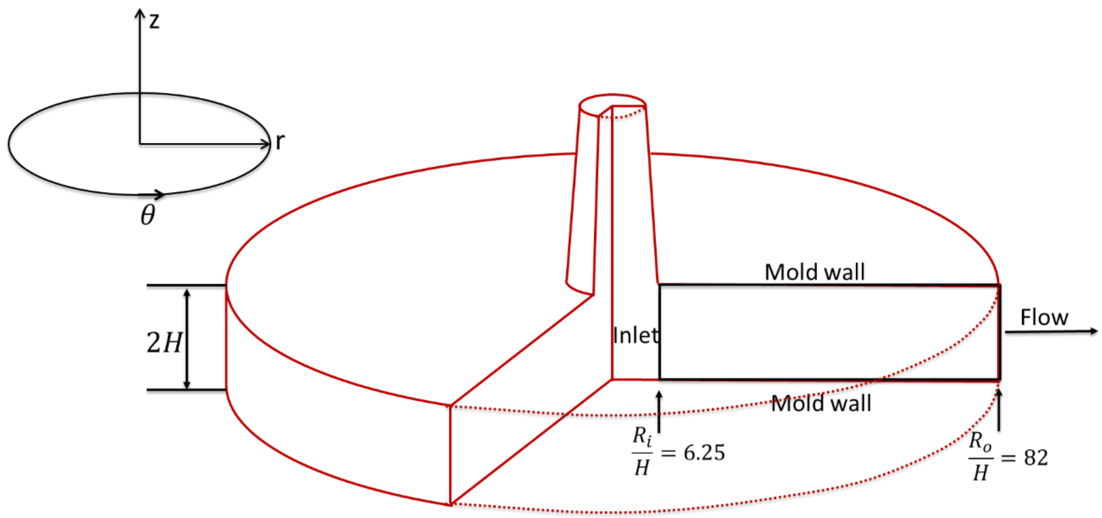

Figure 4-7: Schematic diagram of the CGD geometry with dimensions normalized by the half thickness H of the disk.

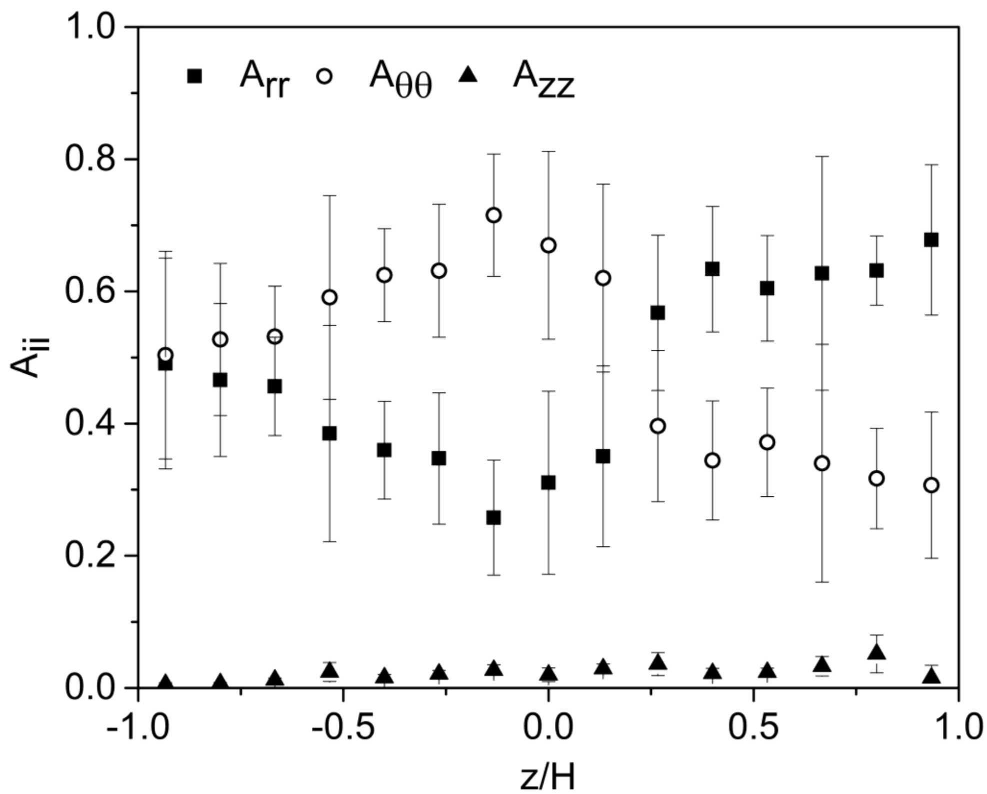

Figure 4-8. Initial fiber orientation state at the inlet of the disk. Here, A_{rr} is the flow direction orientation component, $A_{\theta\theta}$ the neutral-direction orientation component, and A_{zz} the thickness-direction orientation component.

Through thickness A_{rr} profiles at 60% of disk radius are shown in Figure 4-9. Scatter symbols are measured fiber orientation, which shows typical shell-core-shell fiber orientation distribution through the thickness. The predictions of A_{rr} from RSC model using various strain reduction factors are also compared in Figure 4-9. Only A_{rr} component is shown here, but the general trend is similar for $A_{\theta\theta}$ and A_{zz}. All three predictions show the characteristic shell-core-shell layer structures which qualitatively agree with the orientation profile shape through the thickness. Near the walls, there is almost no difference among the predictions from three types of strain reduction factors. This might be because that all the simulations have reached steady-state at the shear flow dominated regions with high shear rate. In the transition regions ($z = -0.77H$ to $-0.1H$ and $z = 0.13H$ to $0.7H$), the model without slow-down effect ($\kappa = \kappa_e$) predict the highest flow-direction alignment. In the same regions, the results from using variable κ and shear flow fitted κ_s are quite comparable, and there is only slight difference around $z = 0.1H$ to $0.3H$ and $z = -0.2H$ to $-0.13H$. Around the center ($z = 0$), compared to the RSC model with the shear flow fitted κ_s, the RSC model with variable κ and the model without slow-down effect ($\kappa = \kappa_e$) predict considerably faster evolution of A_{rr}, where the flow is dominated by extension in the tangential direction.

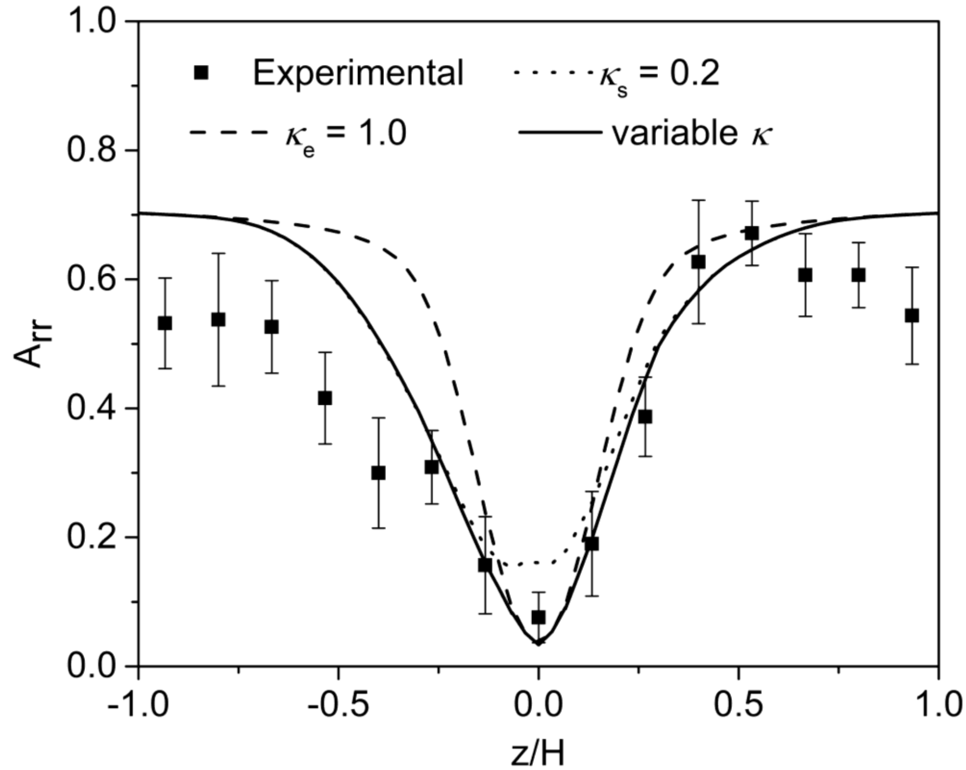

Figure 4-9: Through thickness A_{rr} profile at 60% of disk radius. Scatter symbols are measured fiber orientation. The lines correspond to predictions from the RSC model using a constant strain reduction factor κ_s of 0.2, κ_e of 1.0 and a variable κ based on the local flow-type. All the simulations use the same C_I of 0.02.

At this specific location (60% of disk radius), it seems that using a constant strain reduction factor either of the shear-flow fitted κ_s or the unit κ_e, could not predict the orientation state through the entire thickness of the sample. This might due to the great difference between the observed fiber orientation evolution kinetics during shear and extensional flow. The magnitude of a variable strain reduction factor calculated from Eq. (4-10) to (4-13) can be adjusted according to the flow-type. As a result, at the extensional flow dominated region, the predicted fiber orientation evolution can be much faster than that in the shear flow dominated region. Implicit in this method is that the variable strain reduction factor is empirical, and it is quite dependent on the parameters fitted in pure shear flow and pure extensional flow. But, this method is quite promising, since it allows the simulated orientation evolution rate to be dependent on the local flow conditions.

4.8 Conclusions

A variable strain reduction factor determined from the local flow-type, was used to predict fiber orientation in non-lubricated squeeze flow and the mold filling of injection-molded center-gated disk. The predictions in shear dominated region were close to those using the shear-flow fitted strain reduction factor, while the predictions in extensional dominated region were similar to those using the model excluding orientation slow-down effect (α or $\kappa = 1$). There is a significant difference between the observed fiber orientation evolution rate during pure shear and pure extensional flows, and it seems that fiber orientation model with a constant strain reduction factor were not capable of including all the fiber orientation state in a complex flow field. The variable strain reduction factor allows the simulated orientation evolution rate to be dependent on the local flow conditions. This empirical variable strain reduction factor might help to improve the fiber orientation predictions especially in complex flow. In future, we will continue the test of this method in NLSF with multiple Hencky strains or in injection molded samples tracking the evolution of fiber orientation under multiple time steps, which might help to provide a more conclusive conclusion about this variable strain reduction factor.

References

1. F. Henning, H. Ernst, R. Brüssel, LFTs for automotive applications, Reinforced Plastics, 49 (2005) 24-33.

2. S. Goris, T. Back, A. Yanev, D. Brands, D. Drummer, T.A. Osswald, A novel fiber length measurement technique for discontinuous fiber-reinforced composites: A comparative study with existing methods, Polymer Composites, 0.
3. v.T. Richard, E. Lewis, Fiber fracture in reinforced thermoplastic processing, Polymer Engineering & Science, 23 (1983) 743-749.
4. M.J. Cieslinski, P. Wapperom, D.G. Baird, Fiber orientation evolution in simple shear flow from a repeatable initial fiber orientation, Journal of Non-Newtonian Fluid Mechanics, 237 (2016) 65-75.
5. S.M. Mazahir, G.M. Vélez-García, P. Wapperom, D. Baird, Evolution of fibre orientation in radial direction in a center-gated disk: Experiments and simulation, Composites Part A: Applied Science and Manufacturing, 51 (2013) 108-117.
6. S.M. Mazahir, G.M. Vélez-García, P. Wapperom, D. Baird, Fiber orientation in the frontal region of a center-gated disk: Experiments and simulation, Journal of Non-Newtonian Fluid Mechanics, 216 (2015) 31-44.
7. B.N. Nguyen, S.K. Bapanapalli, J.D. Holbery, M.T. Smith, V. Kunc, B.J. Frame, J.H. Phelps, I. Charles L. Tucker, Fiber Length and Orientation in Long-Fiber Injection-Molded Thermoplastics — Part I: Modeling of Microstructure and Elastic Properties, Journal of Composite Materials, 42 (2008) 1003-1029.
8. H. Chen, D. Baird, Prediction of Young's Modulus for Injection Molded Long Fiber Reinforced Thermoplastics, Journal of Composites Science, 2 (2018) 47.
9. G.B. Jeffery, The motion of ellipsoidal particles immersed in a viscous fluid, Proc. R. Soc. Lond. A, 102 (1922) 161-179.
10. F. Folgar, C.L. Tucker III, Orientation behavior of fibers in concentrated suspensions, Journal of reinforced plastics and composites, 3 (1984) 98-119.
11. M. Sepehr, G. Ausias, P.J. Carreau, Rheological properties of short fiber filled polypropylene in transient shear flow, Journal of Non-Newtonian Fluid Mechanics, 123 (2004) 19-32.
12. H.M. Huynh, Improved fiber orientation predictions for injection-molded composites, University of Illinois at Urbana-Champaign, 2001.
13. J. Wang, Improved fiber orientation predictions for injection molded composites, ProQuest, 2007.
14. J.H. Phelps, C.L. Tucker III, An anisotropic rotary diffusion model for fiber orientation in short-and long-fiber thermoplastics, Journal of Non-Newtonian Fluid Mechanics, 156 (2009) 165-176.
15. J.H. Phelps, C.L. Tucker, An anisotropic rotary diffusion model for fiber orientation in short-and long-fiber thermoplastics, Journal of Non-Newtonian Fluid Mechanics, 156 (2009) 165-176.
16. M.J. Cieslinski, D.G. Baird, P. Wapperom, Obtaining repeatable initial fiber orientation for the transient rheology of fiber suspensions in simple shear flow, J. Rheol., 60 (2016) 161-174.
17. K. Ortman, D. Baird, P. Wapperom, A. Whittington, Using startup of steady shear flow in a sliding plate rheometer to determine material parameters for the purpose of predicting long fiber orientation, J. Rheol., 56 (2012) 955-981.
18. R.S. Bay, Fiber orientation in injection-molded composites: a comparison of theory and experiment, University of Illinois at Urbana-Champaign, 1991.

19. G.M. Lambert, D.G. Baird, Evaluating rigid and semiflexible fiber orientation evolution models in simple flows, Journal of Manufacturing Science and Engineering, 139 (2017) 031012.
20. G. Lambert, P. Wapperom, D. Baird, Obtaining short-fiber orientation model parameters using non-lubricated squeeze flow, Physics of Fluids, 29 (2017) 121608.
21. G. Astarita, Objective and generally applicable criteria for flow classification, Journal of Non-Newtonian Fluid Mechanics, 6 (1979) 69-76.
22. F.R. Phelan, S.D. Hudson, M.D. Handler, Fluid dynamics analysis of channel flow geometries for materials characterization in microfluidic devices, Rheologica Acta, 45 (2005) 59-71.
23. S.G. Advani, C.L. Tucker, The use of tensors to describe and predict fiber orientation in short fiber composites, J. Rheol., 31 (1987) 751-784.
24. D.H. Chung, T.H. Kwon, Invariant-based optimal fitting closure approximation for the numerical prediction of flow-induced fiber orientation, J. Rheol., 46 (2002) 169-194.
25. D.H. Chung, T.H. Kwon, Improved model of orthotropic closure approximation for flow induced fiber orientation, Polymer Composites, 22 (2001) 636-649.
26. J. Wang, J.F. O'Gara, C.L. Tucker III, An objective model for slow orientation kinetics in concentrated fiber suspensions: Theory and rheological evidence, J. Rheol., 52 (2008) 1179-1200.
27. P. De Gennes, Coil-stretch transition of dilute flexible polymers under ultrahigh velocity gradients, The Journal of Chemical Physics, 60 (1974) 5030-5042.
28. J.L. Lumley, Drag reduction by additives, Annual review of fluid mechanics, 1 (1969) 367-384.
29. V. Kunc, B.J. Frame, B.N. Nguyen, C.L. Tucker III, G. Velez-Garcia, Fiber length distribution measurement for long glass and carbon fiber reinforced injection molded thermoplastics, Research Gate, (2007).
30. G.M. Vélez-García, P. Wapperom, V. Kunc, D. Baird, A. ZINK-SHARP, Sample preparation and image acquisition using optical-reflective microscopy in the measurement of fiber orientation in thermoplastic composites, Journal of microscopy, 248 (2012) 23-33.
31. G.M. Vélez-García, P. Wapperom, D.G. Baird, A.O. Aning, V. Kunc, Unambiguous orientation in short fiber composites over small sampling area in a center-gated disk, Composites Part A: Applied Science and Manufacturing, 43 (2012) 104-113.
32. T.J. Hughes, W.K. Liu, T.K. Zimmermann, Lagrangian-Eulerian finite element formulation for incompressible viscous flows, Computer methods in applied mechanics and engineering, 29 (1981) 329-349.
33. P. Lasaint, P.-A. Raviart, On a finite element method for solving the neutron transport equation, Mathematical aspects of finite elements in partial differential equations, Elsevier, 1974, pp. 89-123.
34. G. Haagh, F. Van De Vosse, Simulation of three-dimensional polymer mould filling processes using a pseudo-concentration method, International Journal for Numerical Methods in Fluids, 28 (1998) 1355-1369.
35. G. Lambert, Using non-lubricated squeeze flow to obtain empirical parameters for modeling the injection molding of long-fiber composites, Virginia Tech, (2018).

Chapter 5 Prediction of Young's Modulus for Injection Molded Long Fiber Reinforced Thermoplastics

5.1 Abstract

In this article, the elastic properties of long-fiber injection-molded thermoplastics (LFTs) are investigated by micro-mechanical approaches including the Halpin-Tsai (HT) model and the Mori-Tanaka model based on Eshelby's equivalent inclusion (EMT). In the modeling, the elastic properties are calculated by the fiber content, the fiber length and the fiber orientation. Several closure approximations for the fourth-order fiber orientation tensor are evaluated by comparing the as-calculated elastic stiffness with that from the original experimental fourth-order tensor. An empirical model was developed to correct the fibers' aspect ratio in the computation for the actual as-formed LFTs with fiber bundles under high fiber content. After the correction, the analytical predictions had good agreement with the experimental stiffness values from tensile tests on the LFTs. Our analysis shows that it is essential to incorporate the effect of the presence of fiber bundles to accurately predict the composite properties. This work involved the use of experimental values of fiber orientation and serves as the basis for computing part stiffness as a function of mold filling conditions. The work also explains why the modulus tends to level off with fiber concentration.

5.2 Introduction

During the last decade, an enhanced demand for lightweight materials in automotive applications has resulted in the growth of the use of thermoplastic-discontinuous fiber composites [1]. The increased growth of the use of these thermoplastic matrix composite systems is due to the combination of mechanical properties and melt processability. long-fiber (> 1 mm) injection-molded thermoplastics (LFTs) possess better mechanical properties over short fiber (< 1 mm) composites while retaining their ability to be injection molded [2]. The goal of this research is to improve the stiffness properties predictions for injection molded LFTs. During the plasticating stage of injection molding, significant fiber attrition will occur leading to a broad fiber length distribution (FLD) [3]. Fiber orientation distribution (FOD) is another highly anisotropic feature of the final injection molded parts induced by the mold filling process [4]. Mechanical properties of LFTs are highly dependent on these microstructural variables imparted by the injection molding process [5].

The computation of the elastic stiffness for the aligned and monodispersed short fiber composites was well studied by a large range of people. Tucker et al. [6] reviewed the micromechanical models for this type of composite. By comparing the standard micromechanical models with their finite element method, the authors have shown that the Halpin-Tsai equation gives reasonable estimates for stiffness, but the best predictions come from the Mori-Tanaka model based on the Eshelby's equivalent inclusion method. A similar conclusion was reached by Hine[7]. Ingber and Papathanasiou[8] found the variant of the Halpin-Tsai model is in very good agreement with their boundary element method (numerical simulation) for their entire range of fiber volume contents and aspect ratios, although they had no experimental data for comparison. These models for aligned and monodispersed fiber composites can predict the properties of a representative volume element that can subsequently be averaged to include effects of fiber length and orientation distributions of a real injection molded material. Hine et al.[7] carried out numerical simulation using a distribution of fiber lengths generated by the Monte-Carlo technique. Garesci et al.[5] applied the fitted probability density function to get the averaged property from each single fiber length. A relatively concise way is to replace the FLD with some sort of mean fiber length [7, 9, 10]. The most widely used orientation-averaging scheme is to use second and/or fourth order orientation tensors developed by Tucker and Advani [4] to average the property constants. Hine et al.[11] have shown that the results determined by the constant strain orientation averaging method (assuming the units have the same strain and average their stiffness constants) were in good agreement with their numerical simulations. There exists very little modeling work for predicting stiffness properties on injection molded LFTs [5]. The scenario of the LFTs is different from the works that studied short fiber composite. LFTs injection molding pellets prepared by the pultrusion technique have received much attention. In particular, the fibers are in the form of aligned fiber bundles coated by thermoplastic matrix, which produces pellets with much higher fiber contents than those of more conventional 'short-fiber' compounds. During the compounding process, filamentization of fiber bundles and fracture of the resultant monofilaments into elements of a lower aspect ratio lead to the dispersion of fibers into the polymer matrix [12]. For high content fiber composites, the presence of fiber bundles seems to be unavoidable which could result in a reinforcement with a much lower aspect ratio and effective stiffness than well-dispersed fibers, consequently giving a lower and even decreasing stiffness [13]. However, the existing stiffness models assume the fibers are fully and evenly dispersed in the matrix. The predicted values keep increasing with the fiber content, which is not true within commercial fiber concentration for injection molded

LFTs [13, 14]. In this paper, we report on the development of an empirical model to correct the fibers' aspect ratio for the actual as-formed LFTs with fiber bundles under high fiber content. After the correction, the analytical predictions show good agreement with the experimental stiffness values from tensile tests on the LFTs for the whole fiber contents range investigated. Our analysis shows that it is essential to incorporate the effect of the presence of fiber bundles to accurately predict the composite properties.

5.3 Analytical Modeling Details

5.3.1 Orientation Tensor

A single rigid fiber can be represented by a unit vector, $\mathbf{p}$, parallel to the fiber's long axis. The average orientation state of a fiber composite can be descried by even-ordered structural tensors [4]. In this study, the second and fourth order orientation used in the modeling are defined as:

$$\mathbf{A} = \langle \mathbf{pp} \rangle = \int \mathbf{pp}\psi(\mathbf{p})\, \mathrm{d}\mathbf{p}, \tag{5-1}$$

$$\mathbf{A_4} = \langle \mathbf{pppp} \rangle = \int \mathbf{pppp}\psi(\mathbf{p})\, \mathrm{d}\mathbf{p}. \tag{5-2}$$

Where $\psi(\mathbf{p})$ is the probability distribution function for orientation, and the bracket '< >'denotes the average quantity over a volume domain. The second order orientation tensor, $\mathbf{A}$, can be measured, while the fourth order orientation tensor, $\mathbf{A_4}$, can either be obtained from experiments or estimated in terms of $\mathbf{A}$ using various closure approximation methods [4]. In this study, several approximation closures are implemented to calculate $\mathbf{A_4}$, and the stiffness results evaluated from these approximations are compared with that obtained from the experimentally measured $\mathbf{A_4}$.

5.3.2 Fiber Length Description

Due to the compounding process, the injection molded LFTs will end up with a very broad fiber length distribution. The actual fiber length information can be described by the experimentally obtained probability of finding a fiber with length l_i given by:

$$pl(l_i) = \frac{N_i}{\sum N_i}. \tag{5-3}$$

Here, N_i is the measured number of fibers with length l_i. A more concise approach is to replace the FLD with a single length, normally the number or weight average length defined, respectively, as:

$$L_n = \frac{\sum N_i \, l_i}{\sum N_i} \tag{5-4}$$

$$L_w = \frac{\sum N_i \, l_i^2}{\sum N_i l_i}. \tag{5-5}$$

5.3.3 Elastic Properties

As mentioned in the introduction, both the Halpin-Tsai (HT) and Eshelby-Mori-Tanaka (EMT) methods are extensively studied for the unidirectional or short fiber reinforced composites. The Halpin-Tsai method is the most widely used micromechanical model because of its ease of implementation [15, 16]. The corresponding equations are derived from the self-consistent ideas of Hill [17] and the final implementation is semi-empirical in nature. Several authors have concluded that a constant strain assumption works better than the constant stress assumption, that is to say, stiffness averaging surpasses the compliance averaging in the computation [11, 18]. So in this article, the HT equations are used to predict the compliance matrix, and then the stiffness matrix is obtained from the inverse of the compliance matrix. Finally, the material property is calculated from averaging the stiffness constants based on FLD and FOD.

In this study, the EMT method is also used and compared with the HT method. The EMT method is a combination of Eshelby's equivalent inclusion method and Mori-Tanaka's back stress analysis and so this model is valid even for large volume fraction of fibers. In particular, the equivalent inclusion method of Eshelby is applied in the computation of energy-release rate in terms of the equivalent eigenstrains defined in the fiber and crack [19]. As a result, the EMT method provides the overall stiffness of the composite weakened by fiber-end cracks.

To include the FLD effect on the elastic properties, we use the EMT or HT method to calculate the stiffness matrix component C_{ijkl} of a ‘reference’ unidirectional fiber composite using either the experimental fiber length probability $pl(l_i)$:

$$C_{ijkl} = \frac{\sum C^{*}_{ijkl}(l_i/d) \ * pl(l_i)}{\sum pl(l_i)} \tag{5-6}$$

or using an average fiber length L_{avg} (L_n or L_w) evaluated from the FLD:

$$C_{ijkl} = C^{*}_{ijkl}(L_{avg}/d) \tag{5-7}$$

Here C^{*}_{ijkl} is the stiffness matrix component having a specific fiber aspect ratio l_i/d or L_{avg}/d, and d is the single fiber diameter.

To get the stiffness of the actual injection molded LFTs, a mean tensor averaging procedure is used [20]. Specifically, the stiffness of the calculated unidirectional fiber composite including the FLD effect is averaged over the as-formed fiber orientation state as follow:

$$\begin{aligned} \bar{C}_{ijkl} = {} & B_1 A_{ijkl} + B_2\left(A_{ij}\delta_{kl} + A_{ij}\delta_{kl}\right) + B_3\left(A_{ik}\delta_{jl} + A_{il}\delta_{jk} + A_{jl}\delta_{ik} + A_{jk}\delta_{il}\right) \\ & + B_4\delta_{ij}\delta_{kl} + +B_5\left(\delta_{ik}\delta_{jl} + \delta_{il}\delta_{jk}\right) \end{aligned} \tag{5-8}$$

where δ_{ij} denotes the Kronecker delta and the scalar parameters B_i ($i = 1\ to\ 5$) are the invariants of the stiffness tensor of the calculated unidirectional fiber composite given as:

$$\begin{aligned} B_1 &= C_{11} + C_{22} - 2 * C_{12} - 4 * C_{66} \\ B_2 &= C_{12} - C_{23} \\ B_3 &= C_{66} + \frac{1}{2}(C_{ijkl} - C_{22}) \\ B_4 &= C_{23} \\ B_5 &= \frac{1}{2}(C_{22} - C_{23}) \end{aligned} \quad (5\text{-}9)$$

Here, C_{ij} is the contracted notion for the 4th order stiffness matrix. The composite specimen can be considered as a stacking sequence of thin layers which might have a different fiber orientation state. The stiffness of each layer is calculated based on the overall FLD and the characterized orientation state using the above mentioned method. Finally, the classical lamination theory [21] is then applied to calculate the overall effective engineering stiffness of the composite [20].

5.4 Materials and Methods

The composites under investigation were 10, 30, 40 and 50 wt% glass fibers with a polypropylene matrix. The material was supplied by SABIC Innovative Plastics (Ottawa, Illinois, the US) as 12.5 mm long pellets created through a pultrusion process in 30 and 50 wt% formulations. Samples with 10 wt% fibers were created by diluting the 30 wt% pellets with neat polypropylene, while 30 and 50 wt% pellets were put together to create the 40 wt% composites. The pellets contain a unidirectional bundle of fibers that must be dispersed during the injection molding process, specifically in the plasticating unit. Center-gated disk geometries were formed by injection molding as shown in Figure 5-1. In this study, the Hele-Shaw region (60% disk radius) and the advancing front region (85% disk radius) were investigated for fiber length, fiber orientation and mechanical properties. Tensile specimens were cut from the injection-molded samples and the young's modulus was measured according to ASTM D3039 [22] for polymer matrix composite materials.

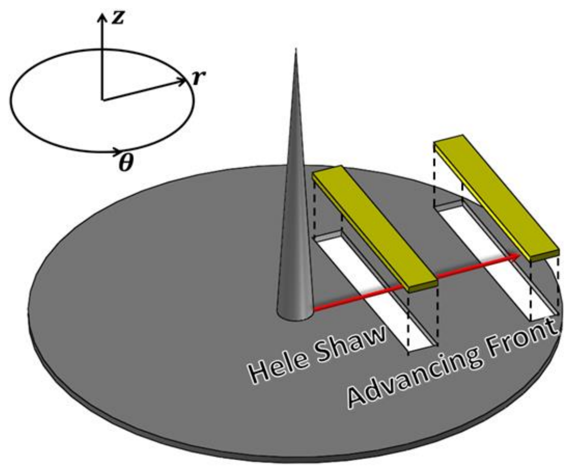

Figure 5-1: The injection-molded glass/pp center-gated disk: the Hele-Shaw region (60% disk radius) and advancing front region (85% disk radius) were investigated in this study.

For fiber length measurement, a method based on Ref. [23] was modified as follows: instead of directly injecting epoxy into the samples after the burning off of the polymer matrix, a needle coated with epoxy was inserted into the sample all the way through the thickness direction shown in Figure 5-2 (a) . As a result, fibers at this location were collected by the epoxy on the needle as shown in Figure 5-2 (b). Due to this sampling method there was biased toward longer fibers, and the measured fiber length was then corrected based on the length of each fiber and the diameter of the needle with epoxy coating. The needle with the fibers was re-burned to get rid of the epoxy. Loose glass fibers were then dispersed on an office scanner and imaged at 3200 dpi. At least 3000 fibers of each sample were measured using our in-house developed Matlab® codes. The fiber length distribution showed the typical log-normal distribution commonly observed for fiber composites. Three repeated measurements were carried out to to produce the averages in

Table 5-1. The number average (L_n) and weight average (L_w) fiber lengths were calculated according to Eqs. (5-4) and (5-5), respectively. It can be seen that the average fiber lengths in these samples are reduced with increasing fiber content.

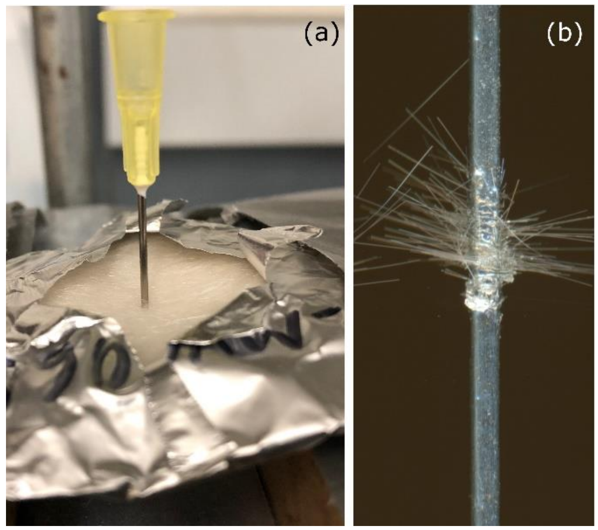

Figure 5-2: The modified fibers sampling method: (a) a needle coated with epoxy inserted into the desired location, and (b) the pulled out needle with the fibers attached on the surface of the epoxy.

Table 5-1: Fiber lengths information.

Fiber content	Hele-shaw region		Advancing-front region	
	L_n (mm)	L_w (mm)	L_n (mm)	L_w (mm)
10 wt% (v_f=0.0 38)	1.51±0.081	3.59±0.71	1.76±0.12	3.21±0.37
30 wt % (v_f=0.135)	1.14±0.078	3.41±0.41	1.32±0.063	3.52±0.26
40 wt% (v_f=0.197)	0.98±0.080	2.67±0.28	1.03±0.086	2.81±0.35
50 wt% (v_f=0.268)	0.87±0.061	2.42±0.32	0.882±0.062	2.54±0.21

Fiber orientation were measured to gain insight into its relationship to the stiffness performance at the same locations. Orientation measurements were taken along the $r-z$plane, such that r denotes the flow direction with the velocity gradient in z. Samples were polished using modified metallographic techniques and oxygen plasma etched to enhance the contrast of the glass fiber and polypropylene matrix. Details of the sample preparation and orientation measurement procedure can be found in the Ref. [24] and [25]. Figure 5-3 shows the measured through thickness fiber orientation for various glass fiber concentrations at the Hele-Shaw region. For the fiber orientation tensor, **A**, the diagonal components are the most important. They describe the alignment of the population with respect to the axis of the coordinate system. A value that approaches one indicates increased alignment in that direction. Only the θ direction component is presented here, because the young's modulus was measured along this transverse direction. At 30, 40, and 50 wt%, the through thickness fiber orientation distributions are very similar showing the characteristic shell-core-shell layer structures. Generally, the θ direction component reaches its largest value near the center of the disk, because that the center of the disk is dominated by extensional flow in this tangential direction. However, at 10 wt%, the distribution deviates significantly from the rest. The through thickness fiber orientation distribution is relatively 'flat' compared to those with higher fiber concentrations. This might due to the concentration effects on the fiber orientation dynamics. At 10 wt%, the degree of fiber-fiber interaction is much less, that is to say hindrance to fiber alignment is much less, as a result the tangential direction alignment is quite dominant.

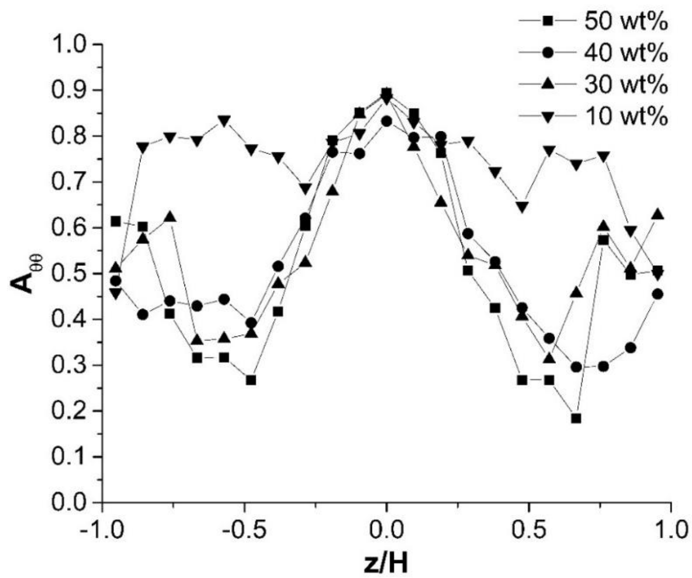

Figure 5-3: Measured θ direction fiber orientation distributions through the thickness direction for 10, 30, 40 and 50 wt% glass fiber at the hele-shaw region.

5.5 Results and Discussion

In all the calculations in this article, the measured FLD or the corresponding average fiber length (L_n or L_w) was input into Eqs. (5-6) or (5-7), while the experimental second-order tensors were used in Eqs. (5-8). To analyze the accuracy of various closure approximations for predicting the elastic properties, the fourth order orientation tensors were evaluated by the linear (LIN), quadratic (QUA), hybrid (HYB), Invariant-based optimal fitting (IBOF) and improved orthotropic (ORW3) closure approximations [4, 18, 26, 27]. Then, the as calculated elastic stiffness using each of these estimated fourth order tensors was compared with that using the original experimental 'true' fourth-order tensor (TRU) obtained from Eqs. (5-2). The comparisons of the effective engineering modulus along the tangential direction are presented in Figure 5-4 and Figure 5-5 applying the methods of EMT and HT, respectively. The predicted results and the general pattern with the HT and EMT methods in the studied fiber content range are very similar. Both models show a similar linear increase in the transverse modulus with increasing fiber content. However, all the values calculated from the EMT model, no matter what length parameter and closure approximation are considered, are slightly greater than those from the HT model. Moreover, the differences between the two methods become more notable as fiber content increases. In Tucker and Liang's [6] review of the stiffness predictions for unidirectional fiber composites, for composites with an aspect ratio larger than 10, the EMT also has predicted greater values of the dominant modulus than the HT model. To answer the question which closure method or methods are the best for stiffness prediction purposes, the results calculated using the experimental fourth order orientation tensors are used as criteria. It seems that, for the entire fiber content range and all the scenarios using different fiber length parameters (FLD, L_n and L_w), the magnitudes of IBOF and ORW3 predictions are the most comparable to the criteria. Another aspect of this paper is to examine the effects of the length parameters (FLD, L_n and L_w) on the stiffness predictions for injection molded LFTs. It is seen that, the predictions of the L_n parameters lie between the largest values generated by the L_w parameters and the smallest predictions from the measured FLD. This result indicates that, for the purpose of replacing the FLD by an average fiber length in the computation, the L_n might outperform the L_w in terms of generating a better match with the FLD.

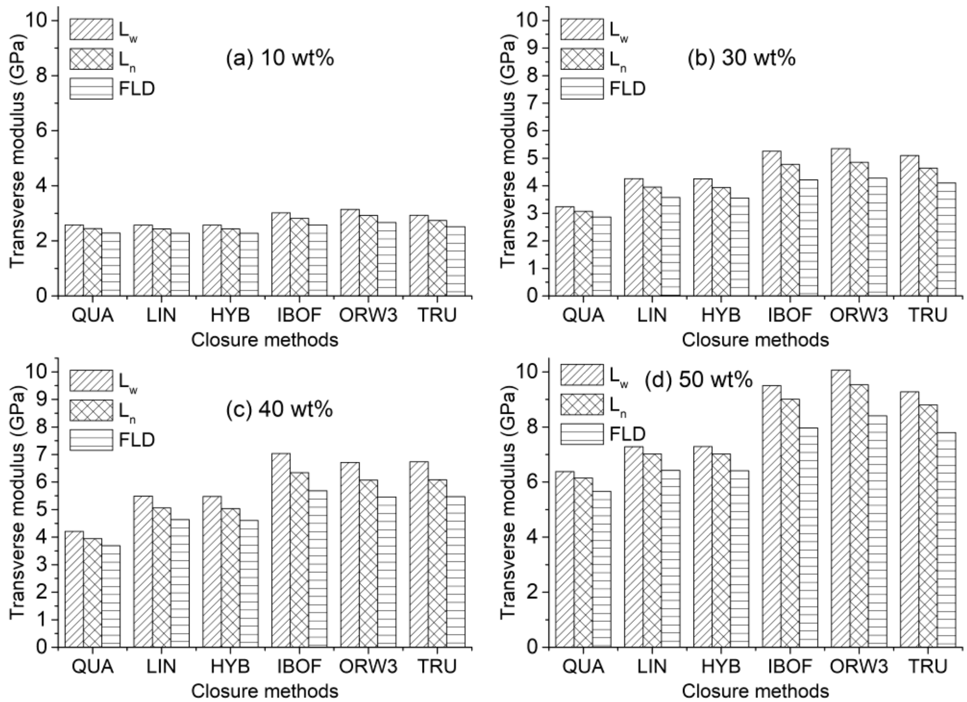

Figure 5-4: Predicted transverse modulus at the hele-shaw region using EMT model for (a) 10 wt%, (b) 30 wt%, (c) 40 wt% and (d) 50 wt% glass fiber polypropylene composites. Various closure approximations and length parameters were used in the calculations.

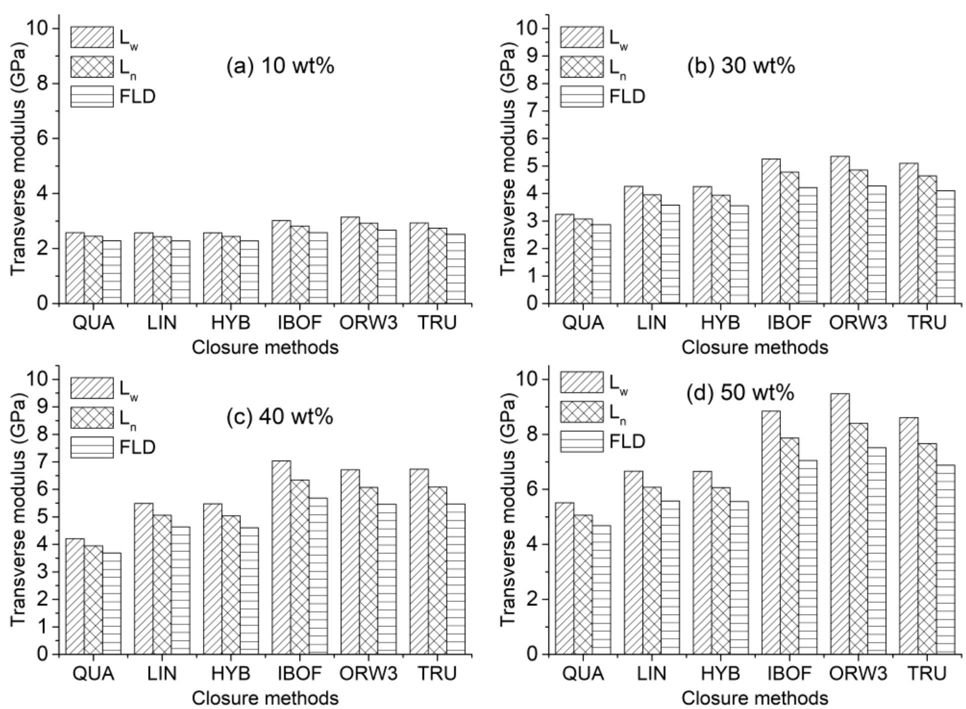

Figure 5-5: Predicted transverse modulus at the hele-shaw region using HT model for (a) 10 wt%, (b) 30 wt%, (c) 40 wt% and (d) 50 wt% glass fiber polypropylene composites. Various closure approximations and length parameters were used in the calculations.

The predictions are also compared with the transverse (θ direction) tensile test results shown in Figure 5-6. At most locations through the thickness, the fibers are predominantly oriented toward this direction as shown in Figure 5-3. Here, both HT and EMT models are applied with the measured FLD and experimental fourth order orientation tensor. Only at the lowest 10 wt% ($v_f = 0.0385$) fiber concentration do the predictions match well with the experimental results. As concentration increases, the deviations of the predictions from the experimental data turn out to be more significant. Several authors [13, 28] experimentally observed that any incremental increase in fiber content appears to bring a lower improvement in properties than the previous one. That is to say, the mechanical performance of the injection molded LFTs will reach a plateau or even decrease at very high fiber concentration range. There are several possible reasons for the degradation of the mechanical properties. First, due to the non-homogeneous nature of these materials, problems can arise during their manufacture, which result in void content/porosity in the final parts [29]. Second, there is also a possibility of poor adhesion between the glass fibers and the matrix [30]. Finally, at higher fiber content, fiber bundles are very common in the injection molded LFTs [13]. There are two major effects of the presence of fiber bundles on the mechanical performance of the composites. First, the clumping of fibers will reduce the effective fiber aspect ratios in the reinforcement. Second, fiber bundles have effect on stress concentration. Specifically, the failed fiber will induce stress concentration in those un-failed neighbor fibers within the bundles. This stress concentration occurs during the nonlinear stage of tensile test [19, 31]. Therefore, it is valid to ignore stress concentration and exclusively consider the effects of reduced aspect ratio on modulus. In this study, the density of the 50 wt% injection molded samples was measured by the pycnometry method described in ref. [32].The density given by the supplier is 1.33 g/mm^3 and the measured value of the injection molded center-gated-disk (CGD) is 1.327 $\pm$ 0.0175 g/mm^3, which means the void content/porosity in the final parts is negligible. There is no information about the adhesion between the glass fibers and the matrix from the supplier. In this study, we assume the adhesion is perfect to simplify the problem, which most likely not be true. However, the 10 wt%, 30 wt%, 40 wt% and 50 wt% materials have the same surface treatments for the fibers (they are the same series using the same formulations). Therefore, it is legitimate to only include the effects of the clumping of fibers on the level-off of the elastic properties of the injection molded LFTs as fiber content increases.

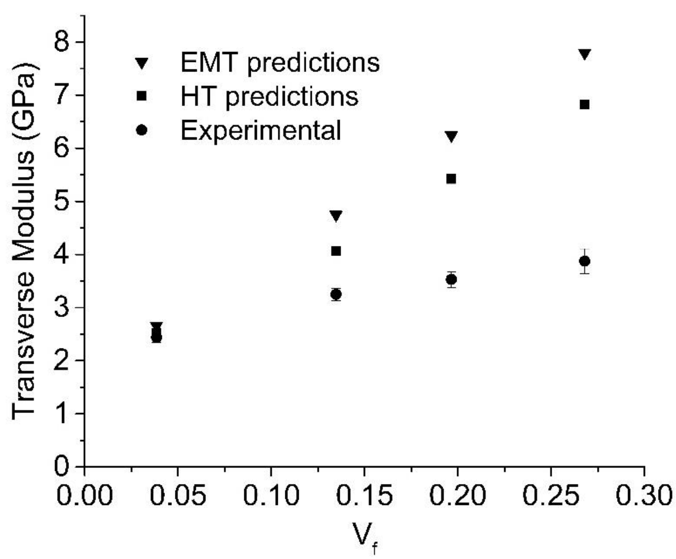

Figure 5-6: A comparison between the predictions using both HT and EMT methods, and the experimental tensile test results at various fiber content.

The cross-sectional microscopic images on the r-z plane with glass fiber foot-prints are shown in Figure 5-7. It is seen that the clumping of fibers turned out to be worse as fiber concentration increased. To include the effects of reduced aspect ratio on the modulus due to the existence of fiber bundles, an empirical model was proposed to replace the fiber diameter d in Eq. (5-6) with d_{i} defined as:

$$d_{\mathrm{i}} = d_0 * d_c(l_i, \mathrm{v}_f)$$

$$d_c = 1 + \frac{\left(\frac{\sqrt{a_r}}{\exp\left(\frac{\mathrm{v}_c}{\mathrm{v}_f}\right)}\right)^n}{1 + \exp(-\mathrm{v}_f a_r)} \tag{5-10}$$

$$a_r = \frac{l_i}{d_0}$$

Here, d_{i} is used to empirically include the mechanical degradation due to fiber clumping, d_0 the single fiber diameter, d_c a correction coefficient, a_r the fiber aspect ratio, l_i the measured single fiber length also used in Eq. (5-6), and v_f the fiber volume fraction. There are two empirical parameters, which need to be determined: v_c is a critical volume fraction and n is an exponent index. Both v_c and n can determine the slope and upper boundary of this empirical function. We believe the correcting coefficient d_c is a function of both fiber volume content and fiber length. At very low concentration (dilute concentration), the fibers have a much less chance to contact with each other and form bundles. The value of d_c should approach 1.0 at low fiber volume content. Besides, d_c should also keep increasing with v_f until reach an upper boundary. So, we modified form of the logistic function or logistic curve (‘S’ shape) and proposed our empirical model in the form of Eq. (5-10) [33].

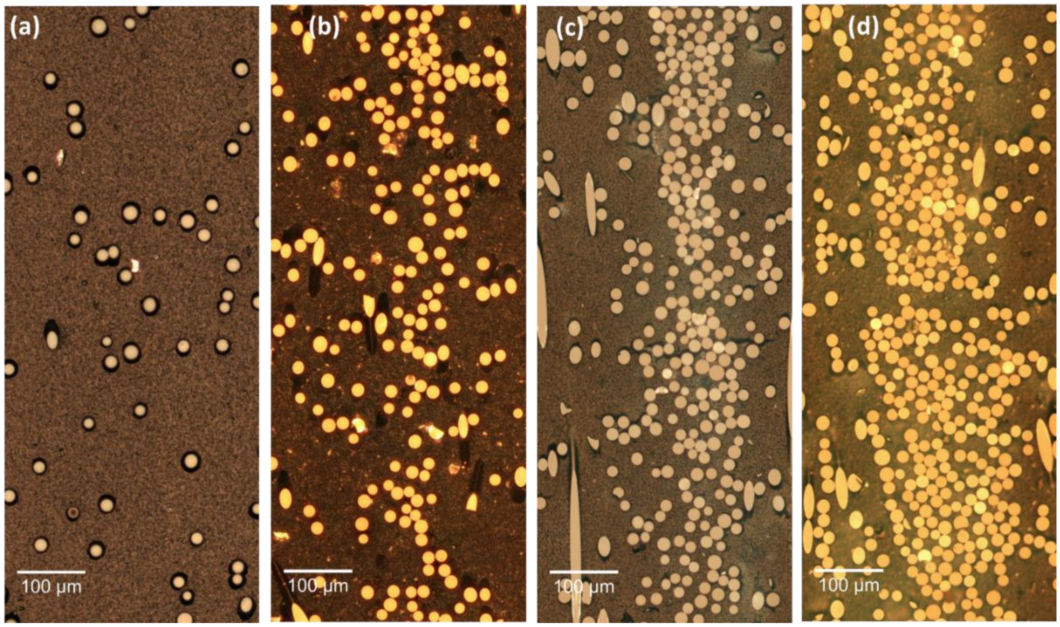

Figure 5-7: Cross-sectional microscopic images at the r-z plane for (a) 10 wt%, (b) 30 wt%, (c) 40 wt% and (d) 50 wt% glass fiber polypropylene composites.

This empirical model was used to correct the bundles size and fit both HT and EMT models to the tensile test results in the Hele-Shaw region with the non-linear least squares fitting method. The measured FLD and experimental fourth order orientation tensor were also used in the calculation. The empirical parameters of the d_c obtained by the fitting of both HT and EMT models are shown in Table 5-2. The comparisons of the fitted results with experiments at the Hele-Shaw region is shown in Figure 5-8. (a). After the application of the empirical model, the predictions turns out to be much more accurate when compared with tensile test results. However, this model might over-predict the bundles' size, because the perfect adhesion between glass fibers and matrix are assumed which might not be true. The empirical parameters obtained from the Hele-Shaw region was applied to calculate the modulus at the advancing-front. The comparisons among the as-calculated predictions, corrected predictions, and the experimental results are shown in Figure 5-8. (b). The predictions also show significant improvement after the diameter correction.

Table 5-2: Fitted parameters of the empirical model.

Model	$\mathbf{v}_c$	$\boldsymbol{n}$
EMT	0.15	1.47
HT	0.21	1.90

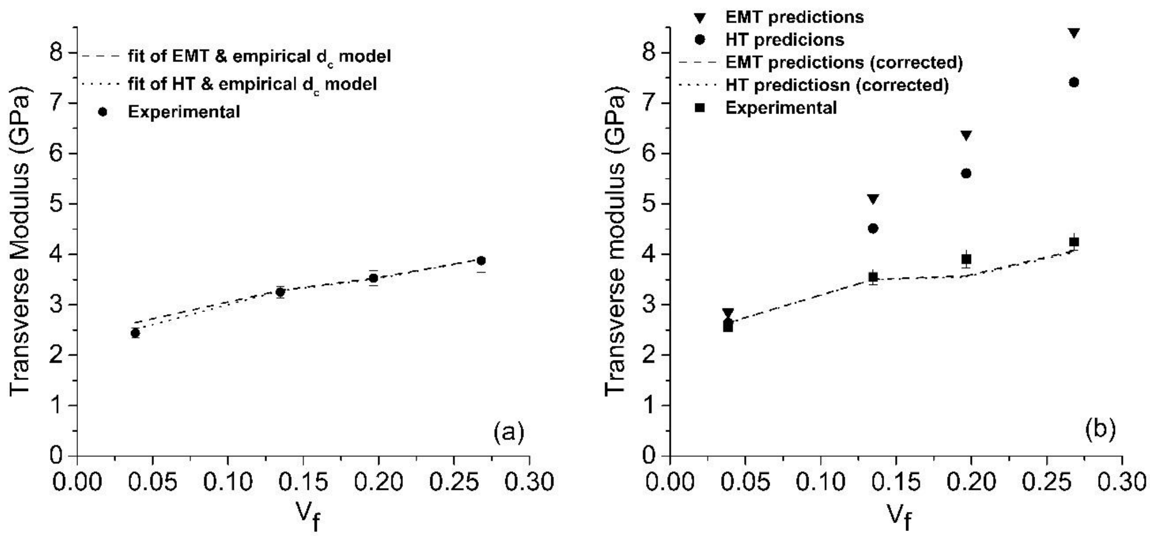

Figure 5-8: A comparison between the fit of EMT and HT with the experimental tensile test results with various fiber content, at the (a) Hele-shaw region. Comparisons among the as-calculated predictions, the corrected predictions using the fitted parameters from Hele-Shaw region and experimental data at (b) the advancing front region.

Figure 5-9 shows the fiber bundles' size as a function of fiber length at various fiber concentration using Eq. (5-10). The two empirical parameters were obtained by fitting the predictions from the EMT method to experimental tensile data. At low concentration(10 wt%), the magnitude of d_c barely increased in the length range from 0.06 mm to 12 mm. The slopes of the lines increase notably with concentration. At higher concentration (30, 40, 50 wt%) the values of d_c show a rapid increase with fiber length. The trends of d_c can be explained qualitatively from the fiber breakage aspect. At higher fiber content, the dominant fiber breakage mechanisms are fiber-fiber and fiber-machine interactions [34].

The residual fiber length exhibited a linear decrease following an increase in the fiber content [14, 35]. Several authors also suggested that the fiber breakage rate was proportional to the fiber length or fiber aspect ratio [12, 36]. The calculated bundle size, d_c, for those longer fibers is very large, especially for the 50 wt% fiber content. Qualitatively, under high fiber content, those long fibers have a great chance to contact the neighboring fibers and the machine (screw and wall of barrel). Fiber bundles reduce the effective fiber length or aspect ratio, significantly, allowing the preservation of longer fibers for higher content fiber composites during the intensive injection molding process.

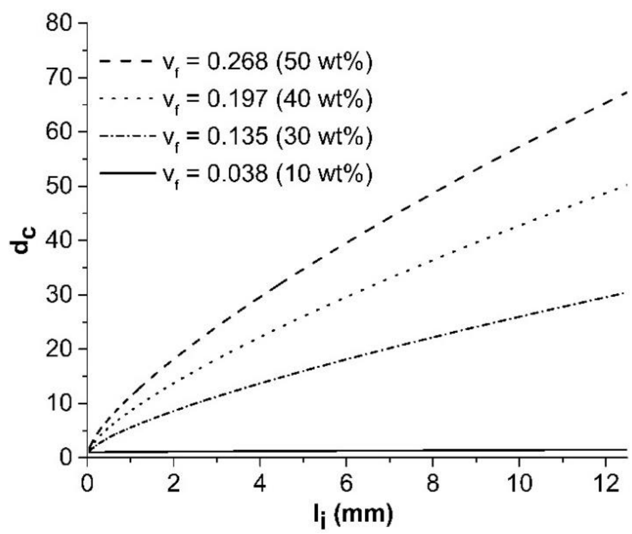

Figure 5-9: Predicted fiber bundles' size as a function of fiber length with various fiber concentrations by fitting the predictions using EMT method to experimental tensile data.

5.6 Conclusions

The stiffness properties have been studied in this work for 10 wt%, 30 wt%, 40 wt% and 50 wt% injection molded LFTs (glass/PP). Experimental measurements of fiber length distribution and fiber orientation were obtained to calculate the transverse modulus (θ direction) using both Halpin-Tsai (HT) model and the Mori-Tanaka model based on

Eshelby's equivalent inclusion (EMT). It has been shown that the EMT method generates slightly larger values than does the HT model. The accuracy of the various closure approximations for predicting the elastic properties has also been evaluated. The IBOF and ORW3 approximations turned out to be the best ways of describing the fourth order tensor in terms of the second order tensor. An important finding from this work is that the models over-predicted the modulus for higher fiber content injection molded LFTs. An empirical model was developed to correct the fibers' aspect ratio in the computations obtained for the actual as-formed LFTs with fiber bundles under high fiber content. After the correction, the analytical predictions matched well with the experimental stiffness values from tensile tests on the LFTs. The leveling off of the elastic properties of the injection molded LFTs as fiber content increases (> 30 wt%) is due to the existence of the fiber bundles. In this study, we assume the adhesion is perfect to simplify the problem, which most likely not be true. However, the 10 wt%, 30 wt%, 40 wt% and 50 wt% materials have the same surface treatments for the fibers. Therefore, it is legitimate to only include the effects of the clumping of fibers for comparison purpose. Moreover, the calculated bundle sizes from the proposed empirical model can be further applied to predict the strength in future work.

References

1. F. Henning, H. Ernst, R. Brüssel, LFTs for automotive applications, Reinforced Plastics, 49 (2005) 24-33.
2. K. Ortman, D. Baird, P. Wapperom, A. Whittington, Using startup of steady shear flow in a sliding plate rheometer to determine material parameters for the purpose of predicting long fiber orientation, J. Rheol., 56 (2012) 955-981.
3. R. von Turkovich, L. Erwin, Fiber fracture in reinforced thermoplastic processing, Polymer Engineering & Science, 23 (1983) 743-749.
4. S.G. Advani, C.L. Tucker, The use of tensors to describe and predict fiber orientation in short fiber composites, J. Rheol., 31 (1987) 751-784.

5. F. Garesci, S. Fliegener, Young's modulus prediction of long fiber reinforced thermoplastics, Composites Science and Technology, 85 (2013) 142-147.
6. C.L. Tucker III, E. Liang, Stiffness predictions for unidirectional short-fiber composites: Review and evaluation, Composites Science and Technology, 59 (1999) 655-671.
7. P.J. Hine, H. Rudolf Lusti, A.A. Gusev, Numerical simulation of the effects of volume fraction, aspect ratio and fibre length distribution on the elastic and thermoelastic properties of short fibre composites, Composites Science and Technology, 62 (2002) 1445-1453.
8. M. S. Ingber, T. D. Papathanasiou, A parallel-supercomputing investigation of the stiffness of aligned, short-fiber-reinforced composites using the Boundary Element Method, International Journal for Numerical Methods in Engineering, 40 (1997) 3477-3491.
9. Y. Takao, M. Taya, The Effect of Variable Fiber Aspect Ratio on the Stiffness and Thermal Expansion Coefficients of a Short Fiber Composite, Journal of Composite Materials, 21 (1987) 140-156.
10. J.C. Halpin, K. Jerine, J.M. Whitney, The Laminate Analogy for 2 and 3 Dimensional Composite Materials, Journal of Composite Materials, 5 (1971) 36-49.
11. P.J. Hine, H.R. Lusti, A.A. Gusev, On the possibility of reduced variable predictions for the thermoelastic properties of short fibre composites, Composites Science and Technology, 64 (2004) 1081-1088.
12. B.S. Hun, Glass fiber breakup in corotating twin screw extruder: Simulation and experiment, Polymer Composites, 33 (2012) 2147-2158.
13. J.L. Thomason, The influence of fibre length and concentration on the properties of glass fibre reinforced polypropylene. 6. The properties of injection moulded long fibre PP at high fibre content, Composites Part A: Applied Science and Manufacturing, 36 (2005) 995-1003.
14. Jim Thomason, Structure–property relationships in glass-reinforced polyamide, part 1: The effects of fiber content, Polymer Composites, 27 (2006) 552-562.
15. J. Halpin, Stiffness and expansion estimates for oriented short fiber composites, Journal of Composite Materials, 3 (1969) 732-734.
16. J. Affdl, J. Kardos, The Halpin-Tsai equations: a review, Polymer Engineering & Science, 16 (1976) 344-352.
17. R. Hill, A self-consistent mechanics of composite materials, Journal of the Mechanics and Physics of Solids, 13 (1965) 213-222.
18. D. Dray, P. Gilormini, G. Régnier, Comparison of several closure approximations for evaluating the thermoelastic properties of an injection molded short-fiber composite, Composites Science and Technology, 67 (2007) 1601-1610.
19. M. Taya, T. Mura, On Stiffness and Strength of an Aligned Short-Fiber Reinforced Composite Containing Fiber-End Cracks Under Uniaxial Applied Stress, Journal of Applied Mechanics, 48 (1981) 361-367.
20. C.W. Camacho, C.L. Tucker, S. Yalvaç, R.L. McGee, Stiffness and thermal expansion predictions for hybrid short fiber composites, Polymer Composites, 11 (1990) 229-239.
21. M.W. Hyer, Stress analysis of fiber-reinforced composite materials, DEStech Publications, Inc, 2009.
22. A. Standard, Standard test method for tensile properties of polymer matrix composite materials, ASTM D3039/D M, 3039 (2008) 2008.

23. V. Kunc, B.J. Frame, B.N. Nguyen, C.L. Tucker III, G. Velez-Garcia, Fiber length distribution measurement for long glass and carbon fiber reinforced injection molded thermoplastics, Research Gate, (2007).
24. G. Vélez-García, P. Wapperom, V. Kunc, D. Baird, A. ZINK-SHARP, Sample preparation and image acquisition using optical-reflective microscopy in the measurement of fiber orientation in thermoplastic composites, Journal of microscopy, 248 (2012) 23-33.
25. G.M. Vélez-García, P. Wapperom, D.G. Baird, A.O. Aning, V. Kunc, Unambiguous orientation in short fiber composites over small sampling area in a center-gated disk, Composites Part A: Applied Science and Manufacturing, 43 (2012) 104-113.
26. D.H. Chung, T.H. Kwon, Improved model of orthotropic closure approximation for flow induced fiber orientation, Polymer Composites, 22 (2001) 636-649.
27. D.H. Chung, T.H. Kwon, Invariant-based optimal fitting closure approximation for the numerical prediction of flow-induced fiber orientation, J. Rheol., 46 (2002) 169-194.
28. S. Houshyar, R. A. Shanks, A. Hodzic, The effect of fiber concentration on mechanical and thermal properties of fiber-reinforced polypropylene composites, Journal of Applied Polymer Science, 96 (2005) 2260-2272.
29. J.E. Little, X. Yuan, M.I. Jones, Characterisation of voids in fibre reinforced composite materials, NDT & E International, 46 (2012) 122-127.
30. D.J. Lee, H. Oh, Y.S. Song, J.R. Youn, Analysis of effective elastic modulus for multiphased hybrid composites, Composites Science and Technology, 72 (2012) 278-283.
31. Y. Swolfs, L. Gorbatikh, V. Romanov, S. Orlova, S.V. Lomov, I. Verpoest, Stress concentrations in an impregnated fibre bundle with random fibre packing, Composites Science and Technology, 74 (2013) 113-120.
32. N.A. Pratten, The precise measurement of the density of small samples, Journal of Materials Science, 16 (1981) 1737-1747.
33. R. Berger, Comparison of the Gompertz and Logistic Equations to Describe Plant Disease Progress, Phytopathology, 71 (1981) 716-719.
34. v.T. Richard, E. Lewis, Fiber fracture in reinforced thermoplastic processing, Polymer Engineering & Science, 23 (1983) 743-749.
35. M.J. Cieslinski, P. Wapperom, D.G. Baird, Influence of fiber concentration on the startup of shear flow behavior of long fiber suspensions, Journal of Non-Newtonian Fluid Mechanics, 222 (2015) 163-170.
36. J.H. Phelps, A.I. Abd El-Rahman, V. Kunc, C.L. Tucker, A model for fiber length attrition in injection-molded long-fiber composites, Composites Part A: Applied Science and Manufacturing, 51 (2013) 11-21.

Chapter 6 Conclusions and Recommendations for Future Work

6.1 Conclusions

1. A novel ‘needle’ down-sampling method was developed to collect the fibers at the location of interest through the thickness of the fiber stack. This method can generate a sampling cylinder with relatively uniform diameter, which will be used for the correction of sampling bias. An empirical equation was proposed to correct the sampling bias toward long fibers. After the correction, the measured results eventually became less dependent on the size of needle indicating an improvement on the accuracy of measurements. In this paper we also developed an automatic fiber length measurement technique based on Matlab®. The accuracy of this automatic tool was evaluated by comparing the as measured results with the manual measurement, and the final results showed good agreement between the two methods indicating the reliability of this automatic algorithm.

2. There is great disparity between the observed rates of fiber reorientation during shear and extensional flows. In this research, we developed a variable strain-reduction factor based on the local flow conditions, shear, extension, pure rotation, and the mixture of them, which are described by a flow-type parameter. The variable strain-reduction factor was then used in fiber orientation equations, to match the fiber reorientation rate to the local flow-type. Fiber orientation simulations for both non-lubricated squeeze flow and injection molded center-gated disk were conducted to verify this variable strain reduction factor method. The predicted orientation results showed improved qualitative agreement of the profile shape with the experimental data. This empirical variable strain reduction factor might help to improve the fiber orientation predictions especially in

complex flow, because it can reflect the different rates at which fibers orient during different flow conditions.

3. The ability of the existed analytical models to predict the stiffness of the injection-molded long fiber thermoplastic composites with changes in concentration, fiber length and fiber orientation were evaluated using 10 wt%, 30 wt%, 40 wt% and 50 wt% injection molded glass fiber reinforced polypropylene composites. Both the Halpin-Tsai (HT) model and the Mori-Tanaka model based on Eshelby's equivalent inclusion (EMT) were investigated to predict the transverse direction young's modulus in this study. The accuracy of the various closure approximations for the fourth order orientation tensor were also been evaluated in the predictions of elastic properties. The IBOF and ORW3 approximations turned out to be the best, as they generated the most comparable modulus with the experimental obtained fourth order orientation tensor. An important finding from this work is that the models over-predicted the modulus for higher fiber content injection molded LFTs. An empirical model was developed to correct the fibers' aspect ratio in the computations obtained for the actual as-formed composites with fiber bundles under high fiber content. After the correction, the analytical predictions matched well with the experimental stiffness values from tensile tests on the LFTs.

6.2 Recommendations for Future Work

4. During the tensile test before complete failure, the fiber composites experience two stages: the linear stage and the nonlinear stage as shown in Figure 6-1. At the nonlinear stage, the broken fiber within a fiber bundle could induce stress concentration [1-3] to the

closest survivor fibers as shown in the schematic diagram in Figure 6-1. A strength model should include the bundle effects on stress concentration in the non-linear stage of tensile test to better predict the strength of fiber composites. The predicted fiber bundle size using the empirical model of Eq. (5-10) would help to predict the stress concentration factors around broken fibers within the fiber bundles [4]. This might help to improve the strength predictions and further verify the proposed empirical bundle size model.

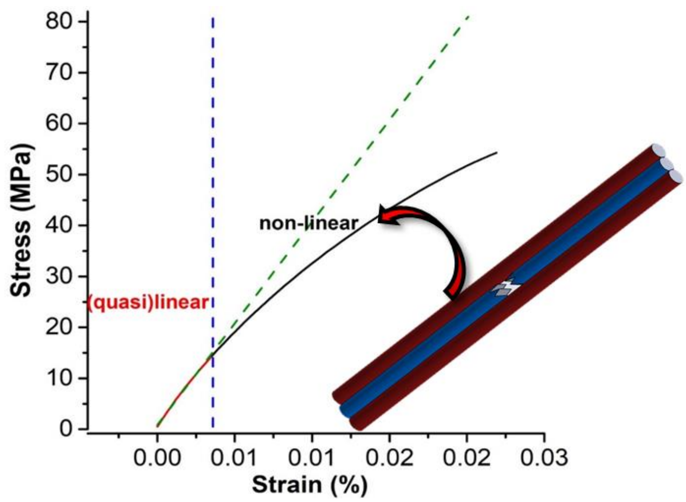

Figure 6-1: The stress-strain curve during tensile test with schematic diagram showing the broken fiber inducing stress concentration upon the neighbor fibers within a fiber bundle.

5. The proposed variable strain reduction factor in fiber orientation models has been tested in non-lubricated squeeze flow with only 1 Hencky strain. Additional Hencky strains need to be investigated to tracking the evolution of fiber orientation under multiple time steps, this will help to obtain a more conclusive understanding of this variable strain reduction factor method in fiber orientation predictions. It is also worth to compare the orientation predictions using this flow-type based strain reduction factor with experimental measurements in more complicated geometry like the End-gated plaque.

References

1. F. Raischel, F. Kun, H.J. Herrmann, Fiber bundle models for composite materials, Conference on Damage in Composite Materials, 2006.
2. S. Mahesh, S.L. Phoenix, I.J. Beyerlein, Strength distributions and size effects for 2D and 3D composites with Weibull fibers in an elastic matrix, International Journal of Fracture, 115 (2002) 41-85.
3. Y. Swolfs, L. Gorbatikh, V. Romanov, S. Orlova, S.V. Lomov, I. Verpoest, Stress concentrations in an impregnated fibre bundle with random fibre packing, Composites Science and Technology, 74 (2013) 113-120.
4. J. Watanabe, F. Tanaka, R. Higuchi, H. Matsutani, H. Okuda, T. Okabe, A study of stress concentrations around fiber breaks in unidirectional CF/epoxy composites using double-fiber fragmentation tests, Advanced Composite Materials, (2017) 1-13.